University of Kerbala

Collage of Science

Department of Physics

Development and Characterization of an Underwater Plasma System for Preparing SiO_2/Au Nanostructures

A Thesis Submitted to the Council of the College of Science, University of Kerbala in Partial Fulfillment of the Requirements for the Master Degree in Science of Physics

Written By:

Saja Hameed Abdulhamza

Supervised By:

Asst. Prof. Dr. Duaa Adel Uamran

July ٢٠٢5 A.D. **Safar ١٤٤7 A.H.**

بِسۡمِ ٱللَّهِ ٱلرَّحۡمَٰنِ ٱلرَّحِيمِ

(هُوَ الَّذي جَعَلَ الشَّمسَ ضِياءً وَالقَمَرَ نورًا وَقَدَّرَهُ مَنازِلَ لِتَعلَموا عَدَدَ السِّنينَ وَالحِسابَ ما خَلَقَ اللَّهُ ذلِكَ إِلّا بِالحَقِّ يُفَصِّلُ الآياتِ لِقَومٍ يَعلَمونَ)

صَدَقَ اللَّهُ الْعَلِيُّ الْعَظِيمُ

(سورة يونس الاية ٥)

Supervisor Certificate

We certify that the thesis entitled **"Development and Characterization of an Underwater Plasma System for Preparing SiO_2/Au Nanostructures"** was prepared under our supervision by (**Saja Hameed Abdulhamza**) at the Science College / Kerbala University as a partial fulfilment of the requirements for the M.Sc. Degree of Science in Physics.

Signature: Duaa A. Uam

Name: Dr. Duaa Adel Uamran

Title: Assistant Professor

Date: 27/08 2025

In view of the recommendations available, I forward this thesis for debate by the examining committee.

Signature: M. A. AL-KAAB

Name: Dr. Mohammed Abdulhussain AL-Kaabi

Title: Assistant Professor

Head of Physics Department, College of Science, University of Kerbala

Date: 29/9/ 2025

Examination Committee Certification

We certify that we have read this thesis, entitled **"Development and Characterization of an Underwater Plasma System for Preparing SiO_2/Au Nanostructures"** and as an examining committee, examined the student **"Saja Hameed Abdulhammza"** on its contents and that in our opinion it is adequate for the partial fulfillment of the requirements for the master degree of Science in Physics.

Signature
Name: **Dr. Fadhil Khaddam Fuliful**
Title: Professor
Address: University of Kerbala, College of Science, Department of Physics.
Date: / /
(Chairman)

Signature
Name**: Dr. Abdahussain A. Khadayeir**
Title: Professor
Address: University of Al-Qadisiyah, College of Education, Department of Physics.
Date: / /
(Member)

Signature
Name: **Dr. Nagham M. Shiltagh**
Title: Assist Professor
Address: University of Kerbala, College of Science, Department of Physics.
Date: 26/8/2025
(Member)

Signature:
Name: **Dr. Duaa A. Uamran**
Title: Assist Professor
Address: University of Kerbala, College of Science, Department of Physics.
Date: / /
(Member & Supervisor)

Signature:
Name: **Dr. Hassan Jameel Jawad AL-Fatlawy**
Title: Professor

Address: **Dean of the College of Science, University of Kerbala**
Date: / /

Dedication

I dedicate this thesis to my loving parents, whose unwavering support, sacrifices, and encouragement have been my guiding light throughout my academic journey. Your belief in me has been my greatest strength.

To my dear siblings, thank you for your constant motivation and for always being my pillars of support.

To my incredible friends your support, late-night conversations, and shared struggles made this journey lighter and more meaningful. I am forever grateful for your presence in my life.

Acknowledgments

First and foremost, all praise and gratitude are due to Allah, the Most Merciful and the Most Generous, for granting me the strength, patience, and wisdom to complete this research. Without His blessings, this work would not have been possible.

I am deeply grateful to my esteemed supervisor, Asst.Prof.Dr. Duaa Adel Uamran for her invaluable guidance, continuous support, and insightful feedback throughout this research journey. Their expertise, patience, and encouragement were instrumental in shaping this thesis.

I would also like to extend my sincere appreciation to the Department of Physics faculty and staff for their technical assistance, access to laboratory facilities, and academic support.

My gratitude also goes to the College of Science for providing an enriching academic environment and the resources necessary for this research.

ABSTRACT

The underwater electrical exploding wire (UEEW) technique has been developed and used to produce SiO_2/Au nanostructures, and the Au plasma in SiO_2 colloidal suspension. The plasma characteristics have been studied during the synthesis. The research has investigated the effect of current (100, 125, and 150 A) and SiO_2 mass (20, 25, and 30 mg) on plasma parameters (electron temperature T_e and density n_e). Furthermore, the nanostructures structural, morphological, and optical properties have been studied.

The study has used the optical emission spectroscopy (OES) to determine T_e and n_e through Boltzmann plots and Stark broadening. From which it has been noticed that the T_e (up to 10.32 eV) and n_e (up to 0.45×10^{18} cm^{-3}) have increased with the applied current. The X-ray diffraction (XRD) analysis has shown that the nanostructures contain a face center cubic (FCC) Au structure with crystalline sizes ranging from 12 to 34 nm.

The field emission scanning electron microscopy (FESEM) and transmission electron microscopy (TEM) images has displayed spherical morphologies between 21 and 39 nm. The UV-Visible spectroscopy results has demonstrated localized surface plasmon resonance (LSPR) peaks between 550 and 1007 nm and a direct bandgap between 2.792-2.878 eV. The thesis delivers essential knowledge about plasma-driven nanofabrication through the demonstration of how process parameters determine Nanostructures properties for plasmonic and renewable energy applications.

Table of Contents

List of Tables

List of Figures

List of Abbreviations

Abbreviation	Meaning
EDS	Energy-Dispersive X-ray Spectroscopy
EWT	Exploding Wire Technique
FCC	Face-Centered Cubic
FEG	Field Emission Gun
FESEM	Field Emission Scanning Electron Microscopy
FWHM	Full Width at Half Maximum
ICDD	International Centre for Diffraction Data
LSPR	Localized Surface Plasmon Resonance
NIST	National Institute of Standards and Technology
NPs	Nanoparticles
OES	Optical Emission Spectroscopy
SERS	Surface-Enhanced Raman Spectroscopy
TEM	Transmission Electron Microscopy
UEEW	Underwater Electrical Exploding Wire
UV-Vis	Ultraviolet-Visible (Spectroscopy)
XRD	X-Ray Diffraction

List of Symbols

Symbol	Meaning	Unit
A	Cross-sectional Area	m^2
A	Absorbance	(unitless)
A	Transition Probability	s^{-1}
A_{ij}	Transition Probability from level j to i	s^{-1}
c_o	Speed of Light in Vacuum	m/s
D	Crystalline Size	nm
d	Lattice Spacing	Å
e	Electron Charge	C
E	Energy	eV
Eg	Bandgap Energy	eV
E_j	Energy of Upper-Level j	eV
G	Statistical Weight	(unitless)
g_j	Statistical Weight of Level j	(unitless)
H	Planck's Constant	J·s
I	Current	A
I	Transmitted Intensity	(arbitrary units)
I_o	Incident Intensity	(arbitrary units)
I_{ij}	Spectral Line Intensity (j→i transition)	(arbitrary units)
K	Boltzmann Constant	J/K
K	Extinction Coefficient	(unitless)
L	Length	m

L	Geometrical Size of Plasma	m
m_e	Electron Mass	kg
N	Refractive Index	(unitless)
N	Order of Diffraction	(unitless)
n_e	Electron Density	cm^{-3}
N	Total Population Density	m^{-3}
N_D	Number of Electrons in a Debye Sphere	(unitless)
N_j	Population Density of Level j	m^{-3}
R	Resistance	Ω
R	Reflectance	%
T	Temperature	K
T	Transmittance	%
T_e	Electron Temperature	eV
Z(T)	Partition Function	(unitless)
A	Absorption Coefficient	m^{-1}
B	Full Width at Half Maximum (FWHM) of XRD peak	radians
Δ λ	Stark Broadening (FWHM)	nm
ε_0	Permittivity of Free Space	F/m
ε_1	Real Part of Dielectric Constant	(unitless)
ε_2	Imaginary Part of Dielectric Constant	(unitless)
λ	Wavelength	nm
λ_D	Debye Length	cm
ρ	Resistivity	mΩ
σ	Optical Conductivity	S/m
θ	Bragg Angle	degrees
ω_p	Plasma Frequency	rad/s

1.1 Introduction

Plasma diagnostic techniques provide the essential tools to serve as the key in our ability to comprehend and develop plasmas. Knowledge of the plasma parameters such as the electron's temperature T_e and density n_e and the evolvement of these parameters enable scientists to control generated plasmas in the most productive way possible to be adapted to satisfy a particular application [1]. The basic plasma diagnosis techniques include electrical, spectroscopic, and Magnetic Field Measurement [2].

One of the most prominent diagnosis techniques is the optical emission spectroscopy (OES) which is a technique that collects data from recorded radiation emitted by excited electrons and ions in the plasma [3]. However, the method in which the (OES) is carried require a high level of accuracy in the case of pulsed plasma which is difficult to achieve manually using the (UEEW) technique as multiple pulses happening simultaneously would result in inaccurate measurement.

This research will contribute to the existing knowledge on the plasma diagnosis by developing an automated version of the (UEEW) technique which is critical to the accuracy of the passive (OES) plasma diagnosis technique. This will help with advancing the accuracy and the simplicity of plasma diagnosis in which the suitable industrial and academic applications will be easier to identify. As well as the importance of gold nanostructures in various industrial applications [4].

1.2 Plasma Fundamentals

The word plasma originates from the Greek πλάσμα meaning moldable substance [5], and in physics, plasma can be defined as an ionized gas

containing charged and neutral particles exhibiting collective behavior with an approximate equal charge density. The ionization process begins at a well-defined temperature of about a few thousand Kelvins, plasma is considered as the fourth state of the matter [6].

One of the main plasma production methods is heating up a gas to increase the kinetic energy of the electrons high enough to cause collisions between the gas atoms to strip them of their outer shell electrons creating a mixture of ions and electrons. Another method is via energetic photons exposition such as Uv or X-ray sources [7].

This assembly of particles must have a “collective response" to perturbing agents in order to be defined as plasma. A collective response will occur when a perturbed charge carrier (e.g. Ion) has an effect on its nearest neighbors which will in turn affect their near neighbors, resulting in a response from a considerable number of coupled particles. However, the strong and long-range Coulombic forces between individual charge carriers must be screened from surrounding charged particles so that a localized charge does not play a significant role ensuring that collective influences. A range must be defined, and it is normally taken to be the distance beyond which the electrical field of a charged particle is shielded by particles having charge of the opposite sign and is known as the Debye length λ_D [8].

$$\lambda_D = \sqrt{\frac{\varepsilon_0 k_B T}{n_e e^2}} \qquad (1\text{-}1)$$

where ε_0 is the permittivity of free space, k_B is Boltzmann’s constant, T is the plasma temperature and e is the electron charge. The collective behavior required that $L >> \lambda_D$, where L represents the geometrical size of the plasma.

Furthermore, the number of electrons inside the “Debye sphere” must be greater than unity [9]:

$$N_D = \frac{4\pi n_e}{3}\lambda_D \gg 1 \quad (1\text{-}2)$$

The most important collective response of plasmas is the wavelike motions. The electron wave plays a fundamental role in many plasma interactions at the plasma frequency f_p [10]:

$$f_p = \sqrt{\frac{n_e e^2}{m_e \varepsilon_0}} \quad (1\text{-}3)$$

where m_e is the electron mass.

1.3 Plasma Classification

There are two main plasmas that are generally classified as high temperature (fully ionized and equilibrium) plasma and low temperature (non-equilibrium) plasma. The later has two types, thermal (and local thermal equilibrium) plasma and non-thermal (partially ionized between 0.01% and 1% and non-equilibrium) as shown in Figure 1.1 [11].

1.3.1 High Temperature Plasma

High temperature plasma, also known as equilibrium plasma, is a state where gas is heated to such extreme temperatures that nearly all atoms are ionized, resulting in a mixture of free electrons and ions. The thermal equilibrium means that the particles energy distribution follows Maxwell-Boltzmann statistics, and the plasma behaves collectively. Due to the abundance of charged particles, these plasmas conduct electricity and respond strongly to electromagnetic fields [12].

High-temperature plasmas are typically formed at temperatures exceeding tens of thousands to millions of kelvins. In fusion devices, temperatures above 100 million kelvins are required to sustain nuclear fusion reactions. Such conditions can be achieved using magnetic confinement, inertial

confinement (lasers), or electrical discharges. The high temperature plasmas are prone to instabilities (e.g., filamentation, turbulence) that can disrupt confinement and uniformity, posing challenges for fusion and material processing [13].

1.3.2 Low Temperature Plasma

1.3.2.1 Thermal Plasma

In thermal plasmas, the electron temperature and the heavy particle (ions and neutrals) temperature are nearly the same, allowing the use of equilibrium thermodynamics to describe the plasma's properties. This is in contrast to non-thermal plasmas, where electron temperature is much higher than that of heavy particles [14].

While thermal plasmas are often modeled as being in LTE, real systems frequently exhibit departures from equilibrium due to external forces, rapid processes, or gradients. These departures can be thermal (temperature differences between species) or chemical (non-equilibrium in reaction rates or species populations) [15].

Thermal plasmas are widely used in high-power industrial processes such as metal cutting, welding, spraying, and materials synthesis, where high energy densities and rapid reactions are required [16].

1.3.2.2 Non-Thermal Plasma

Non-thermal plasma, also known as non-equilibrium plasma, is a partially ionized gas (0.01% and 1%) where the temperatures of the plasma species (electrons, ions, and neutral particles) are not equal. In these plasmas, electrons are highly energetic (hot), while the bulk gas and heavier particles remain near ambient temperature, resulting in a non-equilibrium state [17].

Unlike thermal plasmas, where all species are at similar high temperatures, non-thermal plasmas have energetic electrons but low overall gas temperature. This allows for chemical activation without significant heating of the surrounding environment [18].

Non-thermal plasmas are typically generated by applying strong electric fields to gases at atmospheric or low pressure, using methods such as dielectric barrier discharge, glow discharge, corona discharge, or plasma jets [19].

Non-thermal plasmas are used in diverse fields, including chemical synthesis, environmental remediation (e.g., water and air purification), medicine (sterilization wound healing, cancer therapy), and agriculture (seed treatment, pathogen control) [20].

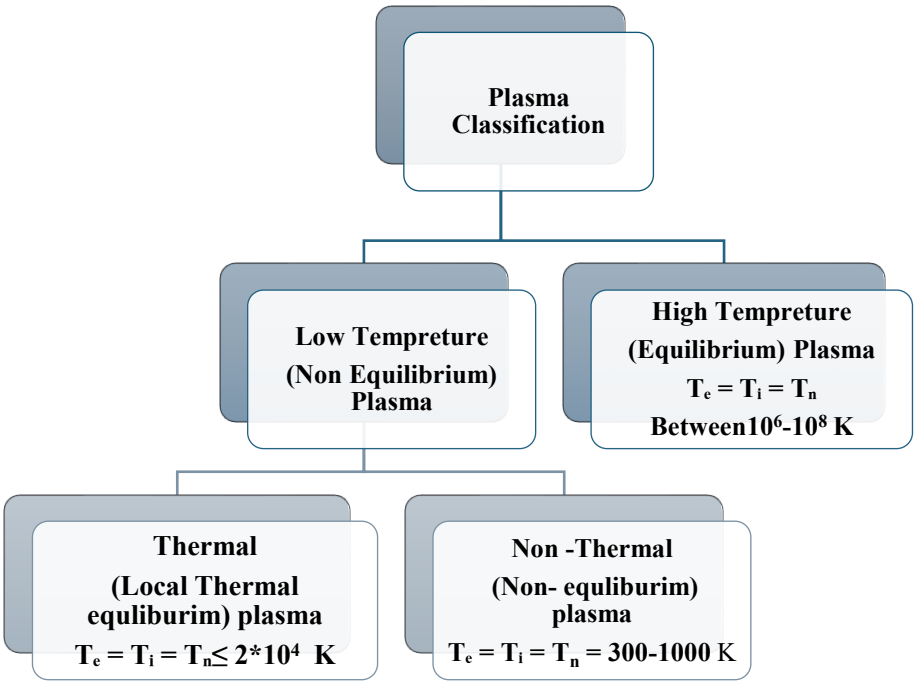

Figure 1.1: Plasma classification [11].

1.3.3 Continuous and Pulsed Plasma

Conventionally, plasma operates continuously as shown in Figure 1.2 which involves the maintenance of a constant state of ionization, this kind of plasma is mainly used in industrial applications such as welding and surface treatment [21].

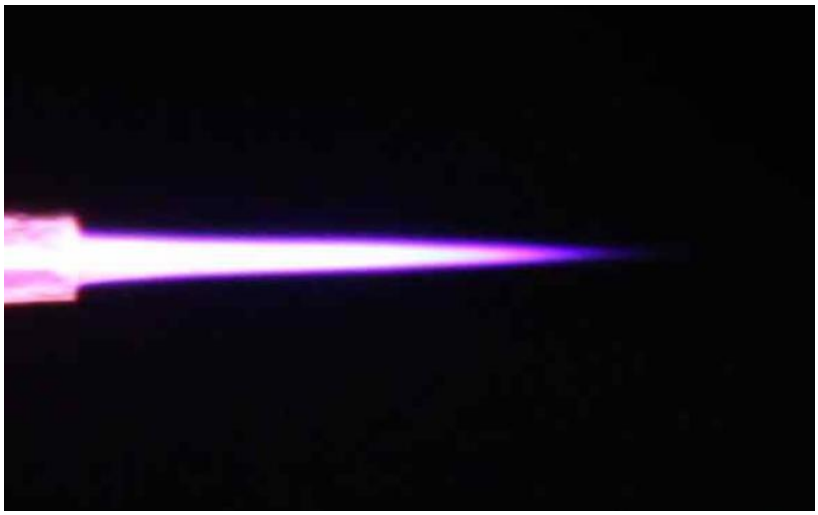

Figure 1.2: Plasma plume [22].

On the other hand, pulsed plasma can be described as a short burst of high energy which is able to create plasma of unique conditions such as high electron temperature and densities with a reduced energy consumption compared to continuous plasma [23], pulsed plasma is employed in material processing such as nanoparticle production [24].

1.4 Underwater Electrical Exploding Wire (UEEW) Technique

1.4.1 Principle and Advantages of UEEW

This technique consists of two electrodes, a metal thin wire and a plate both submerged in a liquid contained in a vessel. The electrical circuit

remains open until the thin wire contacts with the plate, which allows the current to run through the wire causing it to explode underwater [25]. The explosion causes the wire to undergo instant phase transition from solid to plasma which generates a shockwave in liquid, many factors affect the plasma properties such as the wire diameter, the material of the electrodes, the applied current and the underwater medium [26]. The UEEW is a simple, affordable and eco-friendly technique used in many applications such as electrohydraulic forming [27], inertial confinement fusion [28], plasma generation [29], and nanoparticle synthesis [30].

However, in the simplest form of the underwater UEEW technique the time required to mechanically close the electrical circuit via the thin wire contact with the metal plate can be widely varied between pulses which causes an incontrollable difference in the time of contact between the wire and the plate which can lead to poor repeatability and precision [31].

1.5 Plasma Diagnostics

The electron temperature (T_e) and electron density (n_e) is essential for understanding plasma behavior. Because these tools have been used to characterize the state of a plasma, influencing its degree of ionization, energy distribution, and overall behavior. In addition to that, Te effects the rates of excitation, ionization, and recombination, while ne determines the number of charge carriers, impacting conductivity, sheath formation, and wave propagation. Finally, the variations in Te and ne influence plasma uniformity, stability, and the formation of structures like sheaths and transport barriers, which are critical for both laboratory and industrial plasmas [32].

Plasma exists in a state of quasi-neutrality because the electron and ion population numbers remain approximately equal. The extent of ionization differs between plasma types because thermal plasmas maintain higher electron densities than cold plasmas

The electron temperature directly influences plasma kinetics: Higher T_e corresponds to greater electron kinetic energy, enhancing ionization. Plasma returns to a neutral gas state through electron-ion recombination when T_e decreases [33].

Plasma Diagnostic Techniques exist in two distinct approaches which are described in the following [34]:

1. Internal Diagnostics (Direct Contact Methods) Plasma potential and density measurements become possible through current-voltage characteristic analysis using electrical probes.
2. External Diagnostics (Non-Invasive Methods) Plasma morphology and dynamics become visible through optical imaging techniques. Spectroscopic techniques capture the emission spectra to determine T_e and n_e .The phase shifts in transmitted waves allow microwave interferometry to determine electron density.

These methods enable precise plasma characterization, essential for applications in fusion research, material processing, and nanotechnology.

1.5.1 Optical Emission Spectroscopy

Optical emission spectroscopy is a remote analytical technique of the light emitted from a certain medium without any external optical excitation [35].

One of the most prominent diagnosis techniques is the optical emission spectroscopy (OES) which is a passive technique that collects data from recorded radiation emitted by excited electrons and ions in the plasma [36].

OES works by exciting atoms or ions in a sample (often using plasma, laser ablation, or electrical discharge), causing them to emit light at characteristic wavelengths as they return to lower energy states. The emitted light is collected by a spectrometer, allowing identification and quantification of

elements based on their unique emission spectra. In plasma-based OES, such as Inductively Coupled Plasma OES , a high-temperature plasma excites the sample, and the resulting emission lines are measured to determine elemental concentrations [37].

OES main advantages include that OES does not alter or consume the sample during measurement, Enables rapid analysis, useful for process control and diagnostics in manufacturing and plasma applications [38]. However, OES has some disadvantages such as: The Emission lines from different elements can overlap which complicates the analysis, especially in complex matrices, line broadening can limit resolution and accuracy, especially for isotopic or fine-structure analysis, and it needs plasma, laser, or electrical discharge, which may not be suitable for all sample types [39].

The (OES) is carried in a way that require a high level of accuracy in the case of pulsed plasma which is difficult to achieve manually using the (UEEW) technique as multiple pulses happening simultaneously would result in inaccurate measurement, the automation of the (UEEW) technique helped enhancing the accuracy across all the samples.

1.5.2 Measurement of Electron Temperature (T_e): Boltzmann Plot

There are many methods to determine the electron temperature from the emission spectrum of a plasma such as the two-line emission ratio method. and the Boltzmann plot method. The line-to-Continuum method determine the electron temperature via comparing the spectral lines of the plasma using the National Institute of Standards and Technology (NIST) database to the continues emission spectrum which is often used in the laser induced breakdown spectroscopy [40], the two-line emission ratio method depends on the temperature to calculate the ratio of intensity for two spectral lines of the same element to estimate the plasma temperature [41], while the

Boltzmann plot method Considers multiple spectral lines which enhances the accuracy compared to the previous method where the natural logarithm of the spectral lines intensities is plotted against the energy of higher level of transition where the slop of the plotted line is the inverse of the electron temperature [42].

The electron density n_i is assumed to be 10^{14} m^{-3}, and the energy is 1 eV. The electron temperature (T_e) can be determined using the density ratio method, which compares the intensities of two emission lines. The ratio of the intensities (I_1 and I_2) is given by [43]:

$$\frac{I_1}{I_2} = \frac{A_1 g_1 \lambda_2}{A_2 g_2 \lambda_1} exp\left(-\frac{E_1 - E_2}{kT_e}\right) \quad (1\text{-}4)$$

where:

- I_1,I_2 = intensities of the two spectral lines.
- A_1,A_2 = transition probabilities.
- λ_1,λ_2 = wavelengths of the emission lines.
- g_1,g_2 = statistical weights of the upper energy levels.
- E_1,E_2 = upper-level energies of the two transitions.
- k = Boltzmann constant (1.38×10^{-23} J/K).

Rearranging Eq. (1-4) allows the electron temperature to be expressed as:

$$kT_e = \frac{E_1 - E_2}{Ln\left(\frac{I_2}{I_1}\right) - Ln\left(\frac{A_2 g_2 \lambda_1}{A_1 g_1 \lambda_2}\right)} \quad (1\text{-}5)$$

The relationship between the two energy levels, Ei (lower) and Ej (upper), with atomic densities Ni and Nj can be described using the Boltzmann distribution under thermal equilibrium conditions [43]:

$$\frac{N_j}{N_i} = \frac{g_j}{g_i} exp\left[-\frac{E_j - E_i}{kT}\right] \quad (1\text{-}6)$$

Here, g_i and g_j are the statistical weights of the respective states, *k* is the Boltzmann constant (1.38×10^{-23} J/K), and *T* is the temperature in Kelvin. If the total population density is *N*, the distribution of atoms across energy states follows:

$$\frac{N_j}{N} = \frac{g_j}{Z(T)} exp\left[-\frac{E_j - E_i}{kT}\right] \quad (1\text{-}7)$$

where *Z*(*T*) is the partition function, representing the sum of Boltzmann-weight contributions from all energy levels [43]:

$$Z(T) = \sum_m g_m \, exp\left[-\frac{E_m}{kT}\right] \quad (1\text{-}8)$$

When an atom transitions from the upper level *Ej* to the lower level *Ei*, the emitted spectral line intensity *Iji* is given by [43]:

$$I_{ji} = \frac{hc_0}{4\pi\lambda_{ji}} A_{ji} \quad (1.9)$$

Here, λ_{ji} is the emission wavelength, *h* is Planck's constant, c_0 is the speed of light in vacuum, and A_{ji} is the transition probability (the likelihood per second of spontaneous emission from state *j* to *i*). Combining equations (1-9) and (1-7) and rearranging yields:

$$\frac{I_{ji}\,\lambda_{ji}}{A_{ji}\;g_j} = \frac{hc_0 N}{4\pi Z(T)} exp\left[-\frac{E_j}{kT}\right] \quad (1\text{-}10)$$

Taking the natural logarithm of both sides gives:

$$Ln\left(\frac{I_{ji}\,\lambda_{ji}}{A_{ji}\;g_j}\right) = -\frac{E_j}{kT} + C \quad (1\text{-}11)$$

where *C* is a constant. By plotting $Ln\left(\frac{I_{ji}\,\lambda_{ji}}{A_{ji}\;g_j}\right)$ against *Ej* for multiple spectral lines (all sharing the same lower energy level), the electron temperature *Te* can be determined from the slope of the resulting linear relationship [44].

1.5.3 Measurement of Electron Density (n_e)

The Stark broadening of spectral lines is a powerful diagnostic tool for estimating electron density in plasmas. This method is based on the broadening of atomic emission lines due to the electric field effect (Stark effect) caused by the surrounding charged particles (electrons and ions) For high-density plasmas (n_e>10^{17}cm^{-3}) [45]:

$$\Delta w_{H\alpha} = 1.3 \left(\frac{n_e(cm^{-3})}{10^{37}}\right)^{0.64\pm0.03} \quad (1\text{-}12)$$

Where: w is the electron impact parameter (width per unit electron density, tabulated for Hα line) and n_e is the electron density

solving the equation (1.12) for n_e:

$$n_e = \left(\frac{\Delta w_{H\alpha}}{1.3}\right)^{1/0.64} \times 10^{17} cm^{-3} \quad (1\text{-}13)$$

1.6 Nanoparticles

1.6.1 Nanoparticles Definition and Production Methods

An atom or a molecule of an element that is nanometer sized can be defined as a nanoparticle that range in size (1-100) nm. NPs vary in shape as they include nanoshells, nanotubes, quantum dots, etc., and differ in morphologies such as crystalline or amorphous [46, 47].

Nanoparticles main advantage is the distinct properties difference from their micro or macro particles counterpart without losing their chemical identity [48].

The wide range of NPs applications has attracted the attention of researchers in various fields such as medicine, materials science, food science, electronics, and agriculture [49].

There are many different methods to produce NPs, Physical, Chemical, and Biological (green) methods However all these methods can be classified as either the top-down method or the bottom-up method, The top down method disassembles the bulk material into a nanoscale particles, while the bottom-up methods assembles atoms to clusters to a nanoscale particles [50].

Chemical NPs methods include the sol-gel method [51] Chemical Reduction Method [52, 53], etc. while biosynthesis methods involve microorganisms, fungi, and plant extract [54]. The chemical and biological methods mentioned are bottom-up methods. As for Physical methods, they are top-down methods as they include mechanical milling method [55], nanolithography method [56], laser ablation method [57], and the plasma methods [58] especially arc discharge methods such as underwater electrical explosive wire UEEW [59].

1.7 Nanoparticle Characterization

1.7.1 The Structural and Morphological Properties

1.7.1.1 X-Ray Diffraction

X-ray diffraction (XRD) functions as a core analytical method which determines material atomic structures in crystalline materials. The interaction of monochromatic X-rays with crystalline samples results in constructive interference that produces specific diffraction patterns when Bragg's condition is met [60].

$$n\lambda=2d\sin\theta \quad (1\text{-}14)$$

The technique provides three critical structural parameters including crystalline size calculated via Scherrer's equation:

$$D = k\lambda / (\beta \cos\theta) \quad (1\text{-}15)$$

Lattice strain derived from Williamson-Hall analysis, and Phase identification through peak position matching with the International Centre for Diffraction Data ICDD databases.

XRD serves as a powerful tool for analyzing plasma-synthesized nanoparticles because it helps detect: Metastable phases that emerge because of rapid plasma quenching processes. The face-centered cubic (FCC) structure dominance in Au shells can be quantified through this method. The amorphous silica signature appears at $2\theta \approx 22°$ [60].

1.7.1.2 Field Emission Scanning Electron Microscopy

FESEM is an imaging technique invented in 1936 by Erwin Muller [61], that is an effective tool to study surface morphology and composition [62]. This technique utilizes accelerated electrons rather than a light source like standard microscopes, where the electrons pass through a vacuum column where a lens causes the electrons to deflect and bombard the sample until it emits secondary electrons which are caught by a detector and transformed to an electrical signal from which a scan image is generated [63].

The FESEM follows mainly the same imaging process as the scanning electron microscopy SEM. However, the primary difference between the two techniques is the electron generation system, where the FESEM use the field emission gun FEG while the SEM depends on the thermionic emission to generate electrons [64]. This difference has led to the FESEM advantages over SEM three of which are the FESEM magnification power surpassing the SEM by 100,000 ×, clear images with a reduced electrostatic distortion, and the spatial resolution is brought down to 1.5 nm [65].

1.7.1.3 Transmission Electron Microscopy

Transmission electron microscopy (TEM) allows scientists to directly observe nanoparticle core-shell structures at atomic resolution. The

technique operates on the principle of electron transmission through ultra-thin samples (<100 nm), with contrast mechanisms which include mass-thickness contrast for elemental differentiation, Diffraction contrast for crystalline analysis, and High-resolution phase contrast for lattice imaging [66].

Our analysis employs TEM in those operational modes Bright-field imaging for morphology assessment .Selected area electron diffraction for crystallinity verification.

1.7.2 UV-Vis Spectroscopy

UV-Vis spectroscopy functions as a basic analytical instrument for determining nanomaterial optical properties through its application to plasmonic nanoparticles such as SiO_2@Au core-shell structures. The technique analyzes light absorption and scatter from 190-1100 nm wavelengths to generate quantitative information about electronic transitions and surface plasmon resonances [67].

Beer-Lambert equation

$$I = I_0 \mathrm{e}^{-\alpha t} \qquad (1\text{-}16)$$

Where Io and I are the incident and the transmitted photon intensity respectively and α is the absorption coefficient and t is the thickness of the material, The absorption coefficient (α) is calculated from absorption spectrum using:

$$\alpha = 2.303 \frac{A}{t} \qquad (1\text{-}17)$$

The electron transitions are between the Valance band, and the conductive band are divided into direct and indirect transition , it is obeying the following equation:

$$\alpha h\upsilon = B\left(h\upsilon - E_g\right)^r \qquad (1\text{-}18)$$

where B is a constant inversely proportional to amorphousness , r represents the transition type of electrons where if its value is equal to (1/2) then the transition is an allowed direct one where the electrons transition to the conduction band without a momentum change enabling an efficient photon emission, if r value is (3/2) then the transition is direct forbidden which means its less probable as it requires minor phonon assistance due to symmetry, if r equals (2) then it is an allowed indirect transition where electrons rely on phonon interactions to conserve momentum, finally if r is (3) then it's forbidden indirect transition where the electrons further suppress photon emission due to additional symmetry constrains [68].

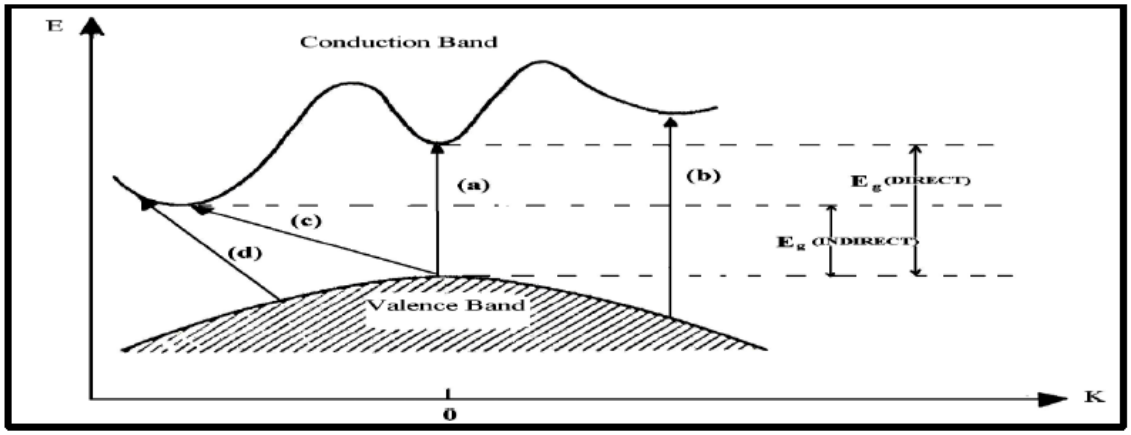

Figure 1.3 : The optical transitions (a) Allowed direct, (b) Forbidden direct, (c) Allowed indirect, (d) Forbidden indirect [68].

The equations required to calculate the optical properties are the following [69]:

Transmission (T): $T = 1 \,/\, e^{(2\cdot 303A)}$ (1-19)

Reflectance (R): $R = 1 - (A + T)$ (1-20)

Extinction coefficient (k): $k = \frac{\alpha\lambda}{4\pi}$ (1-21)

Refractive index (n) : $n = \left[\frac{4R}{(R-1)^2} - k^2\right]^{-\frac{1}{2}} - \frac{(R+1)}{(R-1)}$ (1-22)

Optical Conductivity(σ): $\sigma = \frac{\alpha nc}{4\pi}$ (1-23)

Real (ε_r) and imaginary parts (ε_i) of dialectical constant:

$$\varepsilon_r = n^2 - k^2 \quad (1\text{-}24)$$

$$\varepsilon_i = 2nK \quad (1\text{-}25)$$

And λ is the wavelength.

1.8 Literature review

1. **Anshuman Sahai et al. (2016)** made the first exploding wire technique (EWT) device using plate-wire configuration to generate copper nanoparticles with multifunctional properties. The researchers performed a thorough characterization using seven analytical methods including XRD and HRTEM and XPS and they found that Cu/Cu_2O nanoparticles became ferromagnetic at room temperature because of their oxygen-deficient lattice structures. The study proved that the exploding wire technique produced complex phase compositions beyond traditional detection capabilities which extended opportunities for copper-based nanomaterials in spintronic technologies. This study proved an effective analytical process for multi-phase metal oxide nanoparticle analysis and demonstrated how EWW makes special nanomaterials with unique characteristics [70].

2. **Hoffman et al. (2017)** performed primary studies of how laser-induced plasma behaves when placed in liquid media. The experimental data showed that plasma temperatures achieved 25,000 K at 20 ns but then cooled down to 8,500 K during the next 500 ns. The study used measurements to show that electron density started at 2×10^{25} m^{-3} before decreasing to 2.5×10^{23} m^{-3} throughout 1,000 ns.

Additionally, the researchers observed how water vapor dissociation created a 5,500 K vapor layer that surrounded the plasma plume. The hydrodynamic model showed precise predictions for temperature ranges (18,000-23,000 K) and pressures (2 GPa) which matched experimental results. The research provided essential knowledge about plasma expansion and cooling processes which continue to be vital for laser ablation and material processing applications [71].\

3. **Kanti Sapkota et al. (2018)** invented a method for synthesizing SiO_2/Au-Ag nanocomposites using Nephrolepis cordifolia tuber extract as an environmentally friendly method. The synthesized SiO_2 nanoparticles displayed spherical shape at 200-246 nm and were decorated with Au/Ag NPs approximately 3 nm in size. The dual functionality of these nanocomposites consisted of efficient catalytic properties and antimicrobial capabilities. The nanocomposites demonstrated outstanding catalytic properties in solvent-free amidation reactions which resulted in high yields without additives and displayed potent antibacterial properties against Gram-positive and Gram-negative bacteria. The plant-based synthesis method produced nanomaterials in a sustainable way while remaining biocompatible and keeping human keratinocyte compatibility. The researchers developed a sustainable nanomaterial synthesis process which produces multi-functional products for organic synthesis and biomedical applications [72].
4. **Vladislav Gamaleev et al. (2018)** made a major advancement by establishing stable micro-arc discharges in seawater at extreme pressures reaching 19 MPa. A rod-to-rod electrode system enabled the researchers to preserve plasma ignition across all pressure conditions at voltages below 850 mV. The research established that preheating

energy requirements showed a direct relationship with pressure levels because they increased from 5 mJ at 1 atm to 36 mJ at 19 MPa. The research found that high-pressure conditions led to particular spectral signatures which displayed powerful continuum backgrounds alongside broadened spectral peaks
indicating fundamental shifts in plasma properties compared to normal atmospheric conditions [73].

5. **S. Bhattacharya et al. (2019)** used spectroscopic analysis along with fast photography to improve underwater plasma understanding. The researchers discovered that anode material selection produces significant effects on plasma temperature since SS304 reaches 5,500 K and zircaloy reaches 14,372 K. The high-density plasma environment showed unique characteristics, including observable Hα line emission but suppressed Hβ transitions. Their high-speed imaging revealed new arc phenomena including JxB pumping, and simultaneous multiple arc attachments which refute traditional single-attachment theories and reveal new mass transport mechanisms processes [74].

6. **Y. Bacqueyrisses et al. (2021)** directed their research underwater subsonic discharges using capacitor-based pulsed-power generators, experimental data from currents of 5–100 kA and energies of 250 J–25 kJ revealed that peak pressure generation follows the phenomenological model Crucially, the initial stored energy was found to be less significant than peak current and discharge speed. The research concludes that optimal pressure output requires maximizing both current and voltage while minimizing discharge time, achieved by reducing capacitance and increasing breakdown voltage. This

model, valid for currents from 1 kA to hundreds of kA, provides key design principles for high-pressure underwater plasma sources. [75].

7. **K. Suliz et al. (2022)** introduced a groundbreaking joint electrical explosion method that uses different metal wires to create AlCrFeCuNi alloy nanoparticles during a single-step operation. The produced nanoparticles showed a lognormal distribution pattern with 40 nm average diameter and their nanocrystalline structure consisted of BCC and FCC phases. The researchers showed that the technique enabled precise control of alloy composition and phase characteristics at the nanoscale which resolved critical manufacturing issues for complex alloy nanoparticles. The developed process demonstrated outstanding potential to generate multicomponent nanomaterials with specific functional characteristics by performing element mixing operations at nanoscale levels for multiple metallic components [76].

8. **Dong Yan et al. (2023)** examined underwater high-voltage pulsed discharges to determine energy conversion mechanisms through two separate plasma channel stages which included heating-dominant plasma generation and arc channel development leading to breakdown. The researchers documented key parameters through their experiments which included a 10 Ω equivalent resistance and 0.1 μm initial channel radius and determined that the minimum breakdown voltage required 6 kV for electrode gaps of 0.5 cm. The developed equivalent theory framework provided practical tools for industrial operators to monitor discharge equipment and optimize energy conversion efficiency in pulsed power systems [77].
9. **Xiandong Li et al. (2024)** studied the underwater arc discharge and discovered that three distinct stages develop within millisecond

timeframes. The researchers found three different stages that included short-period oscillation and long-period oscillation and quasi-steady state phases where bubble vapor reached supercritical conditions at minimum radius (827 K, 140 MPa). The research showed that light radiation absorption along with electrode heat conduction functions as controllers for bubble motion while delivering quantitative knowledge of energy transfer mechanisms. Their research showed that standard AC/DC power sources can produce repetitive shock waves using single long-spark discharges at an economical cost compared to advanced pulsed power systems [78].

10. **M. Simeni et al. (2025)** created important breakthroughs in nanosecond underwater pulsed discharges through their analysis of power measurement data and absolute spectroscopic techniques. Free-free bremsstrahlung radiation produced by electron-neutral collisions generated the dominant continuum radiation during the primary spark of a 10 ns discharge with 3.5 MW peak power and 35 mJ energy. Inverse bremsstrahlung proved to be a significant factor that affected discharge processes. The researchers found that the initial discharge produced bubbles which emitted H_2 continuum radiation. Absolute spectroscopy combined with analytical continuum source calculations established a valuable method to study transient plasma phenomena in liquid media [79].

1.9 Aim of the Study

Significant literature gaps exist regarding the direct synthesis of SiO_2@Au nanostructures via the underwater electrical exploding wire (UEEW) method, particularly concerning the effects of the underwater medium on plasma dynamics and resulting nanoparticle characteristics. This Study aims to develop an eco-friendly, and automated version of the UEEW technique to generate plasma and produce Au/SiO_2 nanostructures, while diagnosing the plasma parameters and studying the nanostructure's structural, optical & morphological proper

2.1 Introduction

This chapter outlines the experimental approach for developing using an automated underwater electrical exploding wire (UEEW) system. In addition to generating underwater arc discharge plasma and finally, synthesizing and characterizing SiO_2/Au core-shell nanostructures Key steps include:

Material Preparation: gold wire and plate and the SiO_2 colloidal suspension were prepared under controlled conditions.

The UEEW system: the Arduino-controlled system ensured precise, repeatable electrical discharges in water.

Plasma Diagnostics : Optical emission spectroscopy (OES) measured electron temperature (T_e) and density (n_e).

Nanostructure Analysis : XRD, FE-SEM, TEM, and UV-Vis spectrometer were used to examine structure, morphology, and optical properties.

2.2 Materials

2.2.1 SiO_2 nanoparticles

SiO_2 nanoparticles produced in china by Zhongnuo Advanced Material Technology Company. have been selected to be the core material of the desired Nanostructures due to their chemical stability, optical transparency, biocompatibility, and strong adhesion to the gold shell [80, 81]. The SiO_2 nanoparticles propertises are demonstated in Table 2.1 To investigate the applied current and the SiO_2 consitration effects on the plasma parameters and the optical and structural properties of the produced SiO_2/Au nanostructure.

Table 2.1: SiO_2 properties [82].

Chemical formula	**SiO_2**
Molar mass	60.0843 g/mole
Appearance	White Powder
Density	2.634 g/cm^3

2.2.2 The Gold Plate and Thin Wire

From an alloy of 24 Karats gold, boasting a purity of 99.99%, a plate with the dimensions of 3 cm by 1.5 cm by 1 mm and a wire with a fixed diameter of 0.3 mm shown is in Figure 2.2. The Au properties are displayed in Table 2.2, the wire and plate resistance can be calculated from the following equation [83]:

$$R = p(L/A) \quad (2\text{-}1)$$

Where R is the resistance in ohms (Ω), ρ is the material's resistivity (from Table 2.2), L is the length of the conductor , and A is the cross-sectional area.

The wire resistancehas been calculated to 0.04142 Ω while the plate resistance is equal to 0.00008133 Ω both at 20 C tempreture.

The wire and plate have been precisly fabricated to be the electrodes in the UEEW system. These specific measurements of the gold plate and wire were chosen to accommodate the scale of the experiment setup and ensure practical integration into the reaction vessel.

Figure 2.1: The Au plate and thin wire.

Table 2.2: Au physical Properties [82].

Physical Properties	
Density (at room temperature)	19.30 g/cm3
Melting Point	1337.33 K
Boiling Point	3243 K
Risistivity	2.44 *10^{-8} ohm in 20 ºC
Atomic Properties	
Oxidation State	5, 3, 2, 1, −1, −2, −3 (an amphoteric oxide)
Atomic Radius	Empirical: 144 pm
Covalent Radius	136±6 pm
Van der Waals radius	166 pm
Miscellanea	
Crystal structure	face-centered cubic
Magnetic ordering	Diamagnetic

2.3 The Automated Underwater Exploding Wire Technique

The automated underwater exploding wire (UEEW) system includes an Arduino Uno board which operates a servo motor to precisely position a thin wire electrode 3 cm apart from the submerged gold plate in a liquid medium. The servo motor establishes contact between the wire and plate while applying a high-current spark which causes the wire to vaporize into a short-lived plasma formation in the surrounding liquid.

The Arduino-based automation system has been developed to provide precise timing and wire plate contact force control during each explosion spark which leads to better reproducibility of plasma conditions and nanoparticle synthesis than manual operation. The basic setup consisting of Arduino and servo motor with electrodes and a reaction vessel made out of plastic with 45 ml capacity.

The reaction vessel contains the Au electrodes and 30 ml of distilled water mixed with SiO_2 nanoparticles. The electrical circuit opens until the thin gold wire and plate come into mechanical contact which is controlled by the Arduino Uno board. The high current intensity passing through the thin wire instantly causes a nonlinear explosion of the thin wire, which creates a pulse. This process is programmed to reoccur for 15 times each.

Each sample's first spark was recorded at room temperature via an optical fiber attached to a calibrated StellarNet spectrometer.

The UEEW is automated using a micro servo motor controlled via an Arduino Uno board which is connectted to the micro servo motor via connective wires and a bread board as shown in Figure 2.2, it runs on a C++ code [84]. where the intervals between pulses are 0.1 second to control the contact between the wire and the plate.

The mechanisim [26] [25] [79]:

1. Energy Deposition and Joule Heating

A high-voltage, high-current electrical pulse (often from a large capacitor bank) is discharged through a thin metal wire submerged in water. An enormous amount of power is dumped into the wire in a very short time (microseconds to milliseconds). The electrical current meets resistance in the wire, causing intense Joule heating. The heating is so rapid that the wire's material cannot dissipate the heat through conduction or radiation. Its temperature skyrockets, far surpassing its melting point and then its boiling point.

2. Vaporization and Phase Change

The solid wire almost instantaneously transforms into a cloud of superheated metal vapor. This happens *before* the wire has a chance to physically expand

or change shape significantly (a process known as superheating). Water is an excellent medium for this phenomenon because it is nearly incompressible and an efficient conductor of pressure waves. It acts like a very strong "container," preventing the metal vapor from expanding freely.

3. Plasma Formation and Rapid Expansion

As the temperature continues to rise (reaching tens of thousands of Kelvin), the metal vapor becomes ionized, stripping electrons from their atoms and forming a plasma—a conductive state of matter. Massive Pressure Build-Up: This plasma is an extremely hot, high-pressure gas. It tries to expand with immense force, but the incompressible water surrounding it violently resists this expansion. The pressure inside the plasma bubble builds to a critical point where it overcomes the confinement of the water. This is the moment of explosion. The plasma bubble expands supersonically, pushing against the water.

4. Shockwave Generation and Bubble Oscillation

The supersonic expansion of the plasma launches a powerful pressure shockwave through the water. This is the primary destructive force of the explosion, similar to the blast wave from high explosives. After the initial expansion, the hot gas plasma bubble continues to grow until its internal pressure drops below the surrounding water pressure. The inertia of the water

then causes the bubble to collapse. This collapse can be so violent that it generates a secondary shockwave and may even cause the bubble to rebound and oscillate (expand and collapse multiple times). The rapid collapse can also produce sonoluminescence—brief flashes of light caused by the focusing of energy.

The code for the Arduino board is as follows:

```
#include <Servo.h>
int servoPin = 11;
Servo servo1;
void setup() {
  servo1.attach(servoPin);
  Serial.begin(9600);
}
void loop() {
  for(int iteration = 0; iteration < 15;
iteration++) {
    for(int currentAngle = 90; currentAngle <= 165;
currentAngle += 5) {
      servo1.write(currentAngle);
      Serial.print("Iteration: ");
      Serial.print(iteration);
      Serial.print(", Angle: ");
      Serial.println(currentAngle);
      delay(100);
    }
  }
  while(1); // Stop after 15 times
}
```

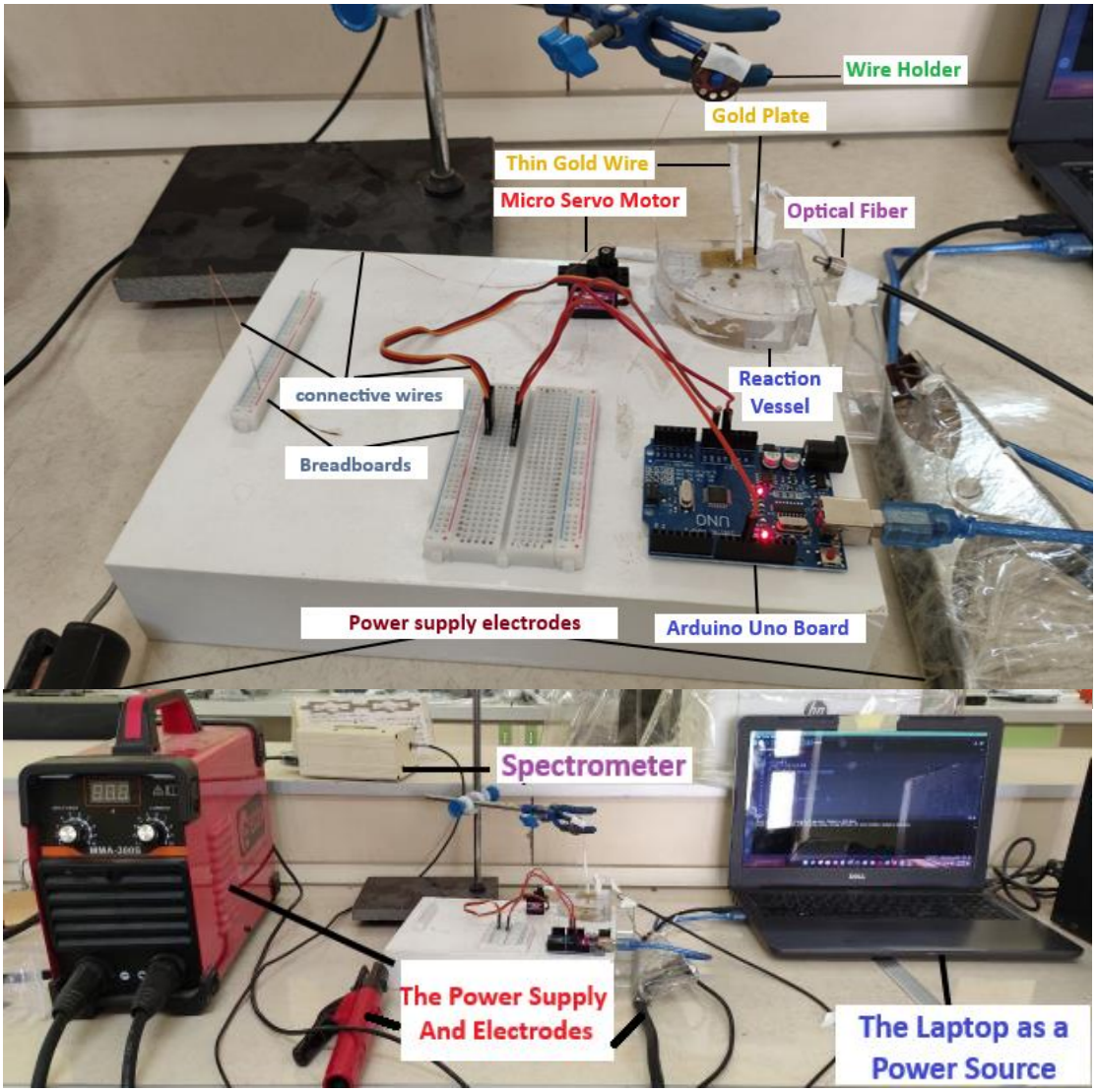

Figure 2.2: The automated UEEW setup.

2.4 Sample Preparation

Three quantities of SiO_2 nanoparticles powder, 20, 25, and 30 mg, were measured by an analytical scale. Each amount of SiO_2 nanoparticles has been dissolved with 30 ml of distilled water by magnetically stirring the mixture at 70 °C and 500 RPM for 25 min to ensure an adequate mixture as shown in Figure 2.3. From this, the 20 and 30 mg samples were subjected to a fixed

current intensity of ١٢٥ A, while the 25 mg samples were subjected to three different applied currents of 100, 125, and 150 A.

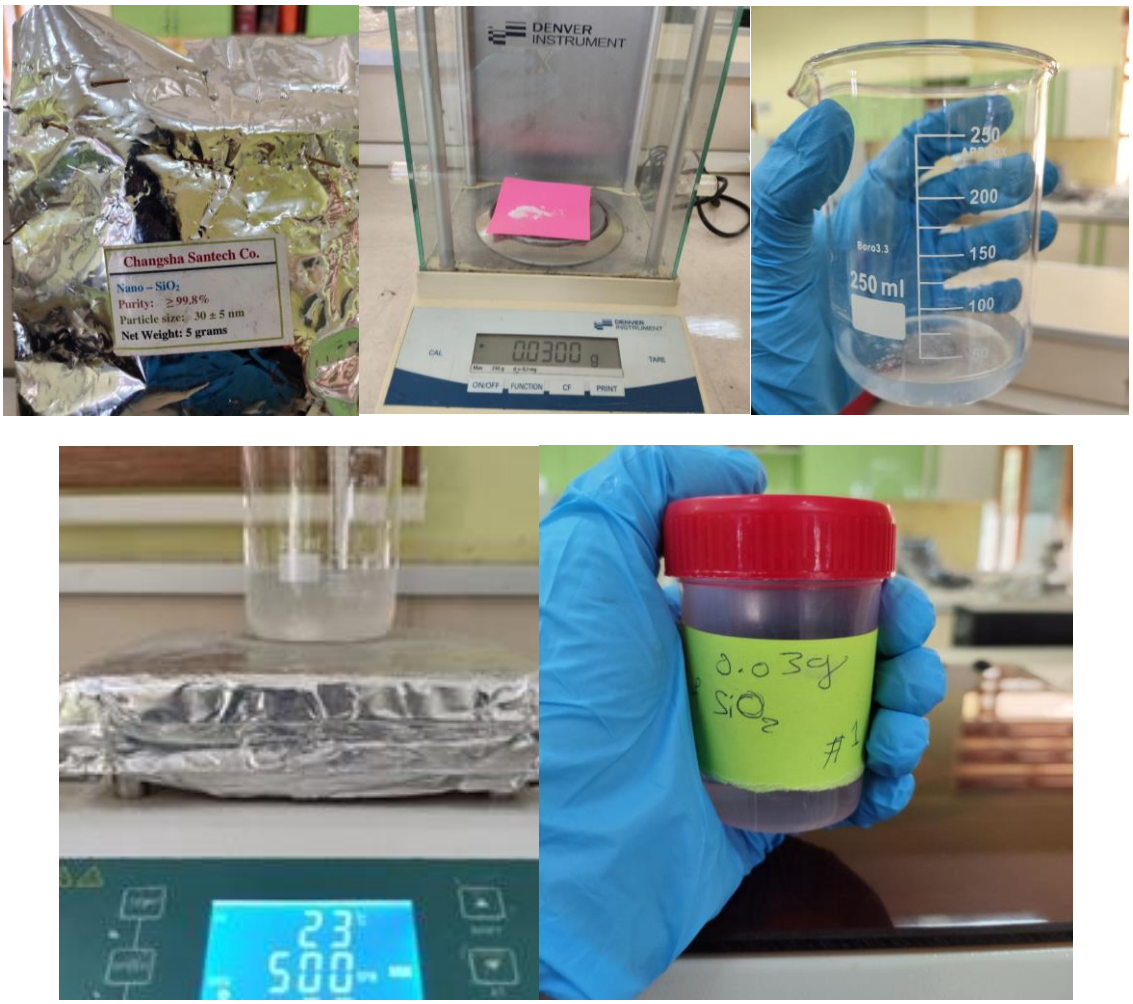

Figure 2.3: The SiO_2 colloidal suspension preparation.

2.5 Thin Films Preparation

Drop casting method has been used to prepare a thin films as shown in Figure 2.4 for each sample for the purpose of preparing the samples to be tested via XRD, TEM, an FESEM. ,The microscope glass slides (25 × 75 mm, 1 mm thickness) has been cleaned via an Ultrasonic cleaner (40 kHz frequency) with ethanol then deionized water.

After the SiO_2/Au colloidal colloidal suspension (post-UEEW) preapration, A 5 mm pipette has been used to drop a determined volume of the colloidal suspension onto the center of the cleaned slide.

Each drop was left to dry at room teampreture to allow complete solvent evaporation. The process was repeated 30 times, with each drop overlapping the previous one. The thickness of theses films has been noticed through the FE-SEM cross section imeges to be nonuniform and its mean value (3131 nm for the 25 mg and 100 A Sample, 1808 nm for the 25 mg and 125 A Sample, 2326 nm for the 25 mg and 150 A Sample, 1581 nm for the 20 mg and 125 A Sample, and 4264 nm for the 30 mg and 125A Sample)as shown in the Figures 2.5, 2.6, 2.7, 2.8, and 2.9.

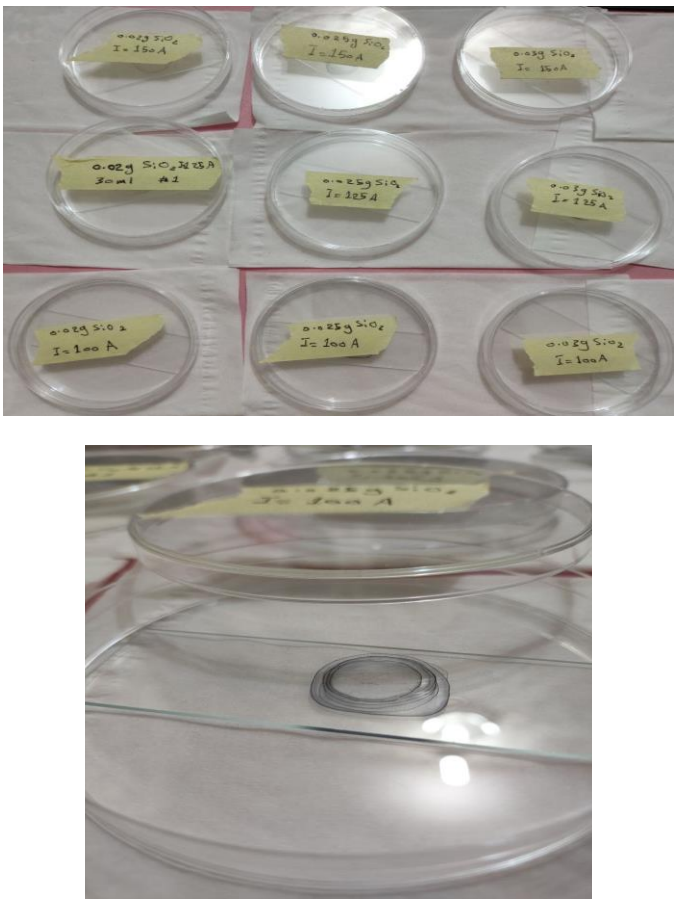

Figure 2.4: SiO_2/Au thin film preparation.

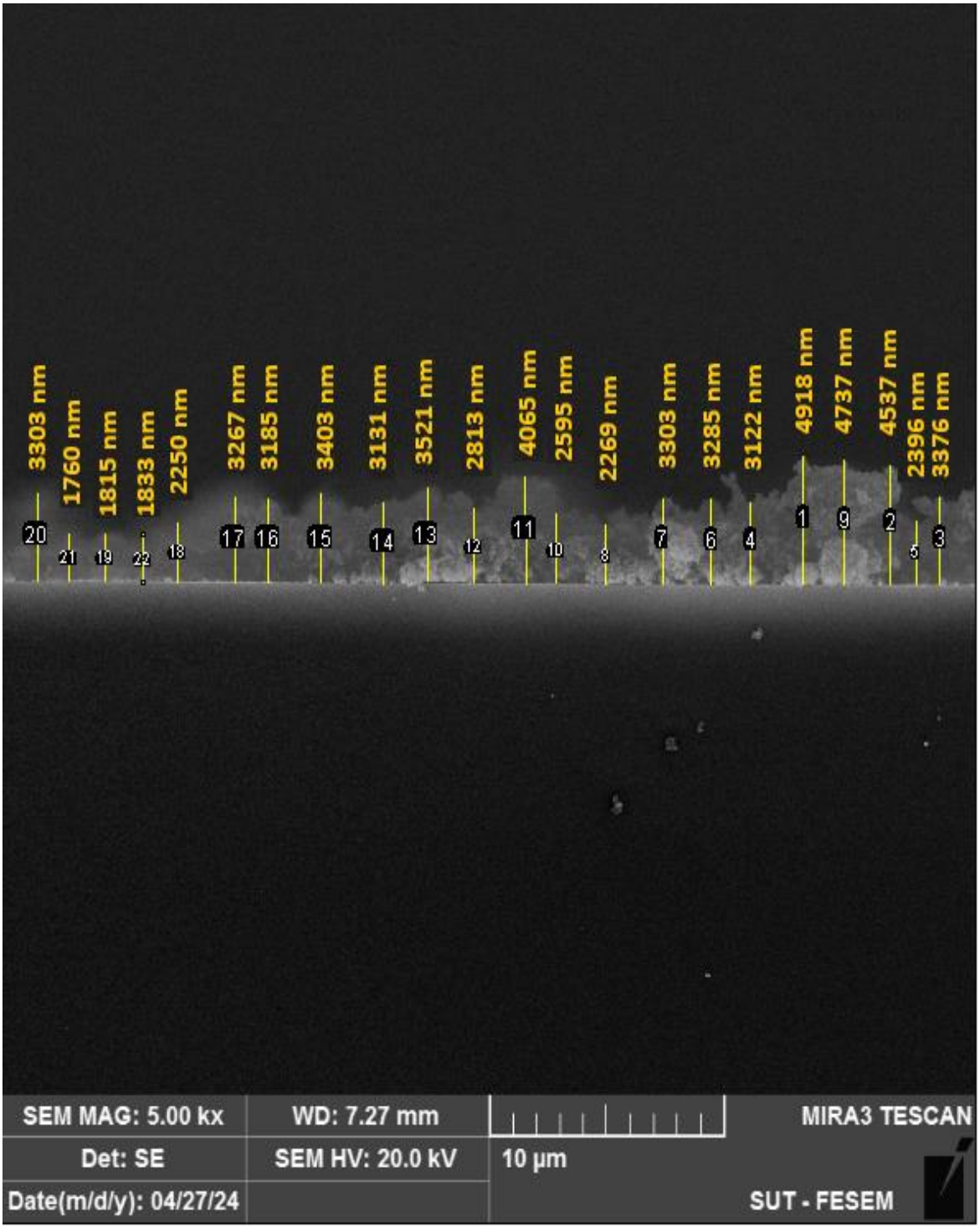

Figure 2.5: FE-SEM cross section image for the SiO_2/Au thin film where the SiO_2 added mass is 25 mg and an applied current of 100 A.

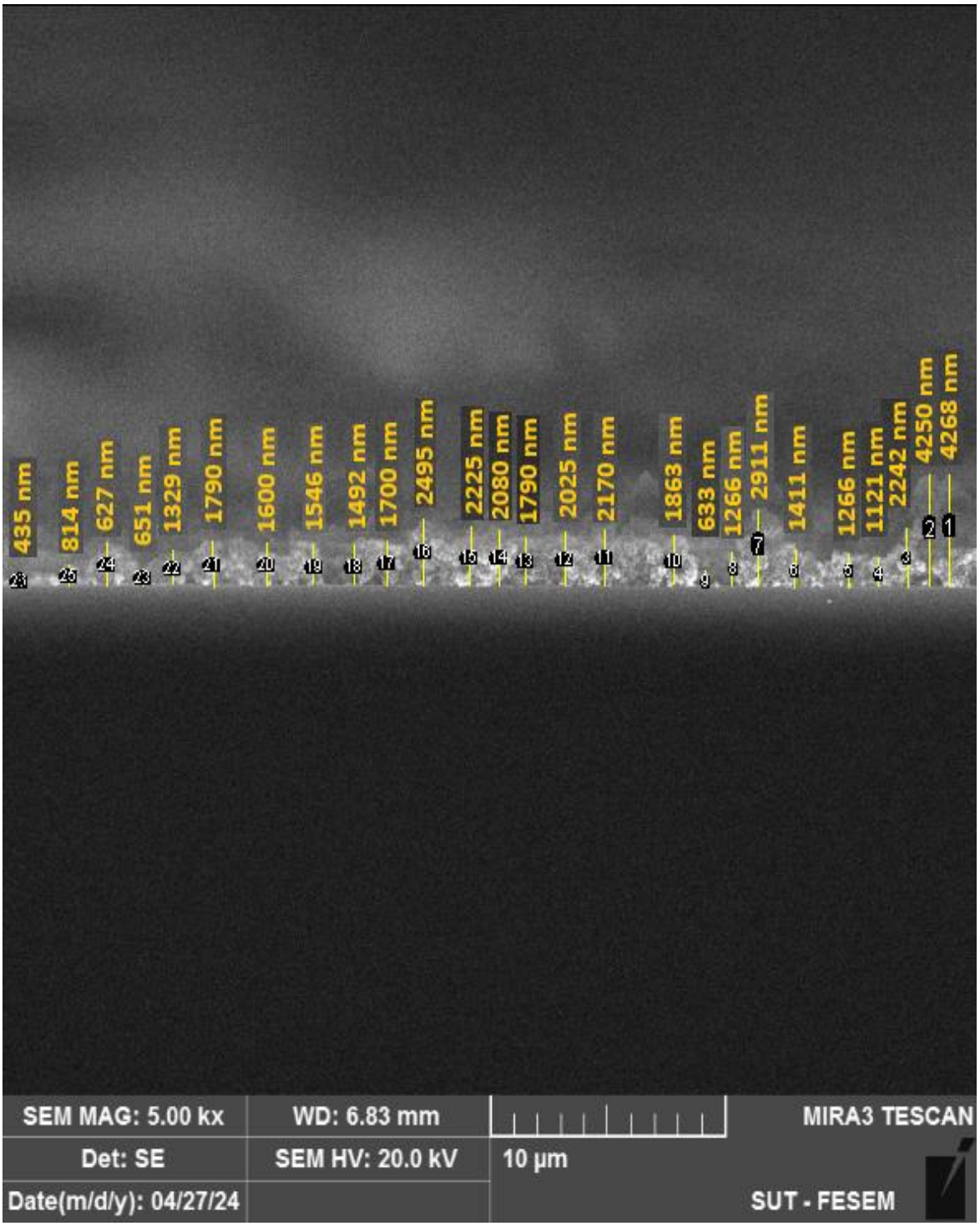

Figure 2.6: FE-SEM cross section image for the SiO_2/Au thin film where the SiO_2 added mass is 25 mg and an applied Current of 125 A.

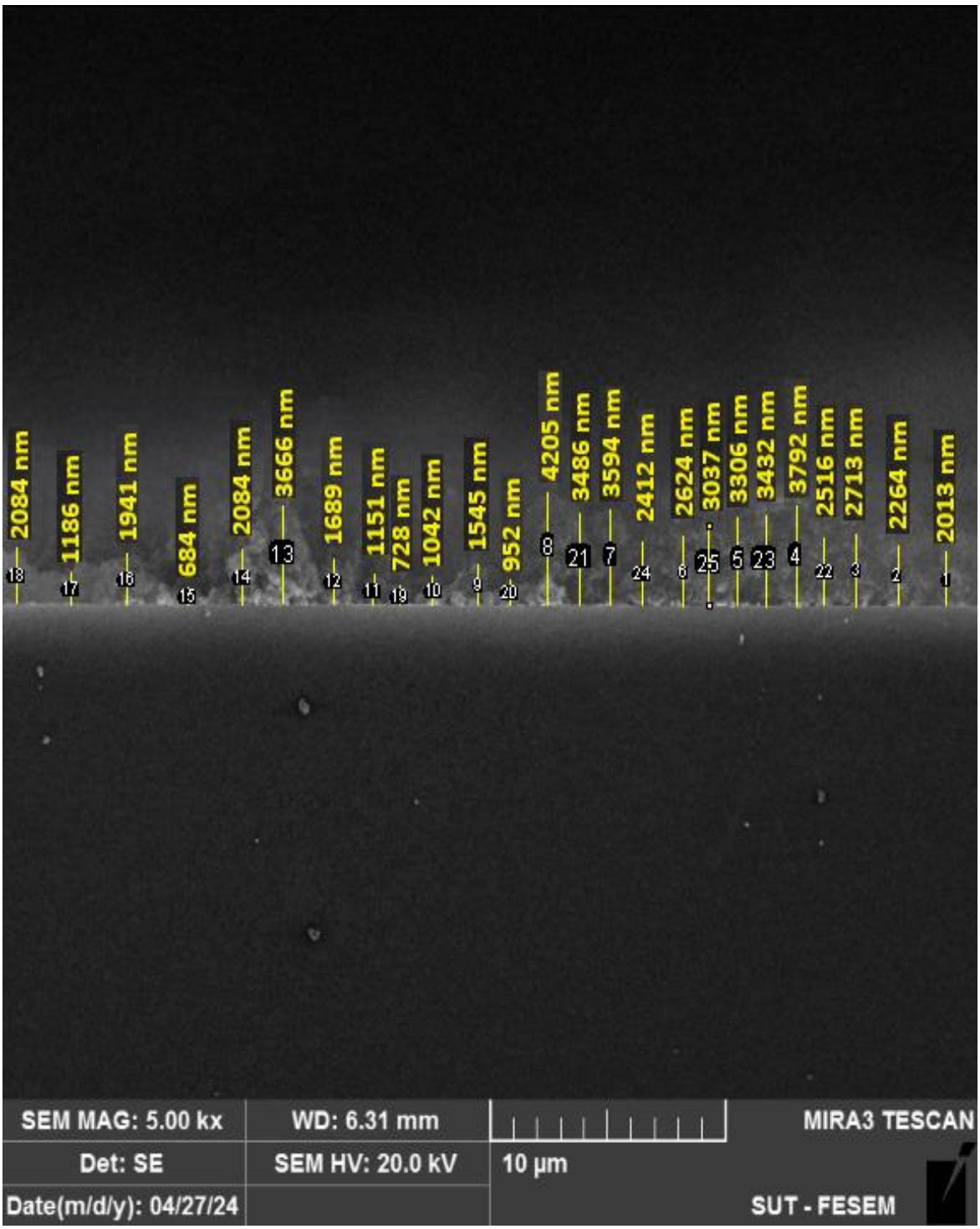

Figure 2.7: FE-SEM cross section image for the SiO_2/Au thin film where the SiO_2 added mass is 25 mg and an applied Current of 150 A.

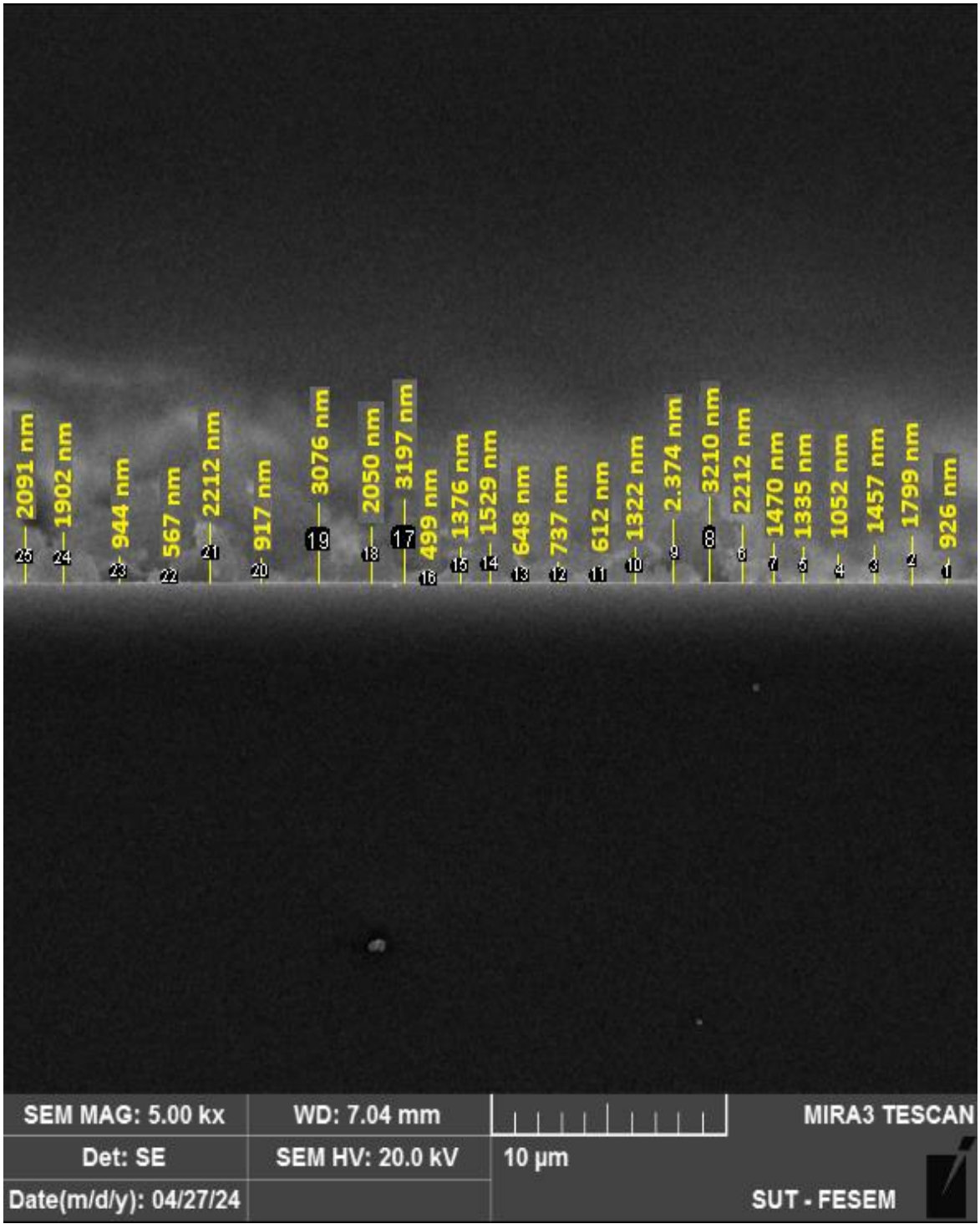

Figure 2.8: FE-SEM cross section image for the SiO_2/Au thin film where the SiO_2 added mass is 20 mg and an applied Current of 125 A.

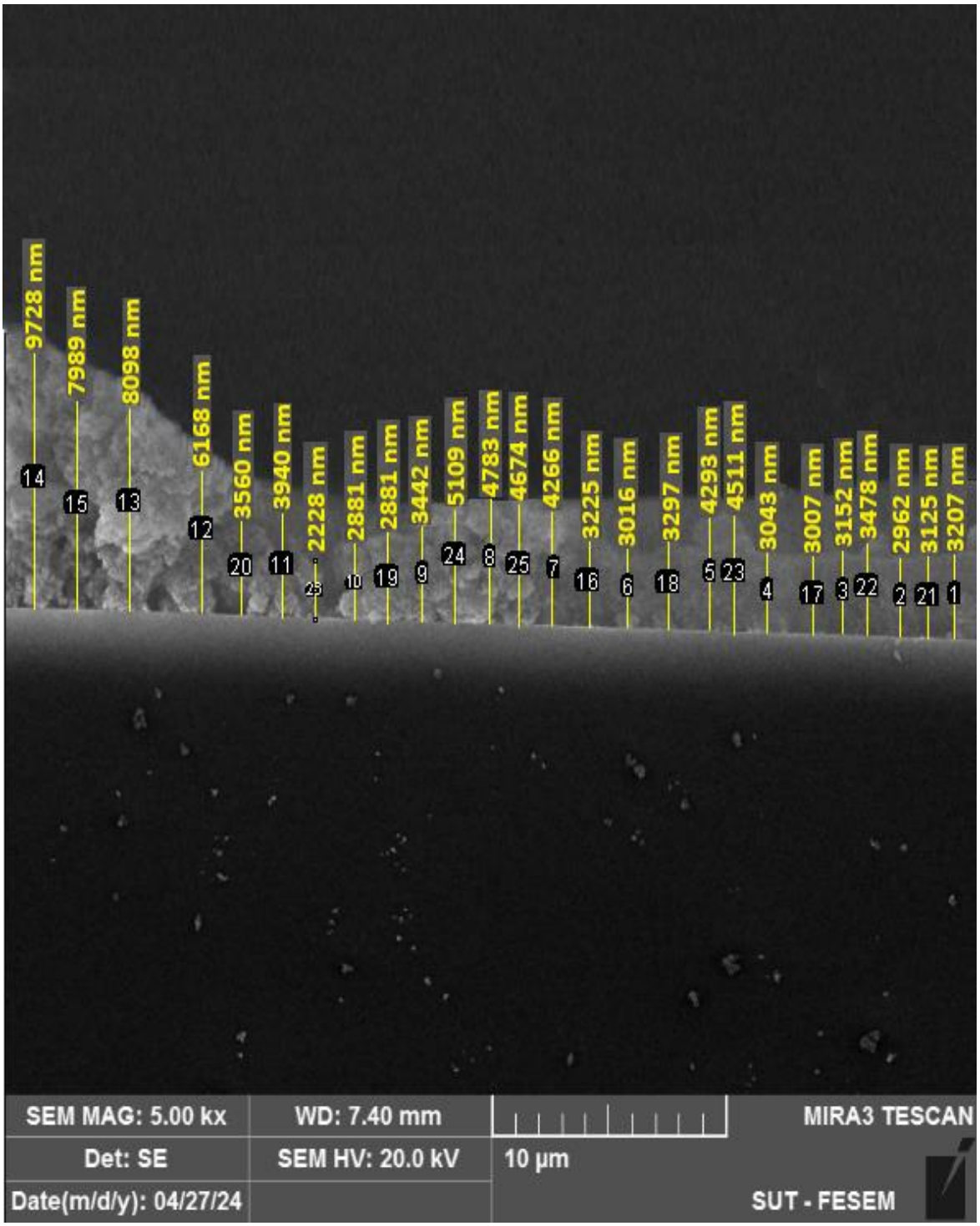

Figure 2.9: FE-SEM cross section image for the SiO_2/Au thin film where the SiO_2 added mass is 30 mg and an applied Current of 125 A.

2.6 Experimental Techniques

2.6.1 Optical Emission Spectroscopy

A calibrated Stellar Net spectrometer recorded the first spark of each sample at room temperature via an optical Fiber, which was connected to a computer to display the intensity of the plasma pulses over the 300-800 nm wavelength range, as shown in Figure 2.10.

The StellarNet spectrometer. These are popular, compact, fiber-optic spectrometers It is connected via USB to the laptop, which runs StellarNet's SpectraWiz software to control the spectrometer and acquire data in real-time, and save the spectra.

The fiber connecting the reaction vessel to the spectrometer is an optical fiber patch cable and it is inside a fiber optic probe. Which is a UV-VIS enhanced silicon fiber, optimized to transmit light efficiently across the ultraviolet, visible, and near-infrared spectral range, covering the major emission lines from a plasma in solution.

Lens Diameter: This probe tip typically has a collimating lens of (approx. 6.35 mm) in diameter.

The lens focuses the light from the plasma onto the tip of the optical fiber which is positioned at a Critical Angle of (~45-degree angle) relative to the plasma source. This is the best standard practice in emission spectroscopy to minimize the collection of two unwanted types of light.

2.6.2 X-Ray Diffraction

The thin film's structure is investigated by an ASENWARE (AW-XDM300) X-ray diffractometer displayed in Figure 2.11, where the radiation source is a Cu (Kα) with a wavelength of 0.154 nm and the current and voltage are 30 mA and 40 kV respectively. The diffraction patterns were reported within a range of 10° to 80° with a 3 degree/min speed.

2.6.3 Field Emission Scanning Electron Microscopy

FESEM imaging and EDS analysis were conducted in Baghdad in Photon Laboratory where the prepared thin films of SiO_2/Au samples were investigated using Field Emission Scanning Electron Microscopy (FESEM) and Energy Dispersive Spectroscopy (EDS) in a TESCAN MIRA3 field emission scanning electron microscope based in Czechia and equipped with an Oxford Instruments EDS detector.

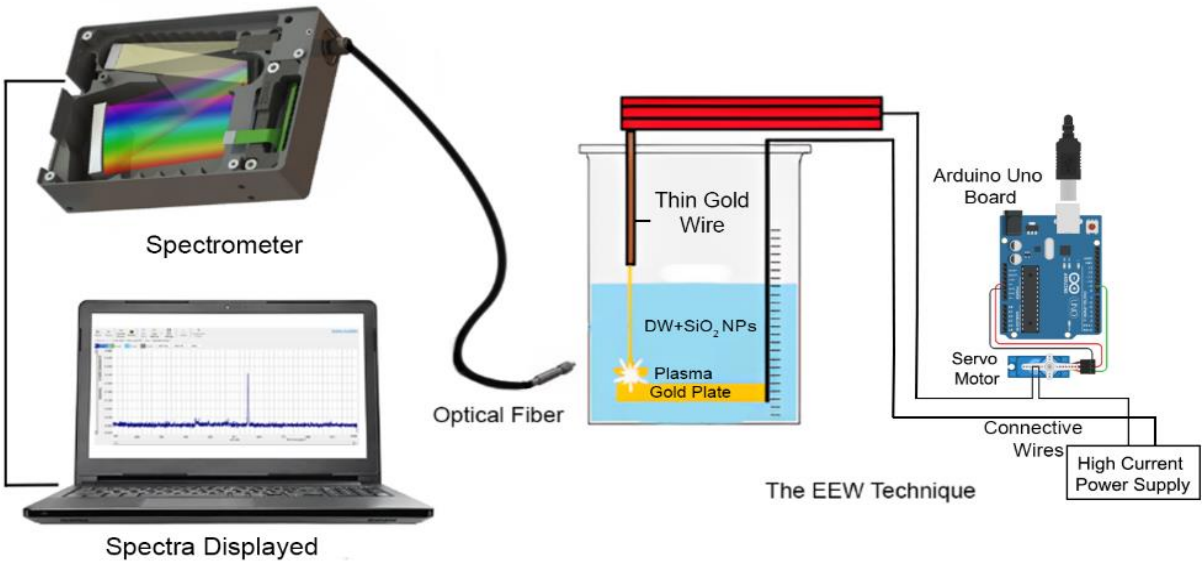

Figure 2.10: The optical emission spectroscopy.

2.6.4 Transmission Electron Microscopy

TEM analysis was carried out in Iran using a Zeiss EM 900 microscope as shown in Figure 2.12 to investigate the internal structure of the nanostructures.For the purpose of examining the fine details of the SiO_2/Au nanostructures, three samples were examined with SiO_2 mass of 25 mg and Applied current of 100, 125, 150 A.

2.6.5 Optical properties measurements

UV-Vis spectroscopy was performed in the postgraduate lab at Kerbala University using a UV-19000i spectrometer shown in Figure 2.13. The measurements were taken in the 300–1100 nm wavelength range using 1 cm quartz cuvettes where 2.5 ml of the liquid sample has been contained where distilled water served as the reference.

The spectra revealed surface plasmon resonance (SPR) peaks in the visible and near-infrared regions, along with interband transitions in the UV range. Tauc plots were used to determine direct bandgap energies, confirming the optoelectronic potential of the synthesized nanostructures.

Figure 2.11: The X-Ray diffractometer.

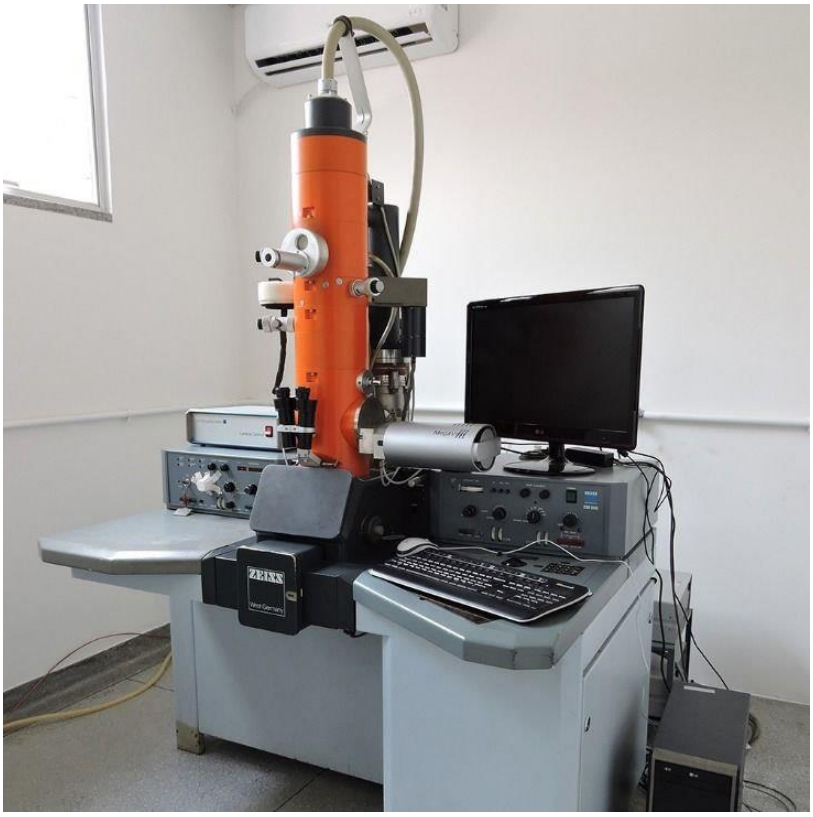

Figure 2.12: The transmission electron microscope.

Figure 2.13: The UV-Vis spectrometer.

3.1 Introduction

In this chapter the results of the experimental techniques used to diagnose the plasma and investigate the nanostructures properties has been analyzed. The discussed results involve the optical emission spectrum to analysis the plasma produced, the investigation investigated using X-ray diffraction pattern, field-emission scanning electron microscopy and transmission electron microscopy images, energy dispersive spectrum, and the UV-Visible spectrum. In addition to results conclusion, recommendation and future work.

3.2 The Optical Emission Spectrum (OES)

The emission spectrum of the gold plasma shown in Figures 3.1, 3.2, and 3.3 originates during the underwater electrical explosive wire technique. The wire electrode is only 0.3 mm in diameter with an applied currents intensities of 100, 125, and 150 A. The liquid medium of the SiO_2 colloidal suspension has 20, 25, and 30 mg of added silica . The displayed spectrum wavelength has a range of (300-800) nm. Each sample spectrum displays a notable ionic (II) and atomic (I) lines of Hα, O I, O II, Au I, Si I and Si II , O I, O II, Au I, Si I and Si II detailed in Table 3.1, where Hα refers to the Blamer series, where electron transition from n=3 to n=2 in the hydrogen atoms [85]. The ionic spectral lines of the silicon Si II, O II Si II (586.84) in particular displayed in Figures 3.4 and 3.5 both show red shifts and Figure 3.6 shows broadening throughout the spectra which is expected to be results of the stark

effect (electric field) although this shift also dependent on the electron temperature and density [86].

The effects of the current and the added SiO_2 mass were similar where both are directly proportional to the intensity of the peaks.

3.3 Measurements of Electron Temperature and Electron Density

The Boltzmann plot method has been chosen to determine the temperature of electrons of an equilibrium plasma. The wavelength of the light emitted depends on the energy difference between levels, while the peak intensity depends on the Boltzmann distribution for local thermal equilibrium [87].

The Si II peaks intensity, transition probability, statical weight, and upper energy level all displayed in Tables 3.2, 3.3, and 3.4 calculated from equation (1.11). The Boltzmann plots are shown in Figures 3.7, 3.8, and 3.9. Assuming a Boltzmann distribution of the atomic levels' population, The electron temperature T_e is evaluated from the inverse of the Boltzmann plot for the same upper level [88] [89].

The electron density has been calculated via the Stark width of the Hα spectral line following equation (1.13) [90].

Figures 3.10, 3.11, 3.12 and 3.13 show the Lorentzian fitting for the full width at half maximum (FWHM) to calculate the electron density in the plasma via the Stark broadening method for all samples with varying current values and SiO_2 masses, The full-width at half maximum decrease is noticeable, corresponding to the current lower values, which is a result of the reduced electron density. The electron temperature (T_e) and electron density (n_e) are

both identified in Figures 3.14, 3.15, and 3.16 for the corresponding current and SiO_2 mass values. The electron temperature T_e and the electron density n_e both exhibited a linear relationship with the applied current which aligns with the results of past studies [91]. However, the values of the electron temperature and density are significantly higher.

Table 3.1: The wavelength of the Hα, O I, O II, Au I, Si I and Si II peaks according to the national institute of standards and technology NIST [92].

Spectral Line	**Hα**	**O I**	**O II**	**Au I**	**Si I**	**Si II**
Wavelength λ	656.28	557.734	486.096	358.670	390.550	385.600
(nm)	---	77.190	515.999	404.09	615.51	412.807
	---	---	558.320	231.510	625.420	462.172
	---	---	576.100	443.730	700.360	504.100
	---	---	667.860	460.750	716.550	546.640
	---	---	690.644	479.26	742.350	566.960
	---	---	764.955	751.07	---	580.670
	---	---	---	---	---	586.840
	---	---	---	---	---	597.890
	---	---	---	---	---	634.710

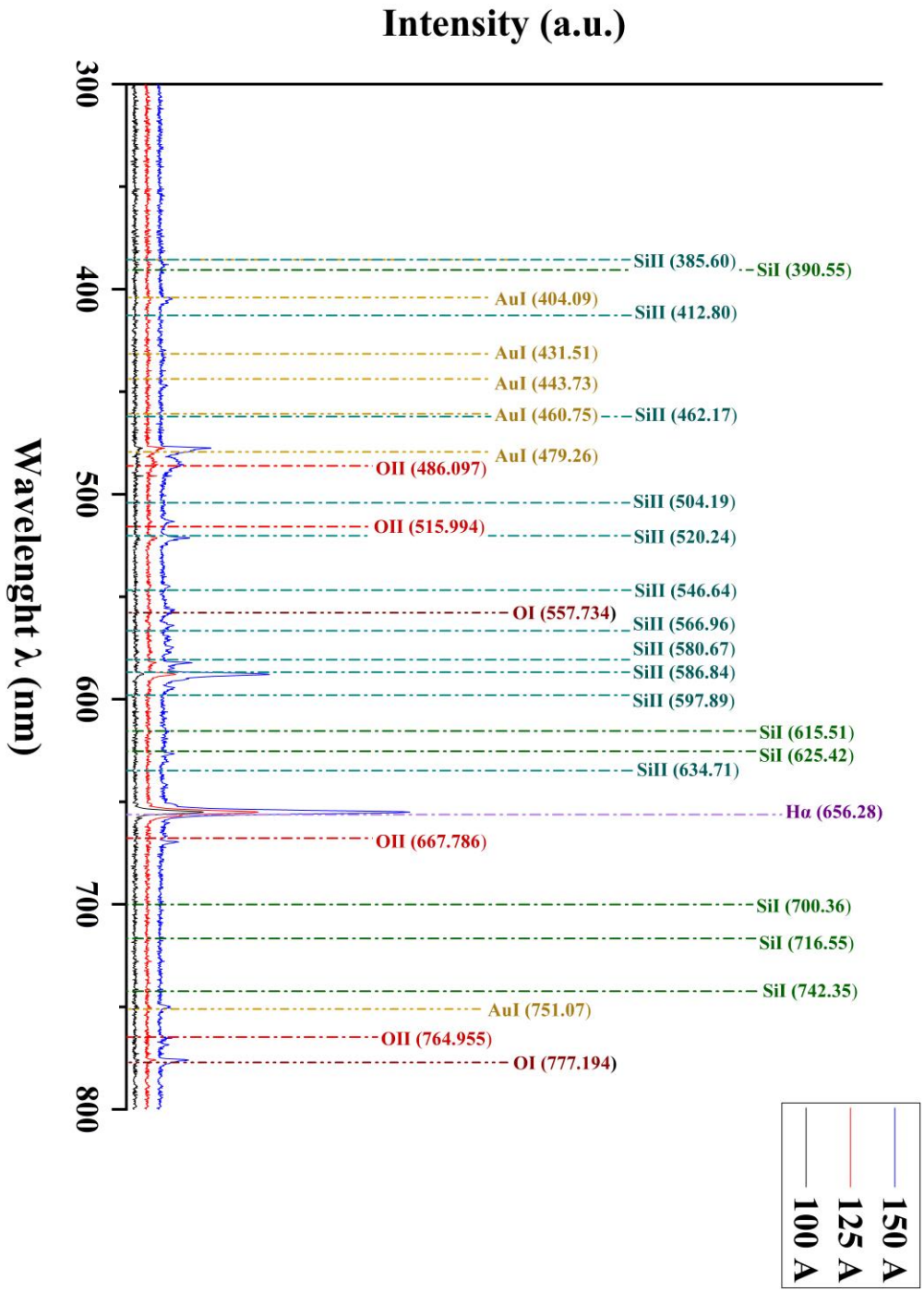

Figure 3.1: Emission spectra for gold wires with constant SiO_2 concentrations of 20 mg and the following currents: 100, 125, And 150 A, obtained by exploding wire.

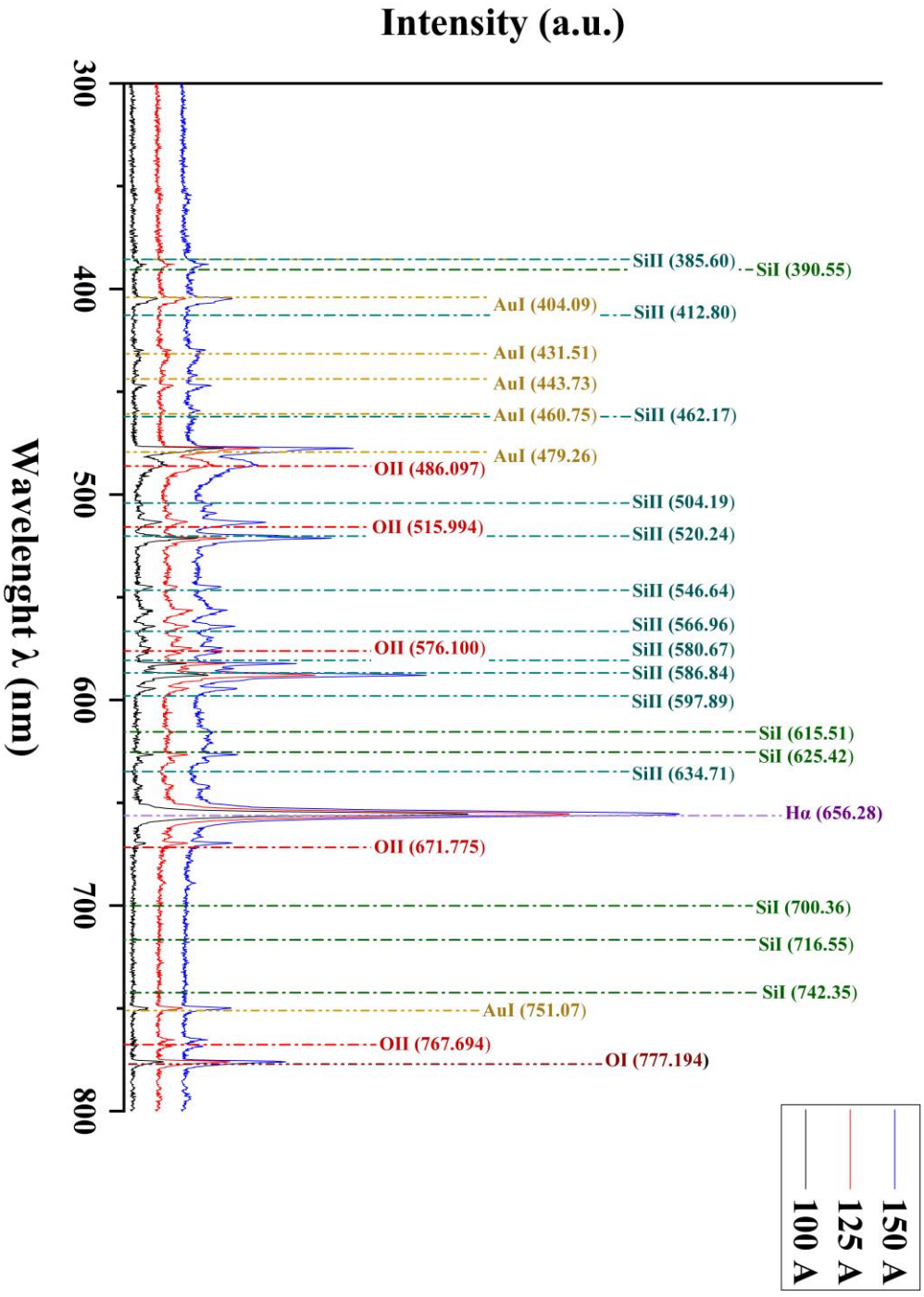

Figure 3.2: Emission spectra for gold wires with constant SiO_2 concentrations of 25 mg and the following currents: 100, 125, And 150 A, obtained by exploding wire.

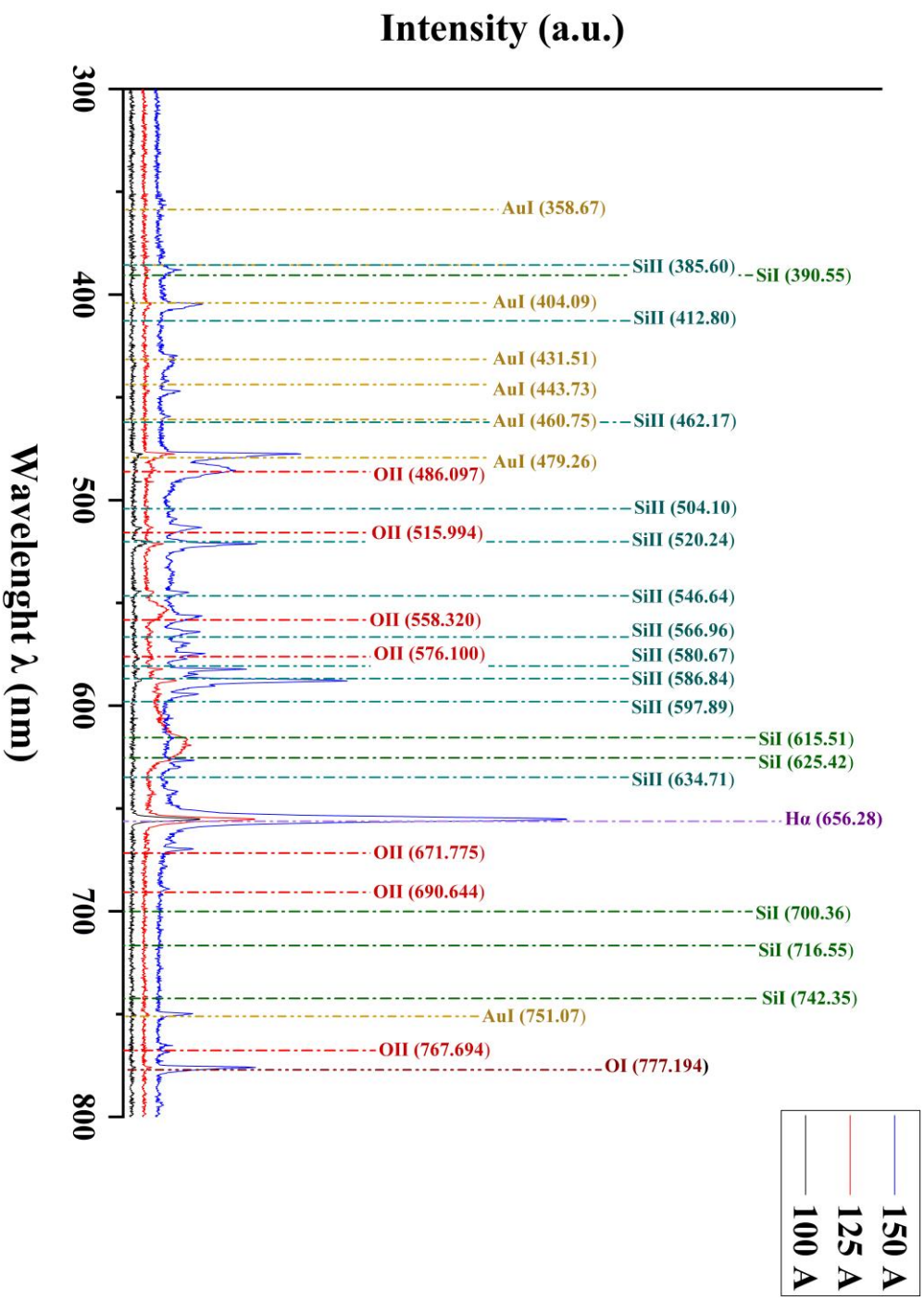

Figure 3.3: Emission spectra for gold wires with constant SiO_2 concentrations of 30 mg and the following currents: 100, 125, And 150 A, obtained by exploding wire.

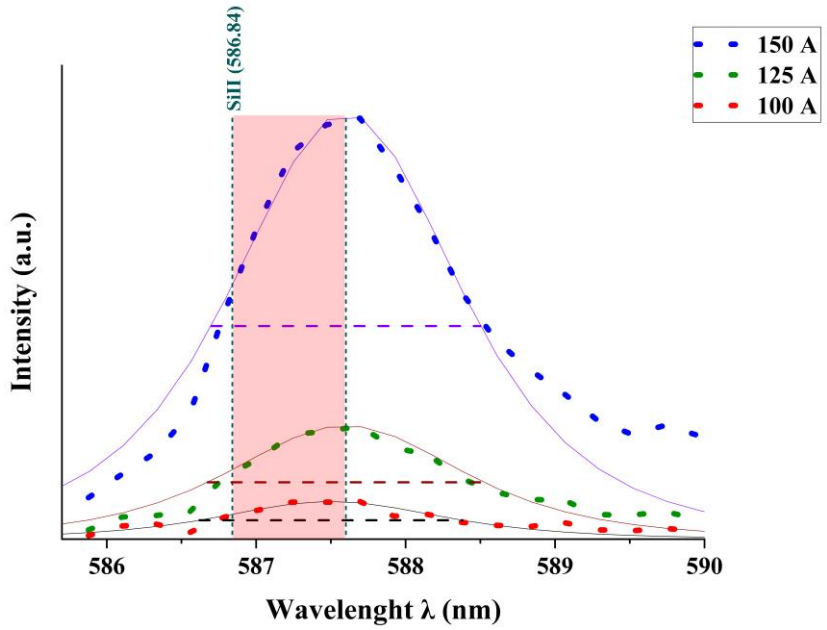

Figure 3.4: Peaks broadening and the Lorentzian fitting of Si II spectral line for 20 mg and the currents of 100, 125, and 150 A.

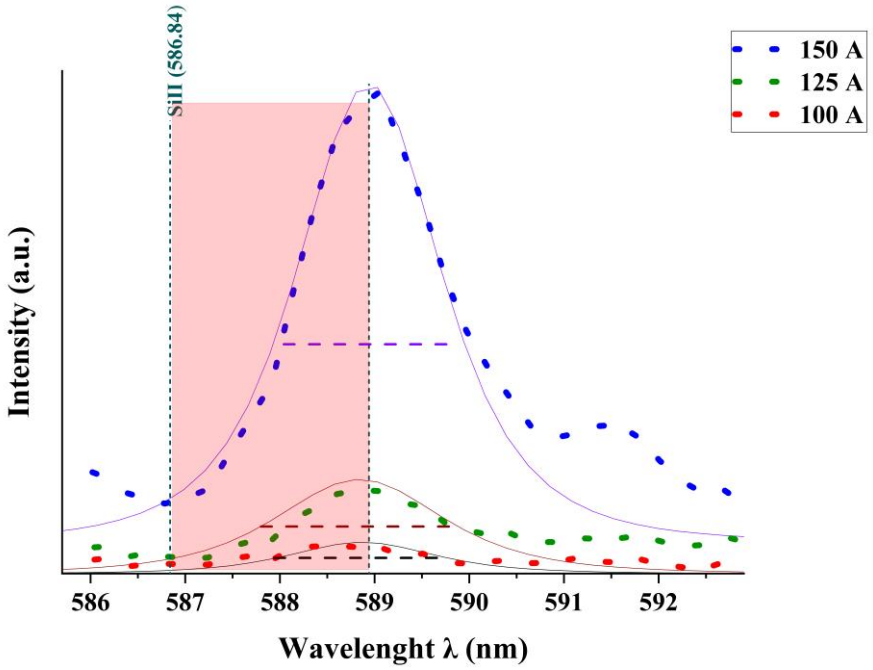

Figure 3.5: The red shift and the Lorentzian fitting of Si II spectral line for 25 mg and the currents of 100, 125, and 150 A.

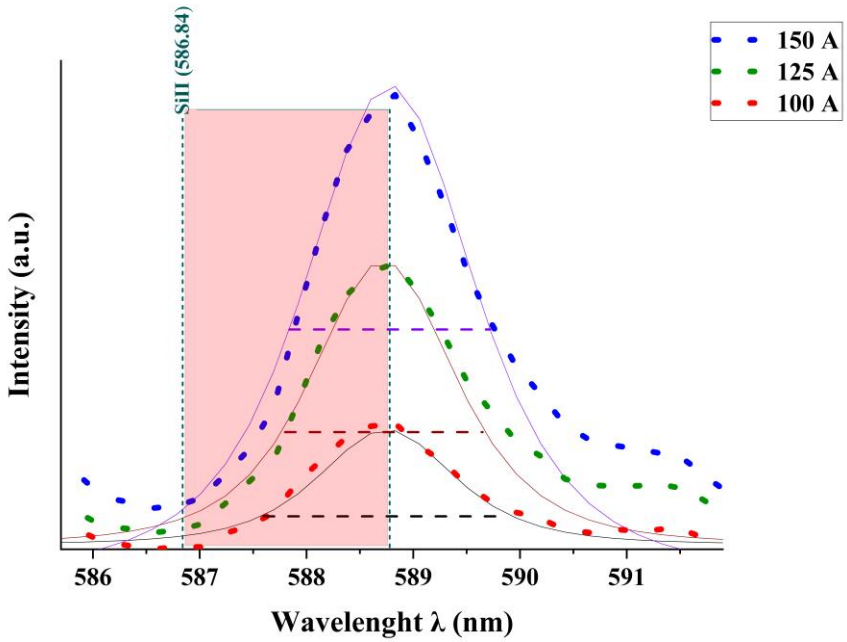

Figure 3.6: The red shift and the Lorentzian fitting of Si II spectral line for 25 mg and the currents of 100, 125, and 150 A.

Table 3.2: Shows the Si II wavelength, intensity , the product of A_{ji}. g_{ij} and the upper-level energy where the SiO_2 mass is 20 mg.

Applied current A	λ(nm) Observed	Intensity	A_{ji}. g_{ij} (s^{-1})	upper-level E_j (eV)	Ln(λji Iji/hcAji. gj)
100	385.602	0.023626	1.76E+08	10.07388	19.38166
	504.103	0.020844	2.80E+08	12.52526	19.06005
	546.643	0.0072	1.30E+08	14.79272	18.84534
	566.956	0.018129	4.00E+08	16.38604	18.68135
	597.893	0.015	2.26E+08	12.14699	19.11593
	634.71	0.0209	2.34E+08	10.07388	19.4726
125	385.602	0.030586	1.76E+08	10.07388	19.63987
	504.103	0.025957	2.80E+08	12.52526	19.27944
	546.643	0.009909	1.30E+08	14.79272	19.16469
	566.956	0.023246	4.00E+08	16.38604	18.92994
	597.893	0.020866	2.26E+08	12.14699	19.446
	634.71	0.024098	2.34E+08	10.07388	19.61499
150	385.602	0.030586	1.76E+08	10.07388	19.63987
	504.103	0.025957	2.80E+08	12.52526	19.27944
	546.643	0.009909	1.30E+08	14.79272	19.16469
	566.956	0.0243	4.00E+08	16.38604	18.97429
	597.893	0.01866	2.26E+08	12.14699	19.33426
	634.71	0.024098	2.34E+08	10.07388	19.61499

Table 3.3: Shows the Si II wavelength, intensity , the product of A_{ji}. g_{ij} and the upper-level energy where the SiO_2 mass is 20 mg.

Applied current A	λ(nm) Observed	Intensity	A_{ji}. g_{ij} (s^{-1})	upper-level E_j (eV)	Ln(λji Iji/hcAji. gj)
100	385.602	0.022629	1.76E+08	10.07388	19.33853
	504.103	0.020571	2.80E+08	12.52526	19.04689
	566.956	0.017614	4.00E+08	16.38604	18.6525
	597.893	0.016429	2.26E+08	12.14699	19.2069
	634.71	0.019171	2.34E+08	10.07388	19.38627
125	385.602	0.031743	1.76E+08	10.07388	19.67699
	504.103	0.031429	2.80E+08	12.52526	19.47072
	566.956	0.027926	4.00E+08	16.38604	19.11336
	597.893	0.023429	2.26E+08	12.14699	19.56185
	634.71	0.029229	2.34E+08	10.07388	19.80799
150	385.602	0.038091	1.76E+08	10.07388	19.85931
	504.103	0.037715	2.80E+08	12.52526	19.65304
	566.956	0.0342	4.00E+08	16.38604	19.31604
	597.893	0.028115	2.26E+08	12.14699	19.74417
	634.71	0.035074	2.34E+08	10.07388	19.99031

Table 3.4: Shows the Si II wavelength, intensity , the product of A_{ji}. g_{ij} and the upper-level energy where the SiO_2 mass is 30 mg.

Applied current A	λ(nm) Observed	Intensity	A_{ji}. g_{ij} (s^{-1})	upper-level E_j (eV)	Ln(λji Iji/hcAji. gj)
100	385.602	0.084259	1.76E+08	10.07388	20.65321
	504.103	0.066826	2.80E+08	12.52526	20.22509
	546.643	0.023281	1.30E+08	14.79272	20.01892
	566.956	0.059756	4.00E+08	16.38604	19.87408
	597.893	0.057772	2.26E+08	12.14699	20.46439
	634.71	0.061653	2.34E+08	10.07388	20.55436
125	385.602	0.099501	1.76E+08	10.07388	20.81949
	504.103	0.087725	2.80E+08	12.52526	20.4972
	546.643	0.03204	1.30E+08	14.79272	20.33825
	566.956	0.082768	4.00E+08	16.38604	20.19985
	597.893	0.079688	2.26E+08	12.14699	20.786
	634.71	0.088731	2.34E+08	10.07388	20.91846
150	385.602	0.188844	1.76E+08	10.07388	21.46024
	504.103	0.187185	2.80E+08	12.52526	21.25509
	546.643	0.0594	1.30E+08	14.79272	20.95555
	566.956	0.158445	4.00E+08	16.38604	20.84922
	597.893	0.133509	2.26E+08	12.14699	21.30204

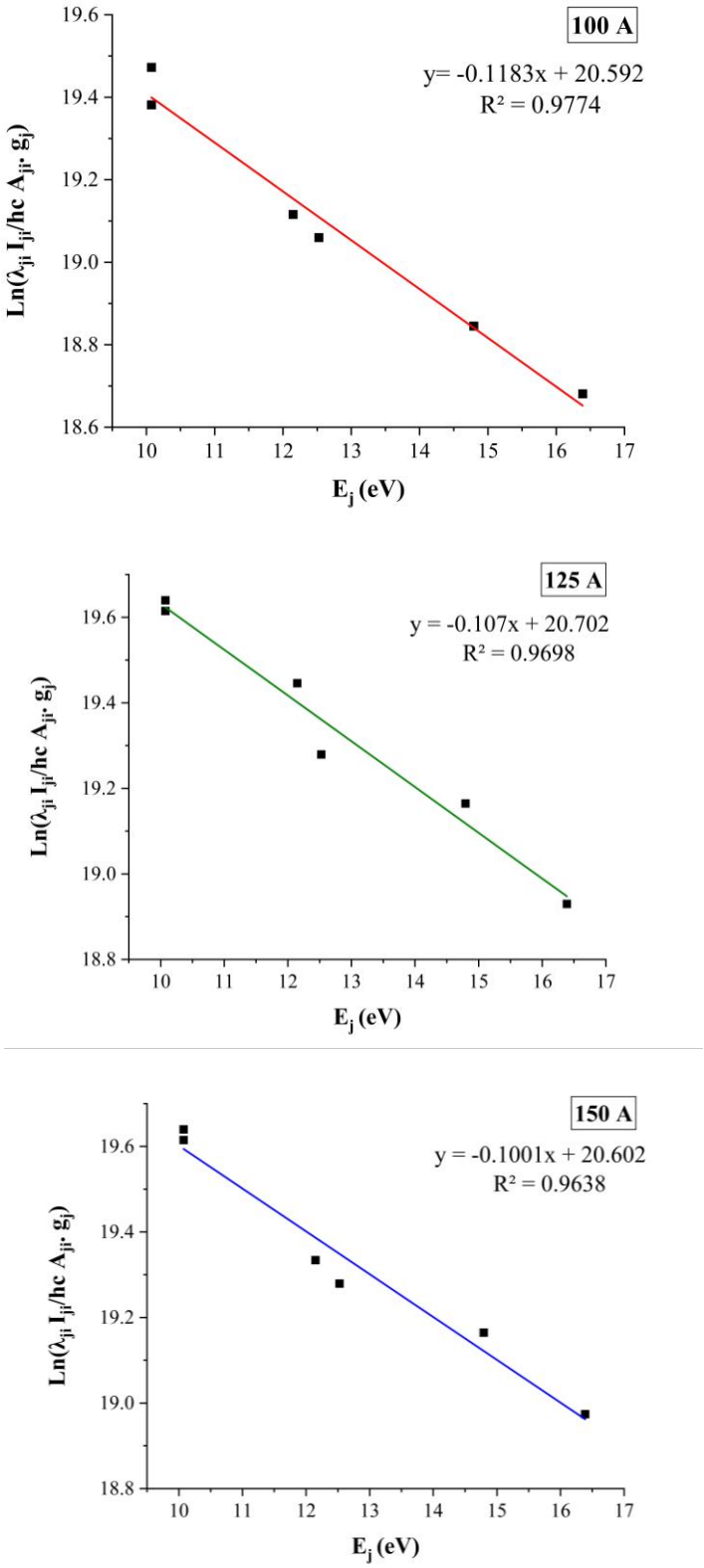

Figure 3.7: Boltzmann plots for SiO_2/Au lines generated by the explosion of au wires, where the SiO_2 mass is 20 mg and the current applied is 100, 125, and 150 A.

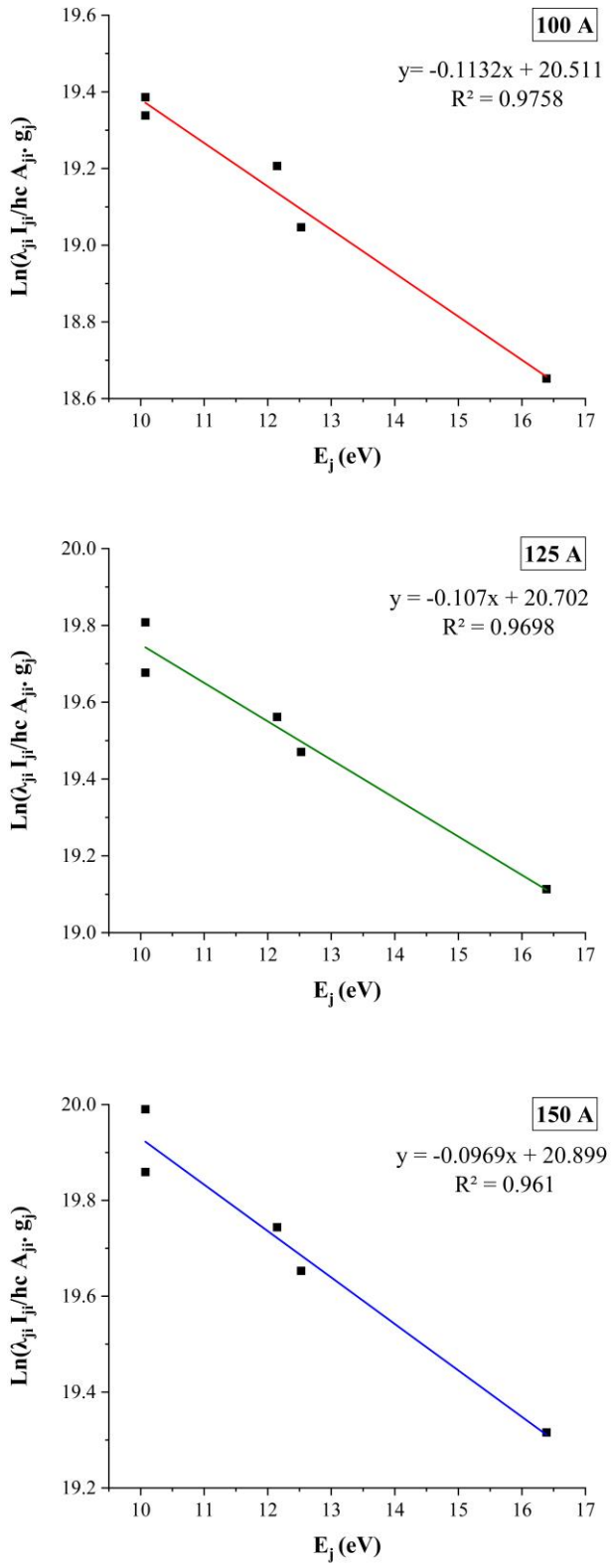

Figure 3.8: Boltzmann plots for SiO_2/Au lines generated by the explosion of au wires, where the SiO_2 mass is 25 mg and the current applied is 100, 125, and 150 A.

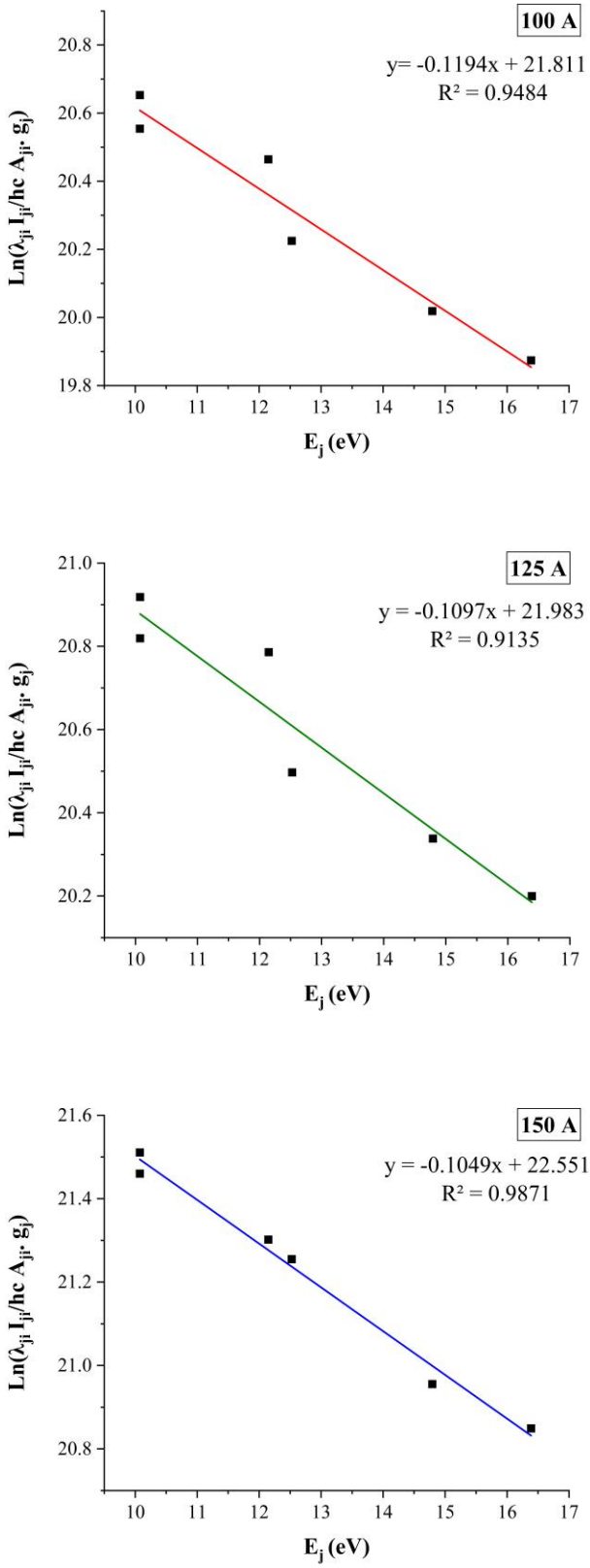

Figure 3.9: Boltzmann plots for SiO_2/Au lines generated by the explosion of au wires, where the SiO_2 mass is 30 mg and the current applied is 100, 125, and 150 A.

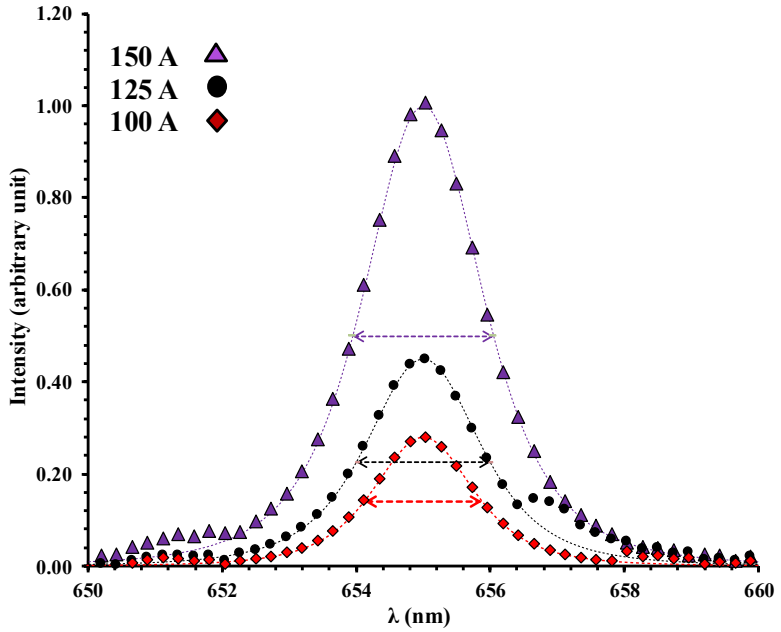

Figure 3.10: Peaks broadening and the Lorentzian fitting of Hα spectral line for 20 mg and the currents of 100, 125, and 150 A.

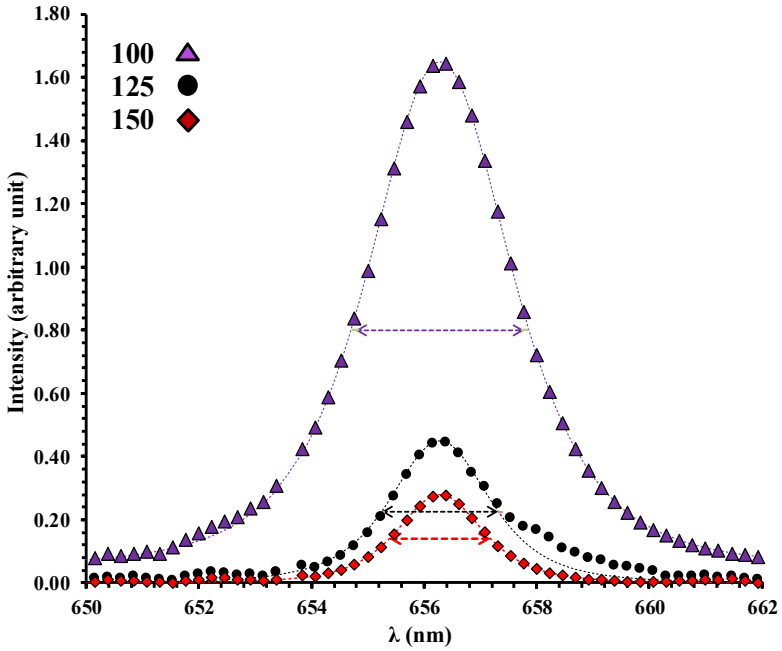

Figure 3.11: The Lorentzian fitting of Hα spectral line for 25 mg and the currents of 100, 125, and 150 A.

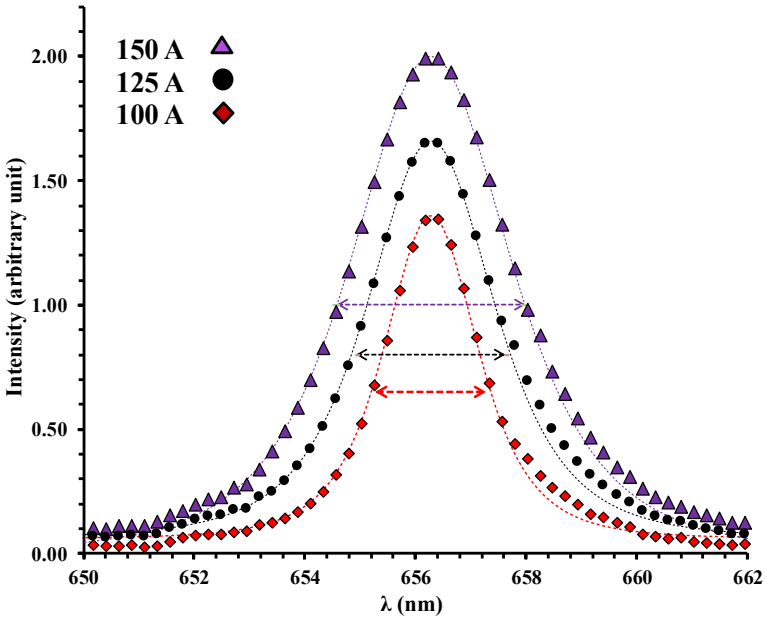

Figure 3.12: The Lorentzian fitting of Hα spectral line for 20 mg and the currents of 100, 125, and 150 A.

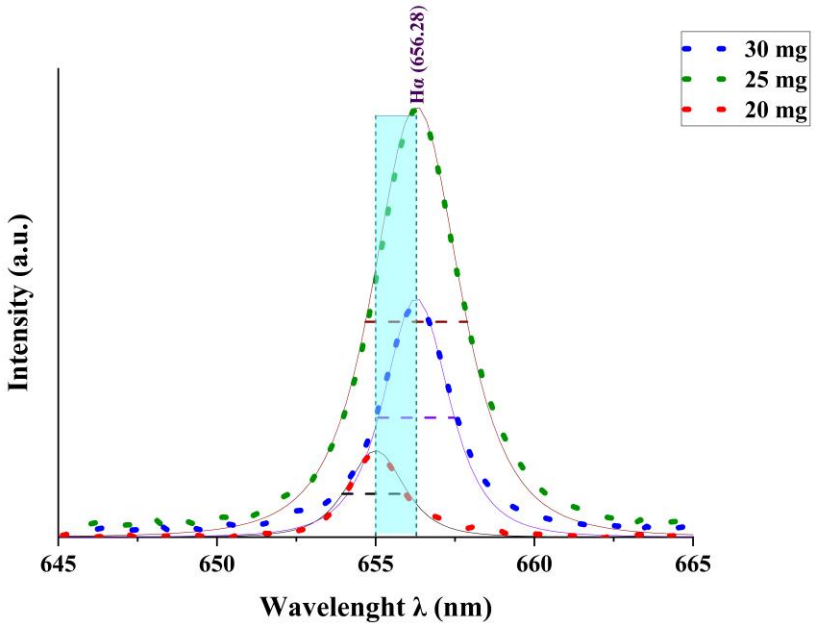

Figure 3.13: Peaks broadening and Their Lorentzian fitting of Hα spectral line for 125 A of applied current and the SiO_2 mass of 20, 25, and 30 mg.

The SiO_2 mass affected the electron temperature and electron density differently where the electron temperature was at its highest when SiO_2 mass was 25 mg, and the lowest T_e corresponded with the 30 mg mass. The

electron temperature decline at the 30 mg mass can be explained by the increased concentration of SiO_2 nanoparticles which in turn increase the cooling collisions between the dielectric nanoparticles, analogous to dusty plasma [93]. Meanwhile, the electron density relates directly with the SiO_2 mass, and that is due to the rising concentration of SiO_2 nanoparticles in the medium, which enhance the ionization as evident by the increased peaks intensity from the expiratory nanoparticle.

The Table 3.5 displays the Au plasma parameters, including the FWHM of Stark broadening, Debye length (λ_D) calculated from equation (1-1), Debye number (N_D) calculated from equation (1-2), and plasma frequency (f_p) calculated from equation (1-3), for Au plasma. The plasma frequency confirms a dense, conductive plasma, enhancing Au reduction and deposition. The short Debye length indicates strong electrostatic shielding and plasma stability. High Debye validate collective behavior. These parameters correlate with improved nanostructure quality numbers. the higher electron density and lower Dybe length at increased currents or SiO_2 mass enhance Au shell uniformity and crystallinity, as confirmed by XRD/TEM. This analysis underscores UEEW's precision for tailored synthesis.

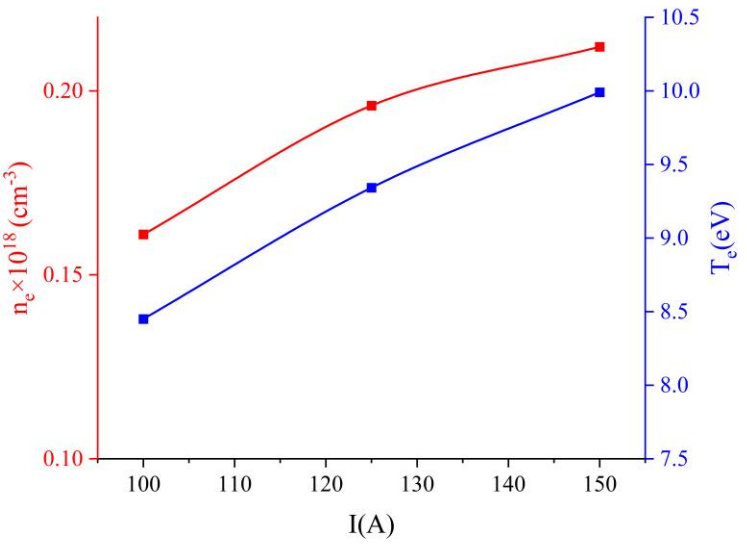

Figure 3.14: The temperature (blue line) and density (red line) of Electrons for the 20 mg SiO_2 mass and currents of 100, 125, and 150 A.

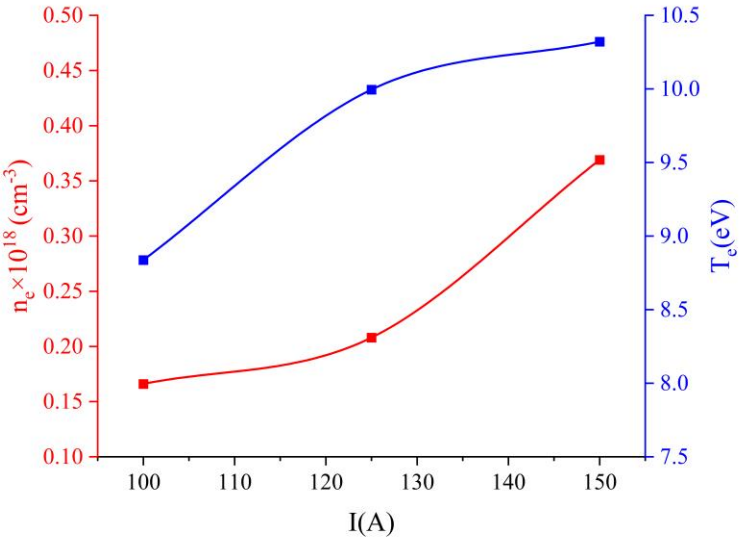

Figure 3.15: The temperature (blue line) and density (red line) of Electrons for the 25 mg SiO_2 mass and currents of 100, 125, and 150 A.

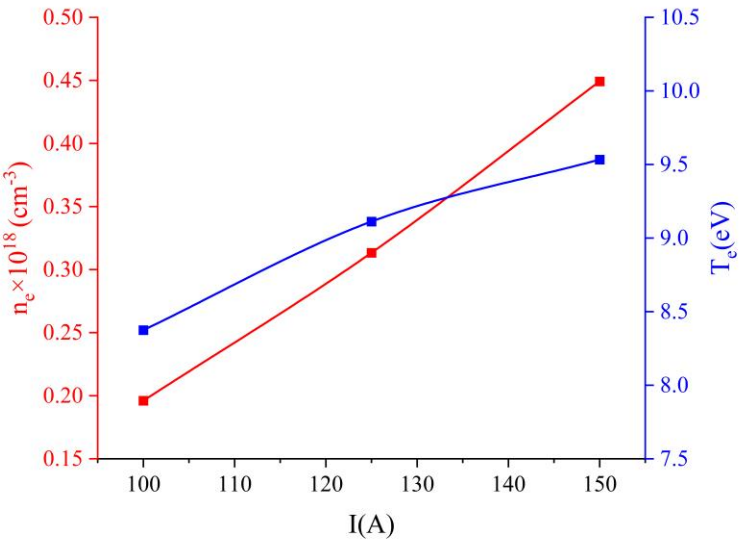

Figure 3.16:The temperature (blue line) and density (red line) of Electrons for the 30 mg SiO_2 mass and currents of 100, 125, and 150 A.

Table 3.5: Au Plasma parameters of UEEW calculated from the spectroscopy line intensity at a SiO_2 mass of 20, 25, and 30 mg for the applied currents of 100, 125, and 150 A.

SiO_2 mass (mg)	**I(A)**	**T_e (eV)**	**$n_e \times 10^{18}$ (cm^{-3})**	**FWHM (nm)**	**f_p (Hz) $\times 10^{10}$**	**$\lambda_D \times 10^{-5}$ (cm)**	**N_d**
	100	8.450	0.161	1.76	359.963	5.388	105283
20 mg	**125**	9.342	0.196	2.00	397.592	6.235	199002
	150	9.991	0.212	2.10	413.040	6.312	222845
	100	8.837	0.166	1.80	366.176	6.391	181793
25 mg	**125**	9.995	0.208	2.08	409.963	5.145	118916
	150	10.321	0.369	3.00	545.769	4.795	170525
	100	8.374	0.196	2.00	397.592	4.856	94039
30 mg	**125**	9.112	0.313	2.70	502.645	4.007	84425
	150	9.533	0.449	3.40	601.833	3.423	75463

3.4 The Structural Properties

The XRD analysis has been employed to determine the crystalline phases of the SiO_2/Au thin films, the crystalline structures present were identified and calculate the corresponding crystalline parameters.

The crystalline pattern of the synthesized nanostructures is displayed in Figure 3.17 and 3.18. The XRD pattern includes a cubic gold crystal with a space group of Fm-3m [94]. The cubic crystalline structure and the Miller indices of the diffraction peaks are reported in Table 3.6 and 3.7. The phase corresponding to the ICDD (International Centre for Diffraction Data) card number 96-901-1613 is identified as cubic gold The crystalline size values have been calculated using the Debye-Scherrer equation (1.15) [60]. These results demonstrate that UEEW synthesis parameters directly influence nanocrystalline quality. Higher currents improve Au crystallinity, while the SiO_2 mass (25 mg) which has the highest electron temperature minimizes defects and enhances core-shell uniformity. The analysis of the displayed pattern reveals a diminishing presence of the amorphous SiO_2 curve with the current increase, until it disappears entirely at I = 150 A, the nonlinear relationship between the current and the highest peak of Au (111) is observed in Table 3.6. The applied current effect may be explained by the enhanced Au shell coverage over the SiO_2 core because of the raised electron temperature, which immediately melts and deposits the Au onto the SiO_2 surface. This is the cause of the increased Au presence on the core, thereby increasing the crystalline size and decreasing the dislocation density.

The SiO_2 mass effect on the XRD pattern is identical to the applied current effect where the Amorphous SiO_2 structure reduced as the SiO_2 mass increase and that is a result of increasing number of SiO_2 nanoparticles in the colloidal

suspension which increase the probability of the Au encapsulation as evident by the higher Au peaks.

The linear relationship between the applied current and the intensity of the Au peaks agrees with the results of previous study [95]. However, our XRD pattern shows an Au (022) peak, which enhances the plasmonic effect applicable in the surface enhanced Raman spectroscopy (SERS) [96].

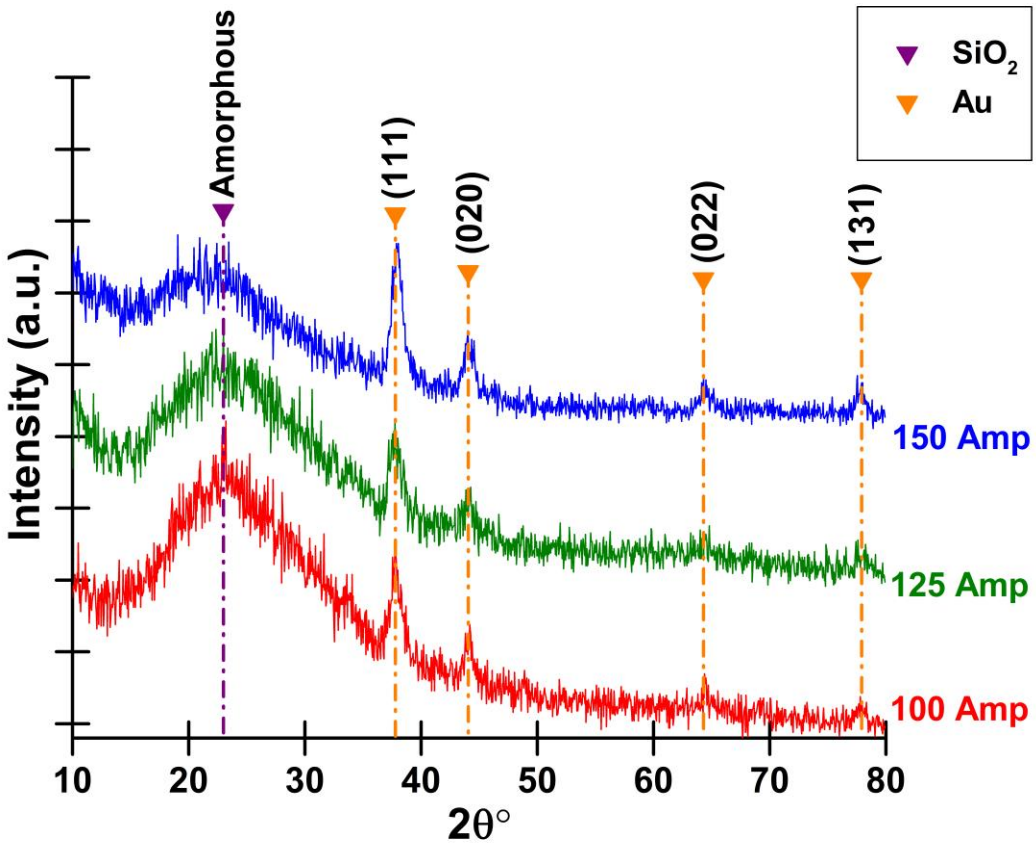

Figure 3.17: X-ray diffraction of SiO_2/Au nanostructures with a SiO_2 mass of 25 mg and currents of 100, 125, and 150 A.

Table 3.6: The crystalline parameters of SiO_2/Au nanostructure, where the SiO_2 Mass is 25 mg and the currents are 100, 125, and 150 A.

Current (A)	2θ	Miller index	FWHM (Rad)	d-spacing (Å)	Peak Intensity	Crystalline size (nm)	Dislocation Density (nm^{-2})
100	37.90	(111)	0.0113	2.34	48.2	12.915	0.0060
	44.05	(020)	0.0095	2.03	19.0	15.575	0.0041
	64.25	(022)	0.0087	1.43	4.7	18.779	0.0028
	77.90	(131)	0.0069	1.21	3.5	25.501	0.0015
125	37.70	(111)	0.0108	2.34	42.3	13.538	0.0055
	44.05	(020)	0.0095	2.03	12.0	15.575	0.0041
	64.25	(022)	0.0095	1.43	3.4	17.072	0.0034
	78.10	(131)	0.0052	1.21	2.9	34.085	0.0009
150	38.00	(111)	0.0104	2.34	65.3	13.995	0.0051
	44.05	(020)	0.0087	2.03	23.1	17.132	0.0034
	64.50	(022)	0.0087	1.43	5.3	18.779	0.0028
	77.80	(131)	0.0087	1.21	10.7	20.400	0.0024

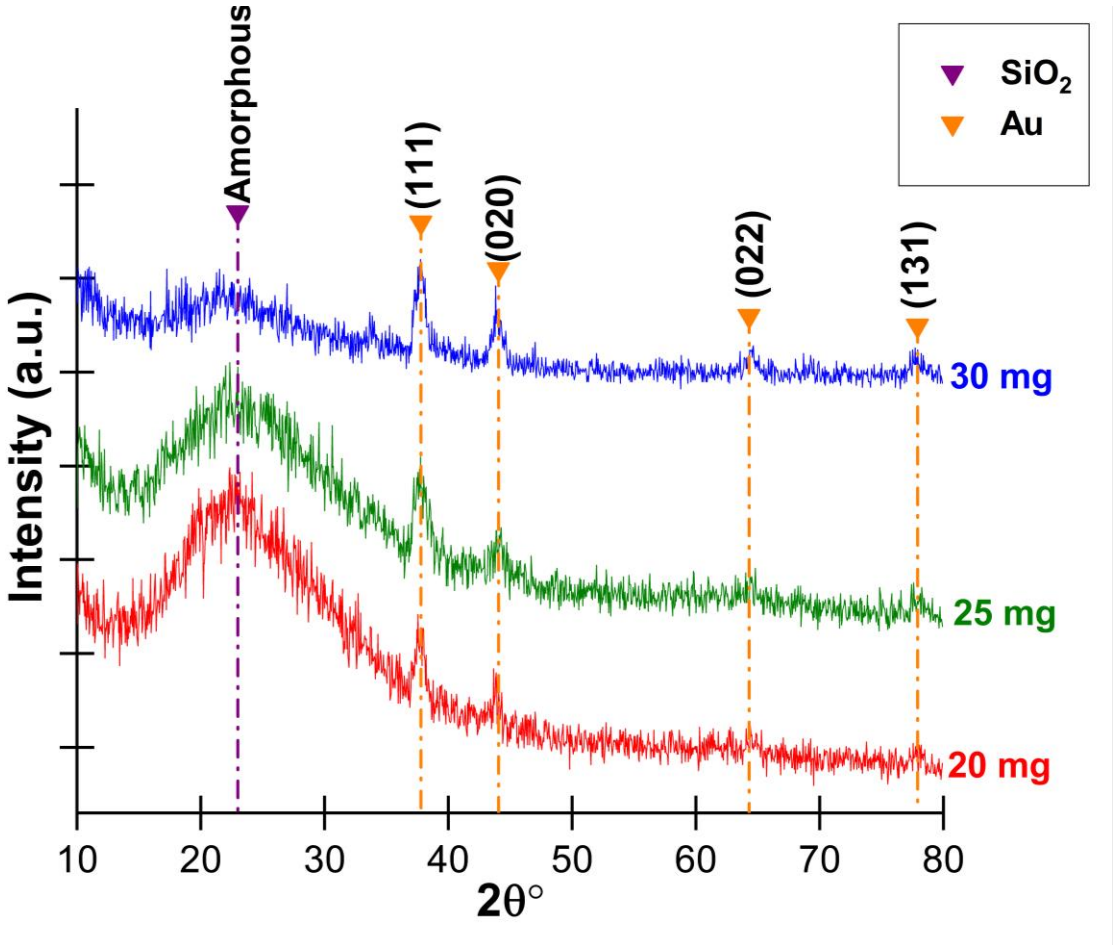

Figure 3.18: X-ray Diffraction of SiO_2/Au Nanostructures with an Applied Current of 125 A and SiO_2 Mass of 20, 25, and 30 mg.

Table 3.7: The crystalline parameters of SiO_2/Au nanostructure, where the applied current is 125 A and the SiO_2 mass of 20, 25, and 30 mg.

SiO_2 Mass (mg)	2θ	Miller index	FWHM (Radians)	d-spacing (Å)	Peak Intensity	Crystalline size (nm)	Dislocation Density (nm-2)
20	37.80	(111)	0.0096	2.34	31.5	15.261	0.0043
	44.05	(020)	0.0091	2.03	13.0	16.473	0.0037
	64.30	(022)	0.0073	1.43	5.1	22.332	0.0020
	78.10	(131)	0.0070	1.21	3.5	25.564	0.0015
25	37.80	(111)	0.0105	2.34	42.3	13.989	0.0051
	43.80	(020)	0.0087	2.03	6.0	17.118	0.0034
	64.40	(022)	0.0096	1.43	3.4	17.062	0.0034
	78.10	(131)	0.0052	1.21	2.8	34.085	0.0008
30	37.72	(020)	0.0093	2.34	62.0	15.833	0.0039
	43.80	(022)	0.0101	2.03	19.0	14.756	0.0045
	64.40	(131)	0.0087	1.43	5.2	18.769	0.0028
	77.75	(020)	0.0084	1.21	3.3	21.250	0.0022

3.5 Morphological Analysis and Elemental Composition

3.5.1 Field Emission Scanning Electron Microscopy and Energy Dispersive Spectroscopy

The morphology of the produced Thin Films have been investigated by the field emission scanning electron microscopy (FE-SEM) shown in the Figures 3.19, 3.20, 3.21, 3.22, and 3.23 which reveals the synthesis of SiO_2/Au Core@Shell spherical shaped nanostructures with a uniform size distribution and mean size of 32.8 nm for the 20 mg of SiO_2 mass, 28.98 nm for the 25 mg finally 26.17 nm for the 30 mg which shows an inverse relationship between the size of the nanostructures and the SiO_2 mass.

As for the applied current the mean sizes were 26.06 nm for the 100 A of applied current, 28.98 nm for the 125 A finally 39.17 nm for the 150 A, that illustrates a direct relationship between the size of the nanostructures and the applied current the elemental composition of the sample was studied via the Energy Dispersive Spectroscopy (EDS) displayed in Figure 3.24, 3.25, 3.26, 3.27. and 3.28 and the Tables 3.8 and 3.9 which informs us about elements present in the samples and the elemental mass and atomic percentages where the highest Au wt.% (Represents the mass contribution of each element relative to the total mass) and atomic% (Reflects the number of atoms of each element relative to the total atoms) corresponds with the 25 mg SiO_2 mass and 125 A of applied current.

The morphology information obtained is consistent with the previous literature [97]. However, the core-shell's Nanostructures size is significantly smaller, which enhances the Au shell's Localized Surface Plasmon Resonance (LSPR) effects, leading to various plasmonic applications, such as photocatalysis [98] [99].

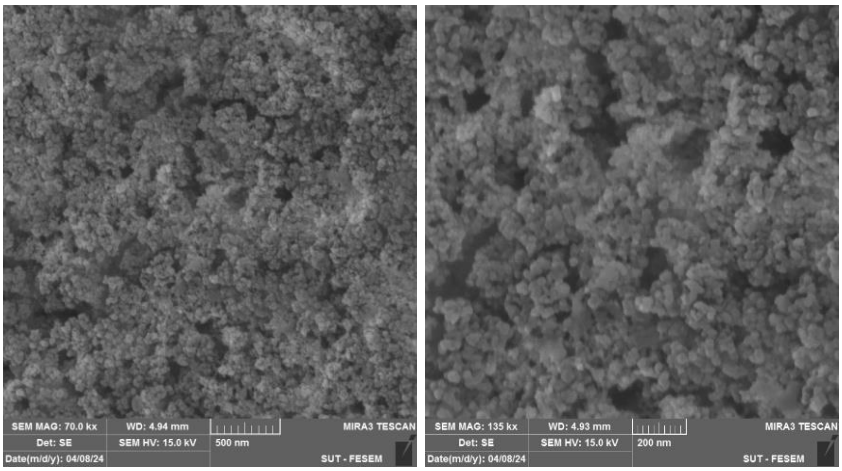

Figure 3.19: FE-SEM of SiO_2/Au thin film where the applied current is 100 A and the SiO_2 mass of 25 mg.

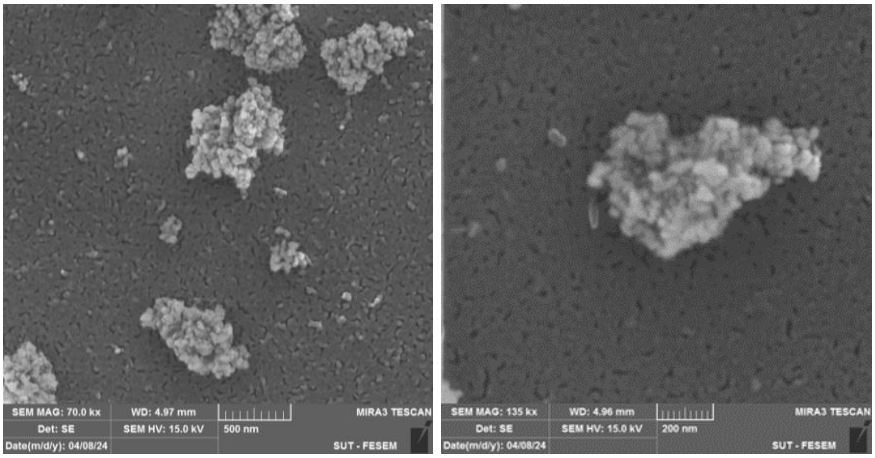

Figure 3.20: FE-SEM of SiO_2/Au thin film where the applied current is 125 A and the SiO_2 mass of 25 mg.

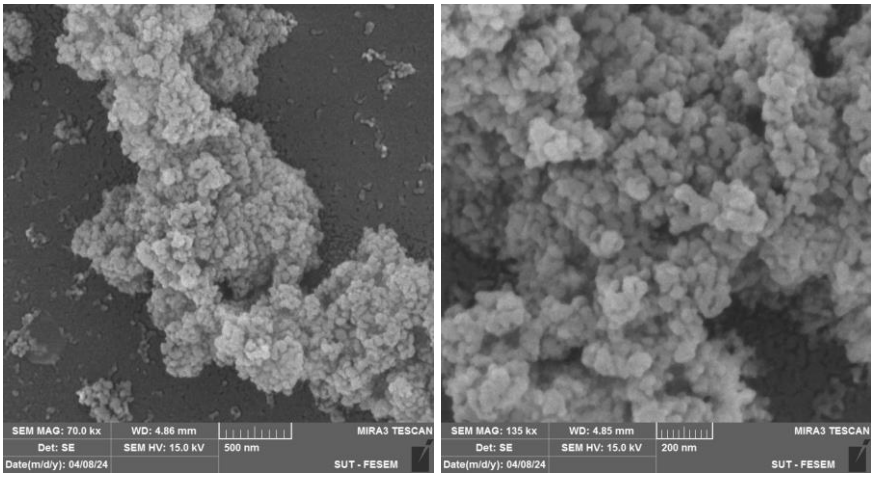

Figure 3.21: FE-SEM of SiO_2/Au thin film where the applied current is 150 A and the SiO_2 mass of 25 mg.

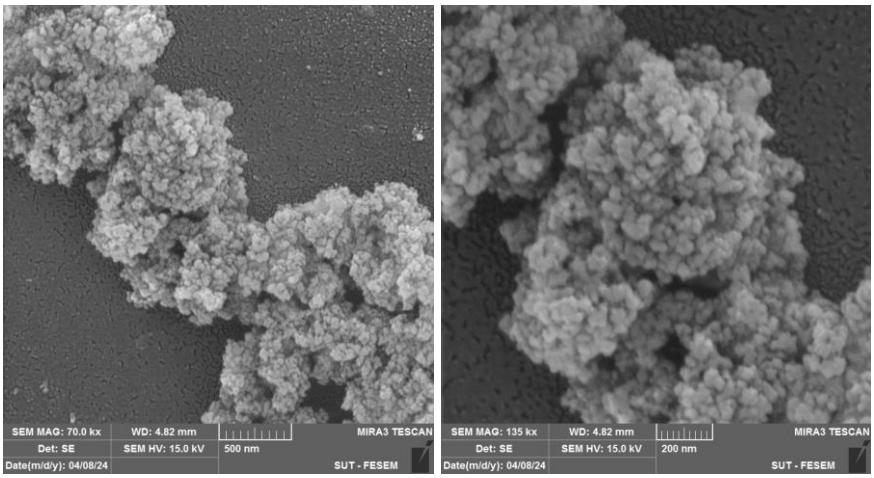

Figure 3.22: FE-SEM of SiO_2/Au thin film where the SiO_2 mass is 20 mg and the applied current is 125 A.

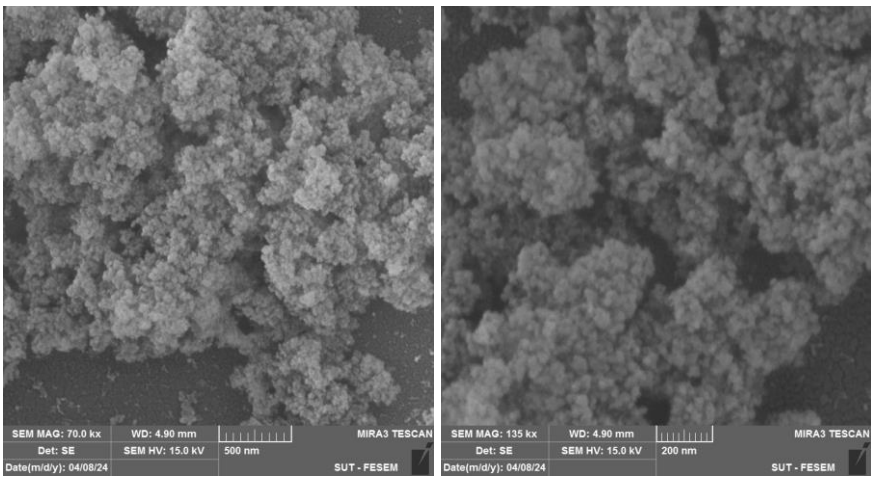

Figure 3.23: FE-SEM of SiO_2/Au thin film where the SiO_2 mass is 30 mg and the applied current is 125 A.

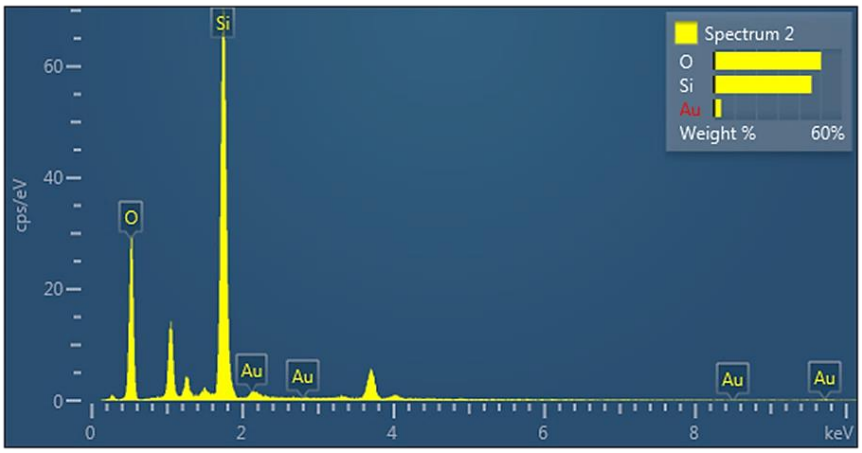

Figure 3.24: EDS of SiO_2/Au thin film where the applied current is 100 A and the SiO_2 mass of 25 mg.

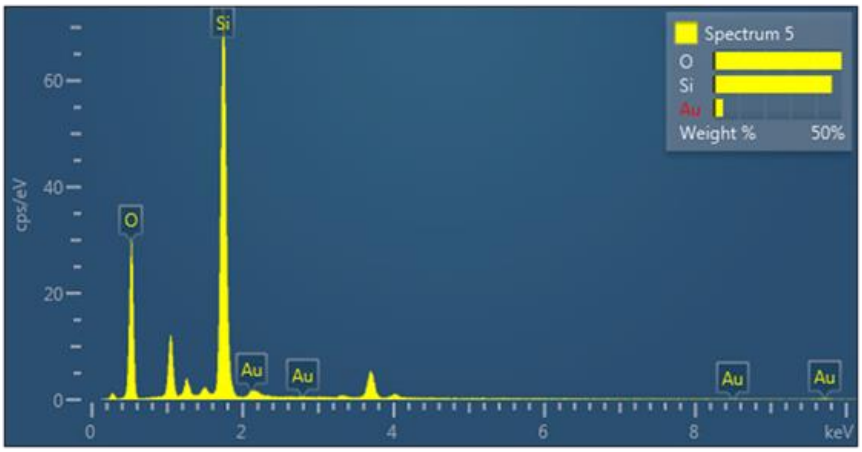

Figure 3.25: EDS of SiO_2/Au thin film where the applied current is 125 A and the SiO_2 mass of 25 mg.

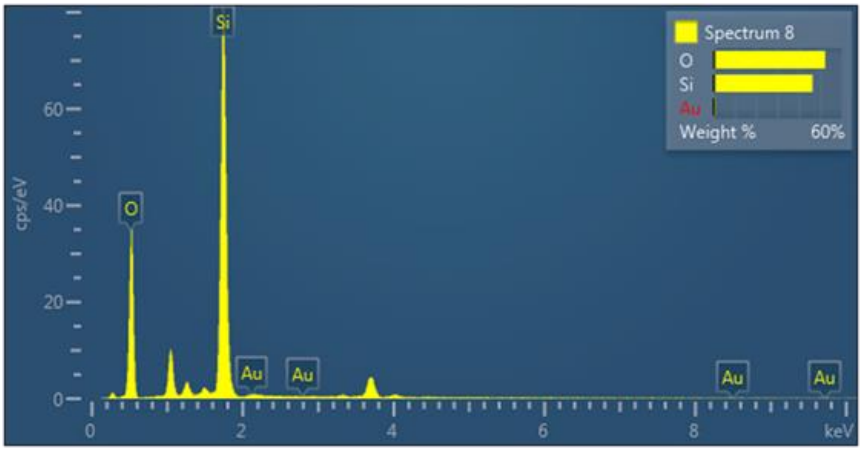

Figure 3.26: EDS of SiO_2/Au thin film where the applied current is 150 A and the SiO_2 mass of 25 mg.

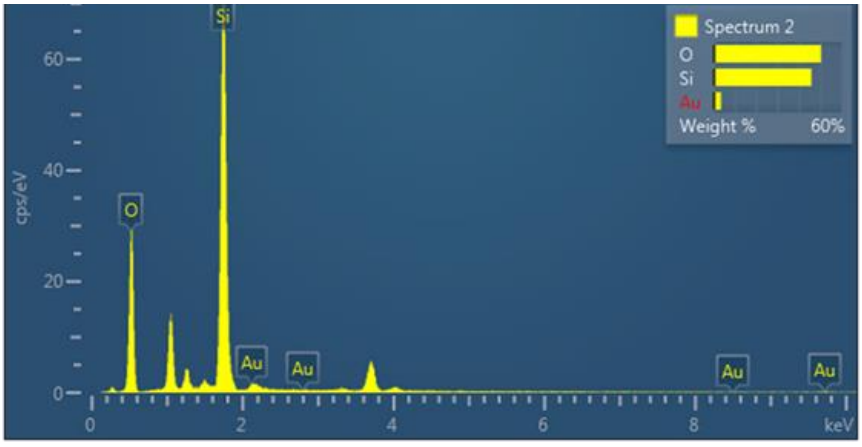

Figure 3.27: FE-SEM of SiO_2/Au thin film where the SiO_2 mass is 20 mg and the applied current is 125 A.

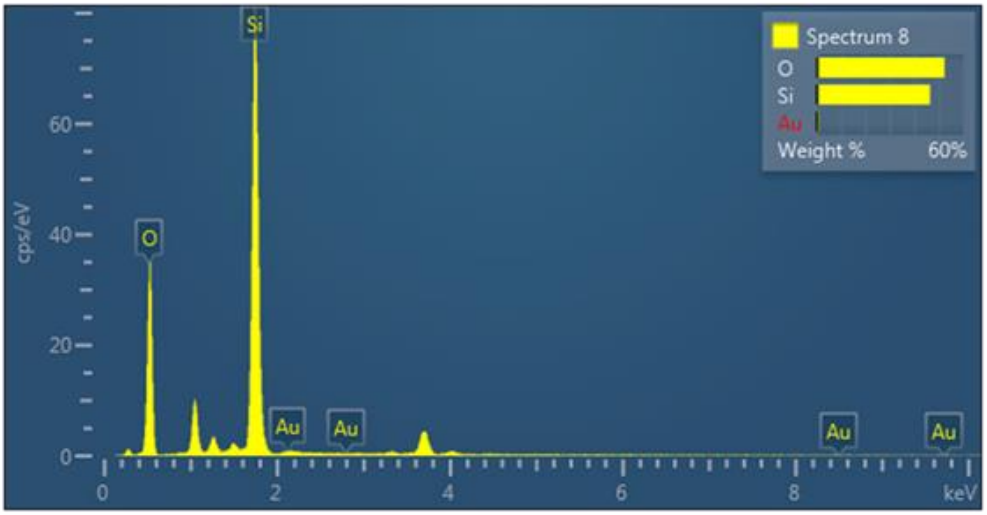

Figure 3.28: FE-SEM of SiO_2/Au thin film where the SiO_2 mass is 30 mg and the applied current is 125 A.

Table 3.8: EDS analysis of each SiO_2/Au sample the applied currents are 100, 125, and 150 A and the SiO_2 mass of 25 mg.

Current (A)	Element	Line Type	Wt.%	Atomic%	Mean size (nm)
100	O	K	50.38	65.59	26.68
	Si	K	45.88	34.02	
	Au	M	3.74	0.40	
125	O	K	49.91	65.23	28.98
	Si	K	46.14	34.35	
	Au	M	3.95	0.42	
150	O	K	52.27	66.30	39.17
	Si	K	46.46	33.57	
	Au	M	1.27	0.13	

Table 3.9: EDS analysis of each SiO_2/Au sample where the SiO_2 mass are 20, 25, and 30 mg and the applied current of 125 A.

SiO_2 mass (mg)	Element	Line Type	Wt.%	Atomic%	Mean size (nm)
20	O	K	59.96	72.47	32.80
	Si	K	39.98	27.52	
	Au	M	0.060	0.010	
25	O	K	49.91	65.23	28.98
	Si	K	46.14	34.35	
	Au	M	3.950	0.420	
30	O	K	51.62	65.61	26.17
	Si	K	47.35	34.28	
	Au	M	1.030	0.110	

3.5.2 Transition Electron Microscopy

The TEM images have been taken for the colloidal suspension with an applied current of 125 A, at magnifications of 16700 kx and 60000 kx. The darker spots in Figures 3.29, 3.30, and 3.31 represent the Au shell decorating the less apparent SiO_2 core, forming the Au@SiO_2 core-shell nanostructures in most of the sample. The nanostructures appear to be spherical and aggregated with a mean size of 21.07 nm, as shown in Figures 3.32 which agrees with the XRD results.

The shape of the nanostructures, as well as the particle size distribution, aligns with the previous research findings [100]. And yet, the metal shell encapsulation of the silica core is more distinct in our TEM images compared to their results, indicating a significant increase in the core-shell production.

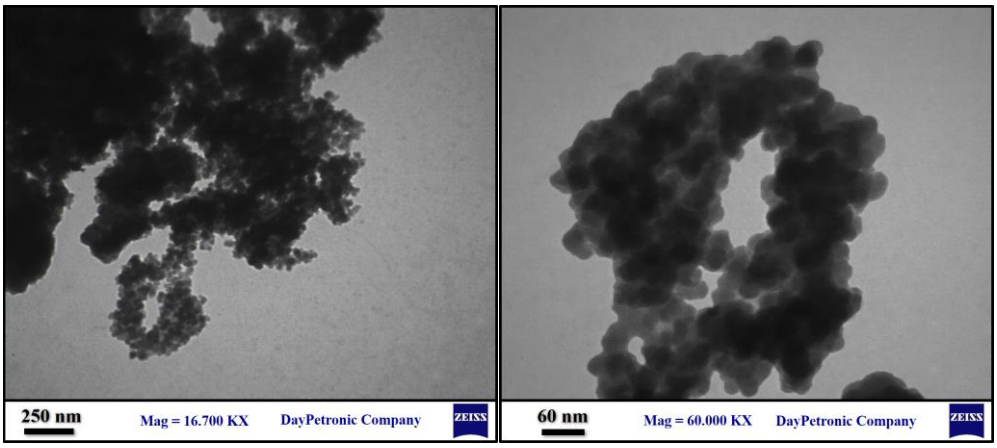

Figure 3.29: TEM images of the SiO_2/Au nanostructures where the SiO_2 mass is 20 mg and an applied current of 125 A.

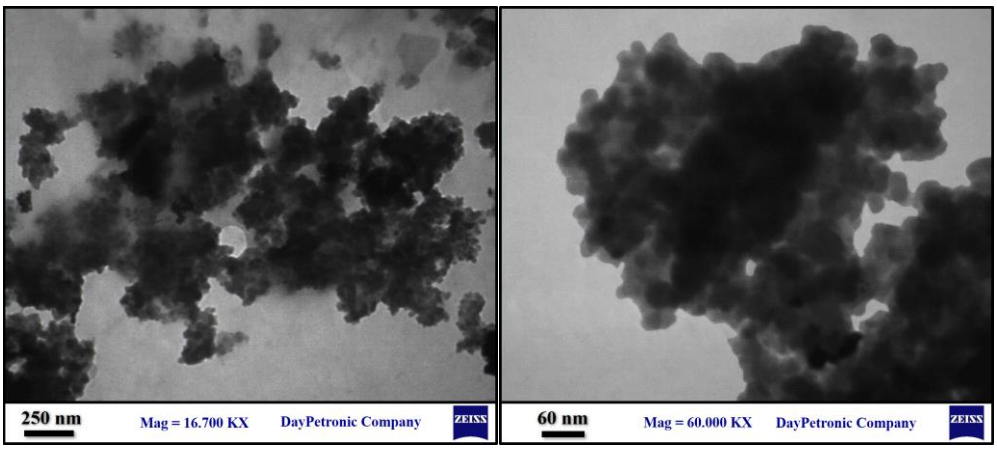

Figure 3.30: TEM images of the SiO_2/Au nanostructures where the SiO_2 mass is 25 mg and an applied current of 125 A.

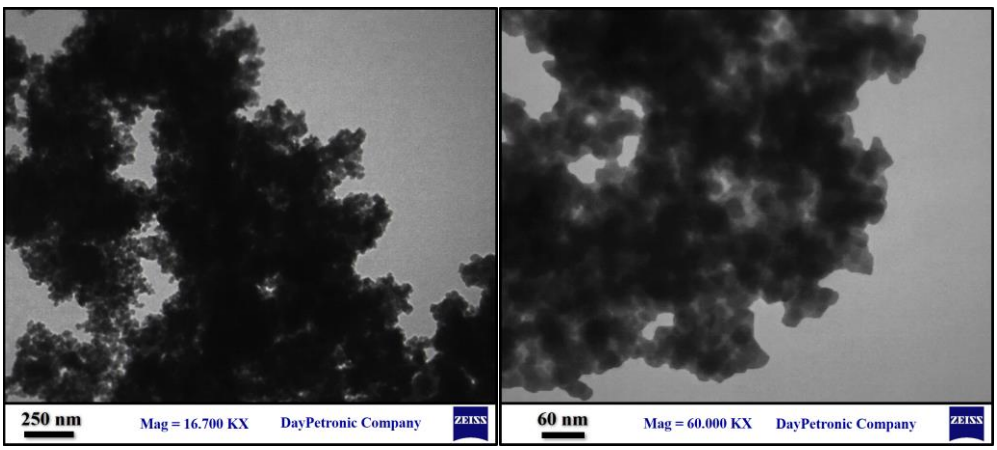

Figure 3.31: TEM images of the SiO_2/Au nanostructures where the SiO_2 mass is 30 mg and an applied current of 125 A.

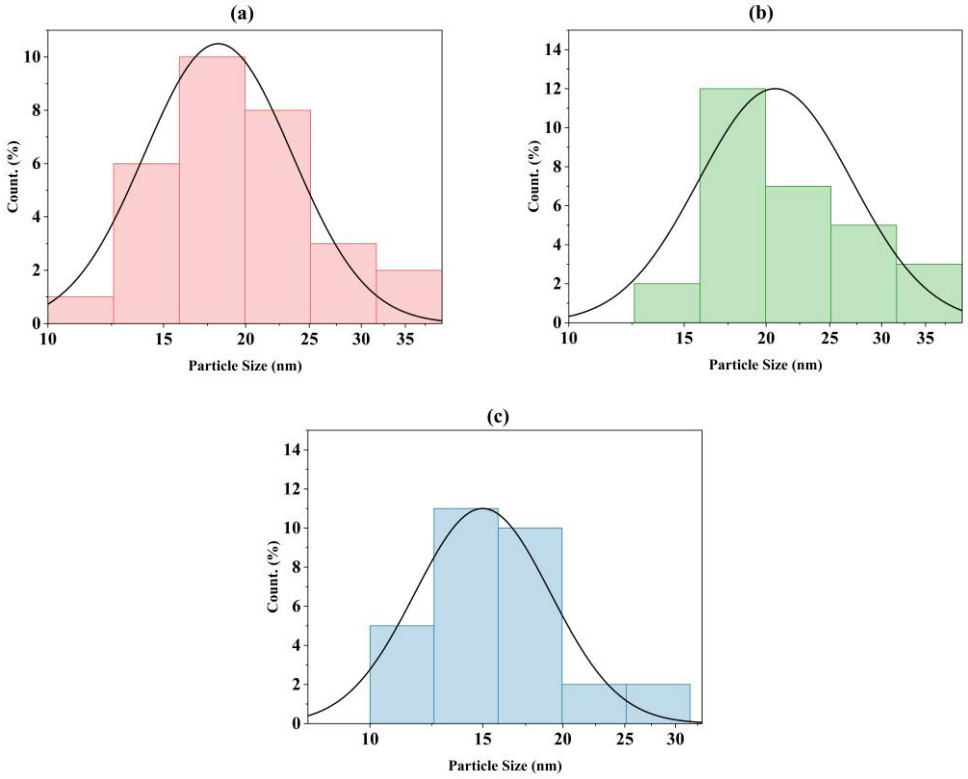

Figure 3.32: Particle size distribution of the SiO_2/Au nanostructures where the SiO_2 mass is (a) 20, (b) 25, and (c) 30 mg and an applied current of 125 A.

3.6 The Optical properties

UV-Vis spectroscopy was performed on the thin films to analyze the optical properties of the formed SiO_2/Au nanostructures. Figure 3.33 and 3.34 show the absorption, reflection, and transmission of each SiO_2 mass. The absorption peaks at the near ultraviolet region (λ_{20} =348, λ_{25} =378, λ_{30} =367 nm) may be a result of the interband transition which occur when electrons absorb or emit energy to move between the valence and conduction bands, typically requiring energy equal to the band gap. [101] such transition is expected to be a result of the outer Au shell [102], while the slight curve at the visable region (λ_{20} =550, λ_{25} =553, λ_{30} =550 nm) and the near infrared region peaks (λ_{20} =1007, λ_{25} =1007, λ_{30} =1004 nm) and similarly for λ_{100}, λ_{125},

and λ_{150} at the near ultraviolet region (λ_{100}=λ_{125}=λ_{150}=378 nm), at the visable region (λ_{100}=538, λ_{125}=537, λ_{150} =535 nm), and the near infrared region peaks (λ_{100}=1005, λ_{125}=1004, λ_{150}=1005 nm). Those are sigins of the Local Surface Plasmon Resonance (LSPR) which is a phenomenon where conduction electrons in metallic nanoparticles oscillate collectively in response to incident light, leading to strong absorption and scattering at specific wavelengths. LSPR is highly sensetive to the nanostructures propertirs. [103] The red shift in the LSPR peaks towards the near infrared region and the broader peaks at the visiable light region may be due to the sample aggregation effect [104] visible in the FE-SEM and TEM images.

The linear relation between the absorption values and the SiO_2 mass as well as the applied current has been remarked. In contrast, the Reflection (R) and Transmission (T) values (calculated from equation (1-19) and equation (1-20)) decreased as the SiO_2 mass increased, in addition to the intensity dips corresponding to the absorption peaks. Tauc plot was utilized to calculate the energy gap of the formed nanostructures, in which we noted that all the samples allowed a direct energy gap E_g where r=2 (calculated from equation (1.18)) displayed in Figure 3.35 and 3.36.

The visible region surface plasmon peaks location and intensities, as well as the relation between the energy gap and the size of the nanostructures, are in line with previous studies [105]. However, the near-UV regions interband transition peaks are absent for the Au NPs. The interband transition in the Au shell can be utilized in solar energy conservation [106].

The excitation coefficient (k) (calculated from equation (1-21)) as shown in Figure 3.37 and 3.38, k peaks intensity increased with the applied current, the refractive index (n) (calculated from equation (1-22)) displayed in Figures 3.39 and 3.40 is inversely proportional to the SiO_2 mass and the applied current which shows similar dips as the reflection and transmission intensities: the average n values (2.187, 2.201, 2.191, and 2.198) are suitable for antireflection coating, which is particularly important in solar cells [107].

The optical conductivity (σ) (calculated from equation (1-23)) was presented in Figures 3.41 and 3.42 increased with the SiO_2 mass and the applied current. The highest values of σ were in the Near-UV region, an essential quality for UV photodetectors. The real and imaginary dielectric constants ε_1 and ε_2 (calculated from equation (1-24) and equation (1-25)) are demonstrated in Figure 3.43 and 3.44, where their highest values were in the NIR region. While the ε_1 exhibited a peak in that region, there was a dip for ε_2. The dielectric constants relate differently to the SiO_2 mass and the applied current where ε_2 is directly proportional to the SiO_2 mass applied current and ε_1 is the opposite. The high values of the dielectric constants in the NIR region allow the nanostructures to be employed in the telecomunications field, such as optical switching [108].

The average values of the optical properties calculated from the UV-Vis spectroscopy are all presented in Table 3.10 and 3.11.

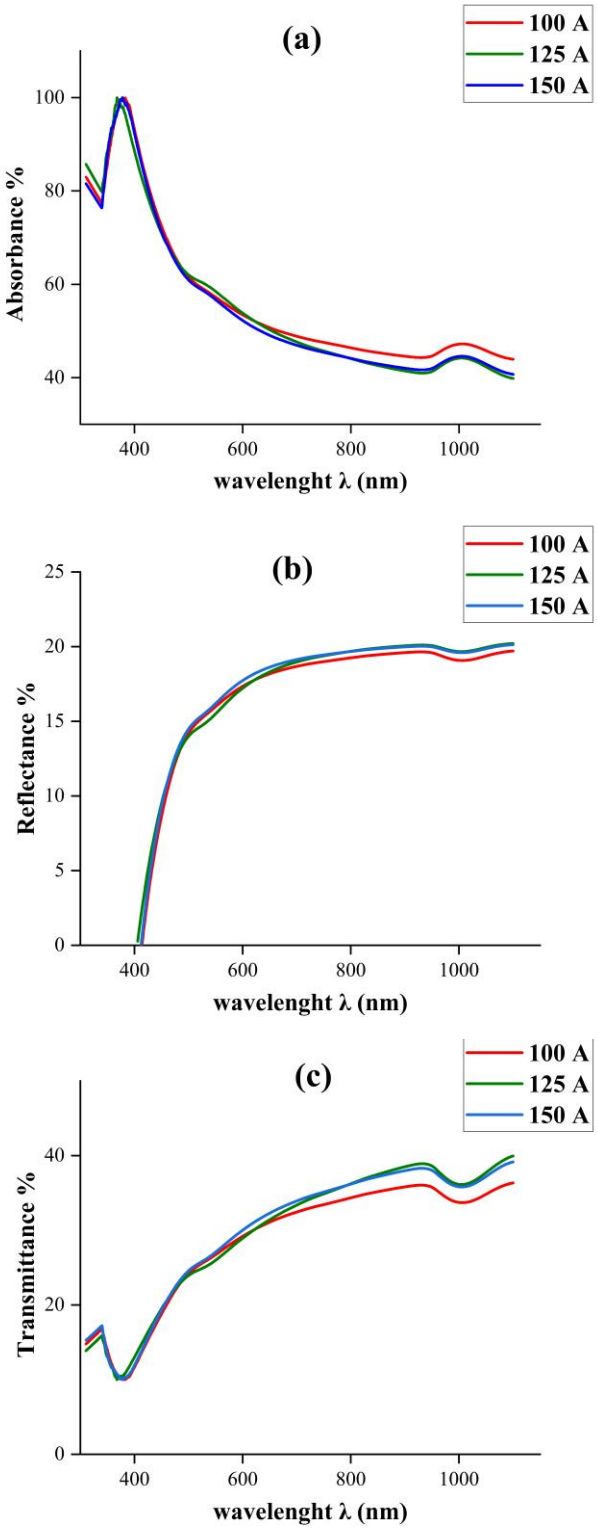

Figure 3.33**:** (a) Absorption, (b) Reflection, and (c) Transmission spectra of the SiO_2/Au samples where the current applied is 100, 125, and 150 A and SiO_2 mass is 25 mg.

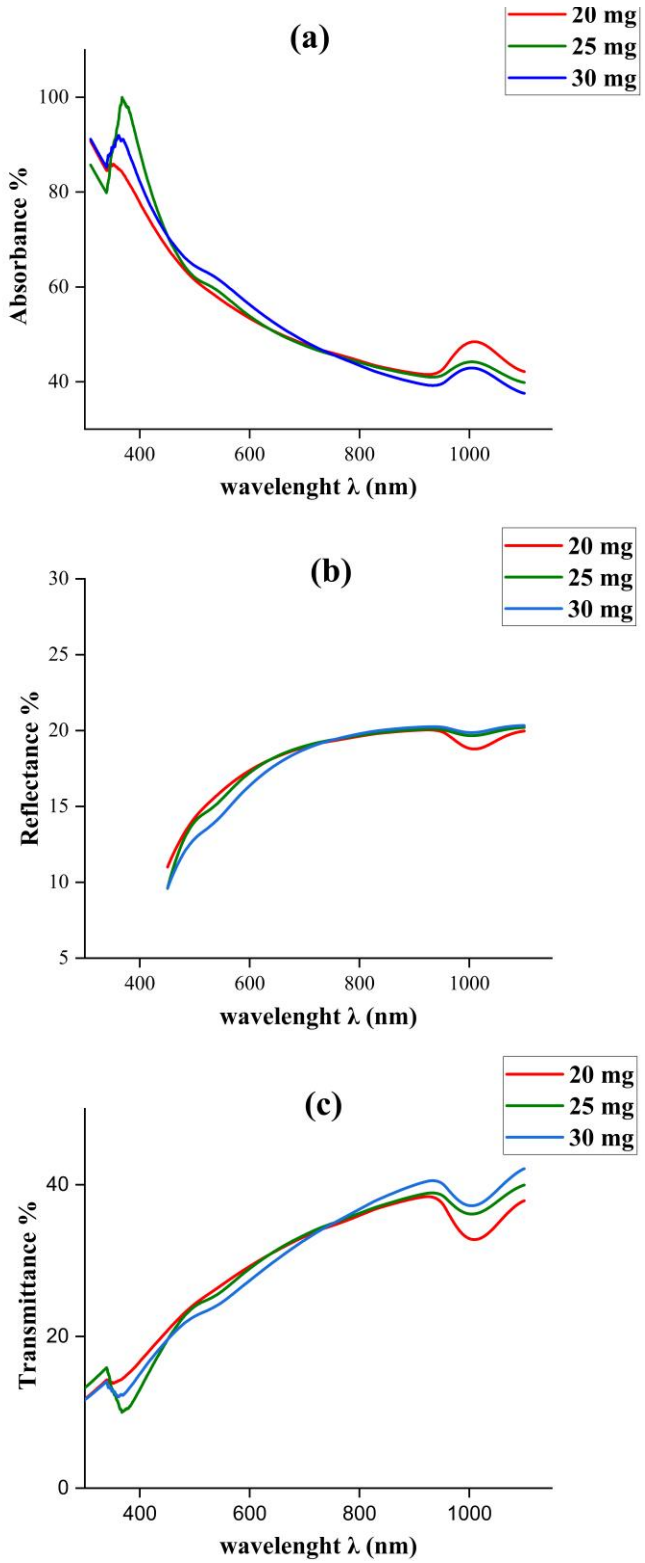

Figure 3.34: (a) Absorption, (b) Reflection, and (c) Transmission spectra of the SiO_2/Au Samples where the SiO_2 mass is 20, 25, and 30 mg and the current applied is 125 A.

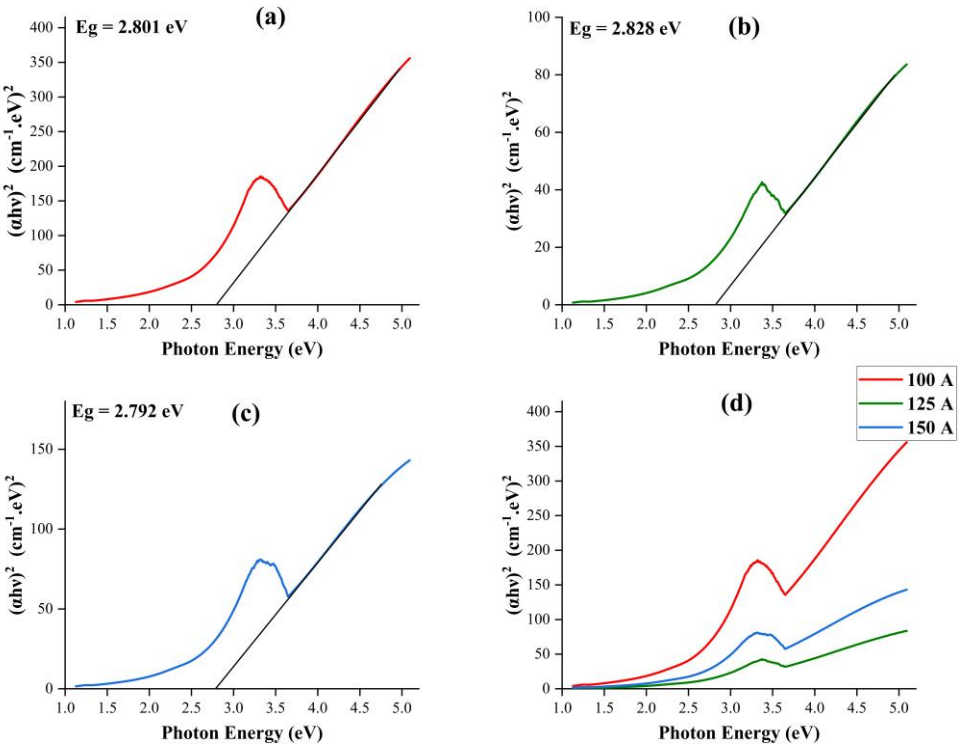

Figure 3.35: Tauc Plots for each SiO_2/Au sample where the applied current is (a) 100, (b) 125, (c) 150 A and (d) 100, 125 and 150 A and the SiO_2 mass is 25 mg.

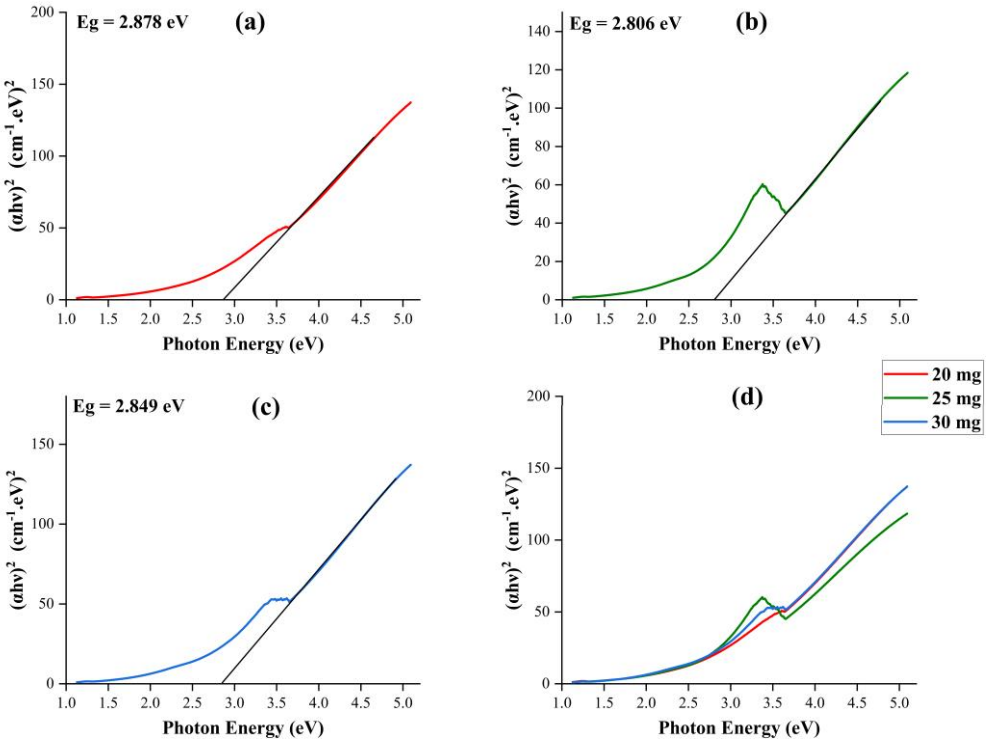

Figure 3.36: Tauc plots for each SiO_2/Au sample where the SiO_2 mass is (a) 20, (b) 25, (c) 30 mg and (d) 20,25, and 30 mg where the applied current is 125 A.

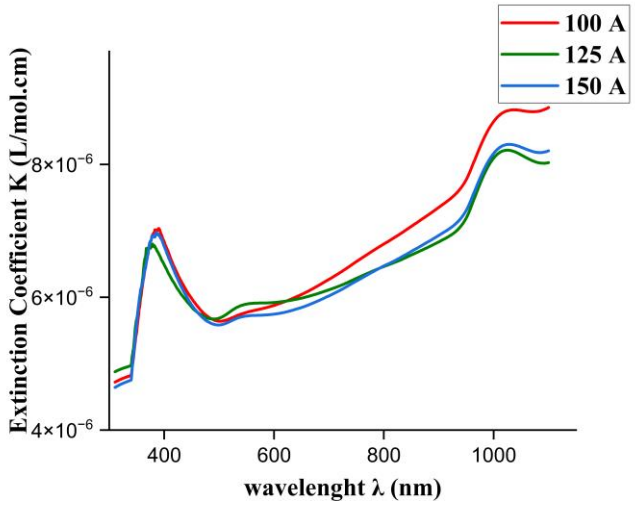

Figure 3.37: Extinction coefficient of the SiO_2/Au samples where the applied current is 100, 125 and 150 A and the SiO_2 mass is 25 mg.

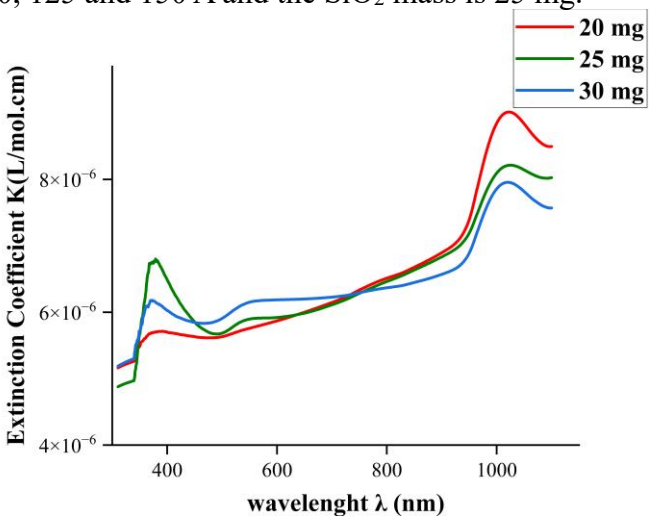

Figure 3.38: Extinction coefficient of the SiO_2/Au samples where the SiO_2 mass is 20, 25, and 30 mg and the current applied is 125 A.

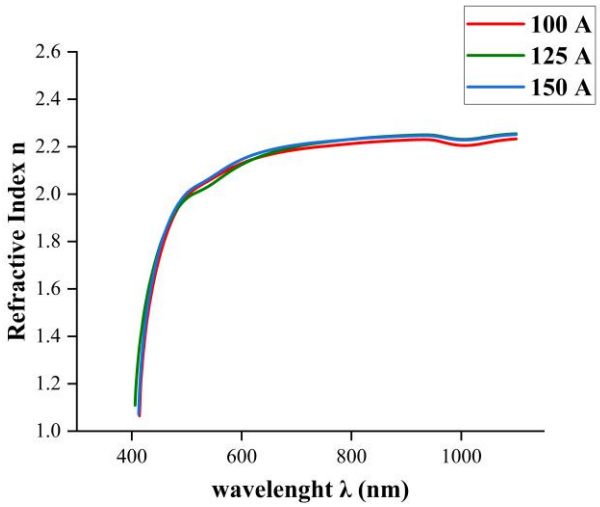

Figure 3.39: Refractive index of the SiO_2/Au samples where the applied current is 100, 125 and 150 A and the SiO_2 mass is 25 mg.

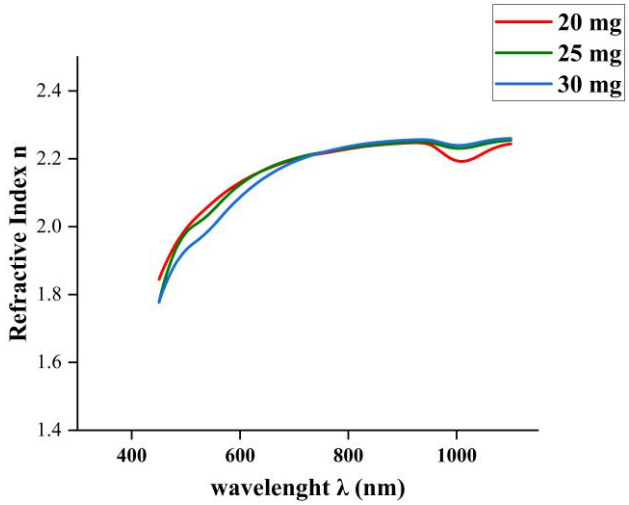

Figure 3.40: Refractive index of the SiO_2/Au samples where the SiO_2 mass is 20, 25, and 30 mg and the current applied is 125 A.

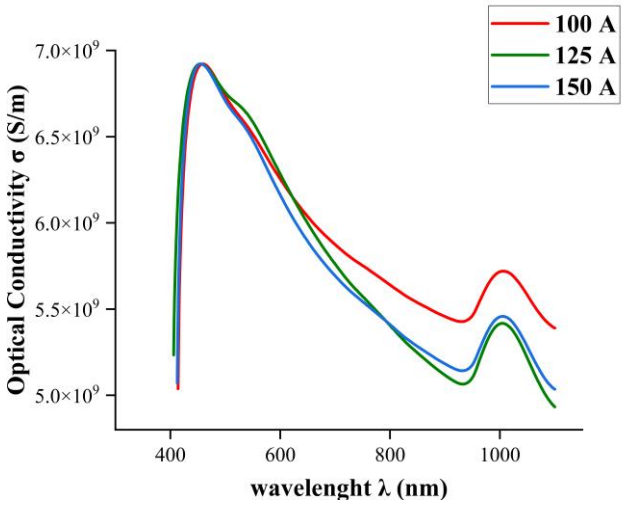

Figure 3.41: The optical conductivity of the SiO_2/Au samples where the applied current is 100, 125 and 150 A and the SiO_2 mass is 25 mg.

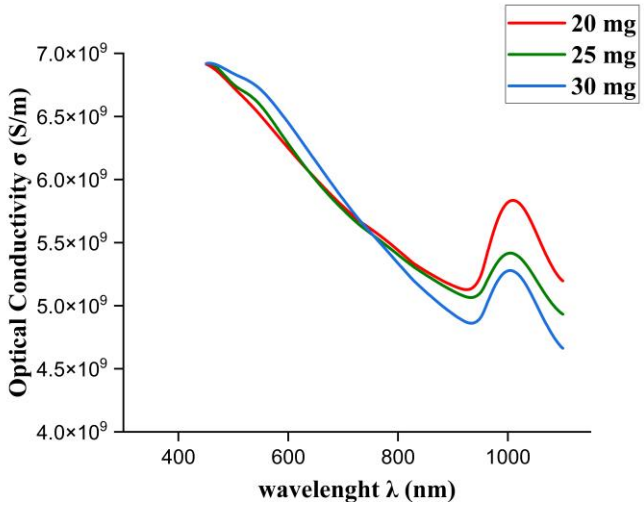

Figure 3.42: The optical conductivity of the SiO_2/Au samples where the SiO_2 mass is 20, 25, and 30 mg and the current applied is 125 A.

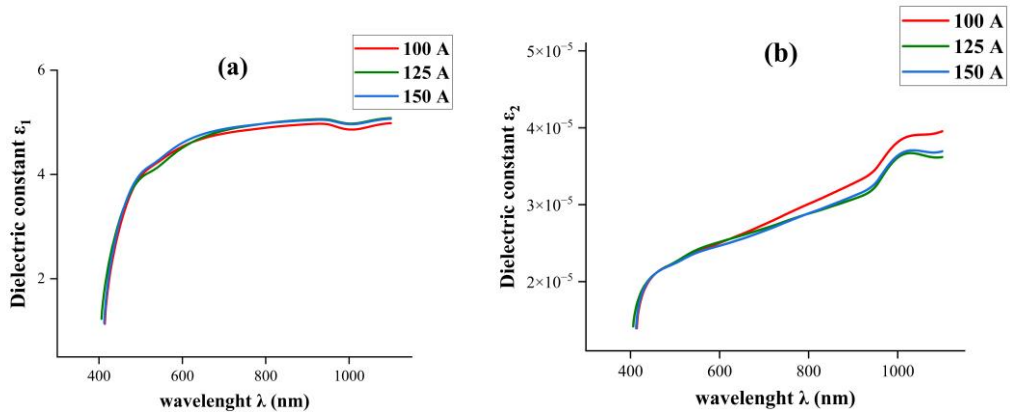

Figure 3.43: (a) The real part and (b) The imaginary part of the dielectric constants of the SiO_2/Au nanostructures where the applied current is 100, 125 and 150 A and the SiO_2 mass is 25 mg.

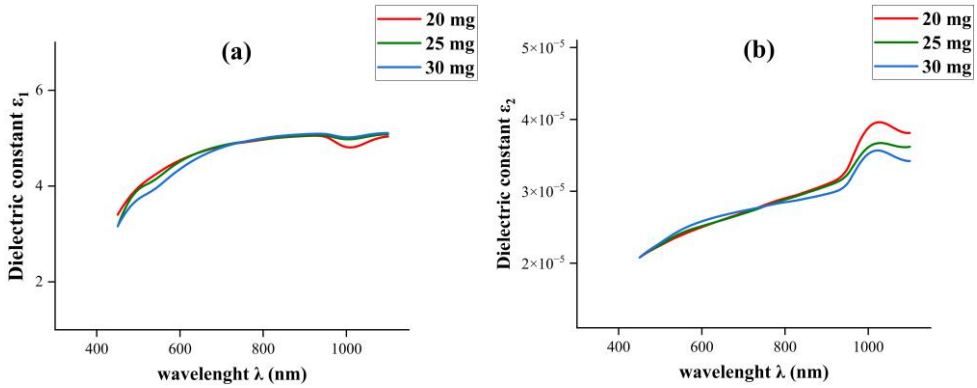

Figure 3.44: (a) The real part and (b) The imaginary part of the dielectric constants of the SiO_2/Au nanostructures where the SiO_2 mass is 20, 25, and 30 mg and the current applied is 125 A.

Table 3.7: The optical parameters' average values with the SiO_2 mass is 20, 25, and 30 mg and the current applied is 125 A.

Current (A)	A %	T %	R %	α	E.G. (eV)	K (L/mol.cm)10^{-6}	n	σ (S/m) (10^9)	ε_1	ε_2 (10^{-5})
100	48.868	32.451	18.681	1.125	2.801	6.267	2.187	5.874	4.786	2.743
125	47.650	33.377	18.976	1.097	2.828	6.113	2.201	5.761	4.843	2.69
150	46.935	33.929	19.137	1.081	2.792	6.021	2.208	5.692	4.874	2.659

Table 3.8: The optical parameters' average values with the applied current is 100, 125 and 150 A and the SiO_2 mass is 25 mg.

SiO_2 mass (mg)	A %	T %	R %	α	E.G. (eV)	K (L/mol.cm)10^{-6}	n	σ (S/m)(10^9)	ε_1	ε_2 (10^{-5})
20	47.916	33.171	18.913	1.104	2.878	6.147	2.198	5.786	4.831	2.702
25	47.650	33.376	18.976	1.104	2.806	6.113	2.201	5.761	4.843	2.690
30	48.545	32.694	18.761	1.081	2.849	6.228	2.191	5.845	4.802	2.729

3.7 Conclusion

The electrical exploding wire (UEEW) technique has been automated and used to produce plasma and SiO_2/Au nanostructures within an SiO_2 suspension. The plasma has been diagnosed using the optical emission spectroscopy (OES) and the nanostructures have been characterized via X-ray diffraction (XRD), field-emission scanning electron microscopy (FE-SEM), energy-dispersive X-ray spectroscopy (EDS), transmission electron microscopy (TEM), and UV-Visible spectroscopy. to analyze the nanostructures. This study produced the following essential results:

1. Plasma Characteristics and OES Analysis: The plasma emission spectra in the colloidal suspension presented intense ionic and atomic spectral lines (Hα, O I, O II, Au I Si I, Si II). The observed spectral lines intensity were directly proportional to the applied current and the added SiO_2 mass. While the electron temperature T_e and electron density n_e measurements has

displayed a linear relationship between Te and ne measurements which increased with current strength until Te reached its peak at 25 mg SiO_2.

2. Structural Properties: The SiO_2/Au thin films demonstrated the face-centered cubic (FCC) structure (space group *Fm-3m*). The intensity of Au (111) peak increased with increasing current values which led to better Au deposition on SiO_2. The presence of the Au (220) peak demonstrates potential applications based on higher plasmonic effect (e.g., surface-enhanced Raman spectroscopy or SERS).

3. Morphological Properties: FE-SEM images of the thin films and TEM images of the colloidal suspension showed spherical core-shell nanostructures with observed aggregation and sizes varying from 21–39 nm which increased with current and decreased with SiO_2 mass. EDS results of the thin films showed Au, Si, and O present in the samples with the greatest Au weight percentage found at 125 A and 25 mg SiO_2.

4. Optical Properties: UV-Vis spectroscopy for the thin films showed the UV region interband transition bands between 348–378 nm. LSPR peaks appeared in the visible (550–553 nm) and NIR (1004–1007 nm) regions with increased broadening because of nanoparticle aggregation. The material exhibited direct bandgap (Eg) characteristics that made it suitable for optoelectronic devices according to Tauc plot evaluations.

Optical constants (refractive index n, extinction coefficient k, dielectric constants ε_1 and ε_2) exhibited trends favorable for: Antireflection coatings (low *n*). UV photodetectors (high optical conductivity in UV). Telecommunications (high dielectric constants in NIR for optical switching).

3.8 Recommendations and Future Work

1. Mechanistic Studies on Plasma-Nanoparticle Interactions: Time-resolved OES analysis should be performed to link plasma dynamics (Te, ne) with nucleation and growth stages of nanoparticles. A computational model using molecular dynamics or finite element analysis needs to be developed to model the UEEW process.

2. Scalability and Industrial Viability: A continuous-flow UEEW system should be designed for manufacturing SiO_2/Au nanostructures at an industrial scale. The method needs evaluation for its cost-effectiveness relative to standard chemical synthesis techniques.

3. Hybrid Nanostructures: The combination of plasmonic catalytic and photocatalytic functions should be achieved by synthesizing ternary systems such as SiO_2/Au/TiO_2. Examine how hybrid nanostructures function together in energy storage systems including supercapacitors.

4. Long-Term Stability and Environmental Impact: The research needs to evaluate the operational stability of SiO_2/Au nanostructures through thermal

and chemical exposure tests. The research needs to evaluate the toxicity and biodegradability of the nanoparticles to determine environmental safety.

5. Functionalization for Targeted Applications: SiO_2/Au nanostructures should be tested for their catalytic properties in CO_2 reduction reactions and dye degradation applications. The surface of the material should be functionalized with biomolecules like antibodies to support biomedical applications including biosensing and drug delivery.

References

[1] J.W. Bradley, P.M. Bryant, Plasma Technologies for Textiles, Woodhead Publishing, 2007.

[2] Chiow San Wong , Rattachat Mongkolnavin, Elements of Plasma Technology, Springer Singapore, 2016.

[3] Richard Engeln, Bart Klarenaar, Olivier Guaitella, "Foundations of optical diagnostics in low-temperature plasmas," *Plasma Sources Science and Technology,* vol. 29, no. 6, 2020.

[4] Xiao Chen & Luting Yan, "Application of Au, SiO2@Au, and Au@SiO2 nanoparticles in PTB7:PC71BM polymer solar cells," *Journal of Materials Science: Materials in Electronics ,* vol. 29, p. 13698–13704, 2017.

[5] Liddell, Henry George; Scott, Robert , "πλάσμα". A Greek-English Lexicon, Clarendon Press, 1940.

[6] F. F. Chen, Introduction to Plasma Physics and Controlled Fusion, Springer Cham, 2016.

[7] Donald A. Gurnett and Amitava Bhattacharjee, Introduction to plasma physics, Cambridge University Press, 2017.

[8] Riccardo d'Agostino, Pietro Favia, Yoshinobu Kawai, Hideo Ikegami, Noriyoshi Sato, Farzaneh Arefi-Khonsari, Advanced Plasma Technology, Wiley-VCH Verlag GmbH & Co. KGaA, 2007.

[9] J. Votano, M. Parham, and L. Hall, Advanced plasma thechnology, Weinheim: Verlag GmbH & Co. kGaA, 2004.

[10] F. C., Optical Diagnostics of Colliding Laser Produced Plasmas Towards Next Generation Plasma Light Sources, Dublin : Dublin City University, 2013.

[11] S. Eliezer and Y. Eliezer, The Fourth State of Matter: An Introduction to Plasma Science, Boca Raton: CRC Press, 2001.

[12] W. Thompson, "The dynamics of high temperature plasmas," *Reports on Progress in Physics,* vol. 24, pp. 363-424, 1961.

[13] Han, H., Park, S., Sung, C., Kang, J., Lee, Y., Chung, J., Hahm, T., Kim, B., Park, J., Bak, J., Cha, M., Choi, G., Choi, M., Gwak, J., Hahn, S., Jang, J., Lee, K., Kim, J., Kim, S., Kim, W., Ko, J., Ko, W., Lee, C., Lee, J., Lee, J., Lee, J., Lee, K., Pa, "A sustained high-temperature fusion plasma regime facilitated by fast ions.," *Nature,* vol. 609, pp. 269 - 275, 2022.

[14] Murphy, A., & Uhrlandt, D., "Foundations of High-Pressure Thermal Plasmas," *Plasma Sources Science and Technology,* vol. 27, 2018.

[15] Guo, H., Zhang, X., Chen, J., Li, H., & Ostrikov, K. , "Non-equilibrium synergistic effects in atmospheric pressure plasmas.," *Scientific Reports,* vol. 8, 2018.

[16] Gleizes, A., Gonzalez, J., & Freton, P. , "Thermal plasma modelling," *Journal of Physics D: Applied Physics,* vol. 38, pp. R153 - R183., 2005.

[17] P. Lu, P.J. Cullen,K. Ostrikov, Cold Plasma in Food and Agriculture, Academic Press, 2016.

[18] Dobslaw, C., & Glocker, B. , "Plasma Technology and Its Relevance in Waste Air and Waste Gas Treatment.," *Sustainability,* vol. 12, p. 8981, 2020.

[19] Veerana, M., Yu, N., Ketya, W., & Park, G. , "Application of Non-Thermal Plasma to Fungal Resources.," *Journal of Fungi,* vol. 8, 2022.

[20] Moszczyńska, J., Roszek, K., & Wiśniewski, M. , "Non-Thermal Plasma Application in Medicine—Focus on Reactive Species Involvement.," *International Journal of Molecular Sciences,,* vol. 24, 2023.

[21] Kim, S., Chung, T., Joh, H., Cha, J., Eom, I., & Lee, H., "Characteristics of Multiple Plasma Plumes and Formation of Bullets in an Atmospheric- Pressure Plasma Jet Array," *IEEE Transactions on Plasma Science,* vol. 43, pp. 753-759, 2015.

[22] Sahar Hosseinzadeh Kassani, Reza Khazaeinezhad, Chan Young Lee and Tavakol Nazari, "Visible emission enhancement in fiber

optic atmospheric pressure helium plasma jet," *Lasers and Electro-Optics Pacific Rim (CLEO-PR),* pp. 1-2, 2013.

[23] Lee, S., , S., Hong, Y., & Choi, M., "Effects of pulsed and continuous wave discharges of underwater plasma on Escherichia coli.," *Separation and Purification Technology,* vol. 193, pp. 351-357, 2018.

[24] Pilch, I., Söderström, D., Brenning, N., & Helmersson, U, "Size-controlled growth of nanoparticles in a highly ionized pulsed plasma," *Applied Physics Letters,* vol. 102, p. 033108, 2013.

[25] Shaojie Zhang, Wansheng Chen, Yong Lu, Yongmin Zhang, Shuangming Wang, Aici Qiu, Liang Ma, Liang Gao, and Fei Chen, "Underwater electrical wire explosions under different discharge types: An experimental study with high initial energy storage," *Physics of Plasmas,* vol. 3, no. 4, 2024.

[26] Krasik, Y., Fedotov, A., Sheftman, D., Efimov, S., Sayapin, A., Gurovich, V., Veksler, D., Bazalitski, G., Gleizer, S., Grinenko, A., & Oreshkin, V., "Underwater electrical wire explosion," *Plasma Sources Science and Technology,* vol. 19, p. 034020, 2010.

[27] S. F. Golovashchenko , A. J. Gillard , and A. V. Mamutov , "Formability of dual phase steels in electrohydraulic forming," *J. Mater. Process. Technol.,* vol. 213, no. 7, pp. 1191-1212, 2013.

[28] J. Wu , Y. Lu , F. Sun , X. Jiang , Z. Wang , D. Zhang , X. Li , and A. Qiu, " Researches on preconditioned wire array Z pinches in Xi'an Jiaotong University," *Matter Radiat. Extremes,* vol. 4, 2019.

[29] Ruoyu Han, Jiawei Wu, Haibin Zhou, Yongmin Zhang, Aici Qiu, Jiaqi Yan, Weidong Ding, Chen Li, Chenyang Zhang, Jiting Ouyang, "Experiments on the characteristics of underwater electrical wire explosions for reservoir stimulation," *Matter Radiat. Extremes,* vol. 5, no. 4, 2020.

[30] Y. A. Kotov, "Electric explosion of wires as a method for preparation of nanopowders," *J. Nanopart. Res.,* vol. 5, pp. 539-550, 2003.

[31] Virozub, A., Gurovich, V., Yanuka, D., Antonov, O., & Krasik, Y., "Addressing optimal underwater electrical explosion of a wire," *Physics of Plasmas,* vol. 23, p. 092708, 2016.

[32] D. Nicholson and D. R. Nicholson., Introduction to Plasma Theory, New York, 1983.

[33] A Roosmalen, , J. Baggerman, and S. Brader., Dry Etching for Vlsi, Springer Science & Business Media, 2013.

[34] P.Gibbon, Introduction to Plasma Physics, arXiv preprint , 2020.

[35] I. P. Herman, Optical Diagnostics for Thin Film Processing, Academic Press, 1996.

[36] Himanshu Mishra, Mishra, H., Tichý, M.,and Kudrna, P., "Optical emission spectroscopy study of plasma parameters in low-pressure hollow cathode plasma jet and planar magnetron powered by DC and pulsed DC supply," *Vacuum,* vol. 205, p. 111413, 2022.

[37] H. Akatsuka, "Optical Emission Spectroscopic (OES) analysis for diagnostics of electron density and temperature in non-equilibrium argon plasma based on collisional-radiative model," *Advances in Physics:X,* vol. 4, 2019.

[38] T. Belmonte, C. Noël, T. Gries, Julien Martin, G. Henrion, "Theoretical background of optical emission spectroscopy for analysis of atmospheric pressure plasmas," *Plasma Sources Science and Technology,* vol. 24, 2015.

[39] S. S. Harilal, B. Brumfield, N. LaHaye, K. Hartig, M. Phillips, "Optical spectroscopy of laser-produced plasmas for standoff isotopic analysis," *Applied Physics Reviews,* 2018.

[40] Hira Fatima,Ullah, M.U., Ahmad, S, Mubashair Imran, S. Sajjad, S.Hussain, and A. Qayyum, "Spectroscopic evaluation of vibrational temperature and electron density in reduced pressure radio frequency nitrogen plasma," *Discover Applied Sciences,* vol. 3, 2021.

[41] C. M. Samuell, A. G. Mclean, C. A. Johnson, F. Glass, A. E. Jaervinen;, "Measuring the electron temperature and identifying

plasma detachment using machine learning and spectroscopy," *Sci. Instrum.,* vol. 92, no. 4, 2021.

[42] E. C. Dutra, J. A. Koch, R. Presura, P. Wiewior, A. M. Covington, "Electron temperature and electron number density measurements in laser ablation Z-pinch experiments of Al2O3," *Phys. Plasmas ,* vol. 6, no. 8, 2019.

[43] D. M. Devia , L. V. Rodriguez-Restrepo, E. Restrepo-Parra, "Methods Employed in Optical Emission Spectroscopy Analysis: a Review," *Ingeniería y Ciencia,* vol. 11, no. 21, p. 239–267, 2015.

[44] T. Boyd and J.J. Sanderson, The Physics of Plasmas, New York: Cambridge University Press, 2003.

[45] Liu, F., Nie, Z., Xu, X., Zhou, Q., Li, L., & Liang, R., "Measurement of electron density by Stark broadening in an ablative pulsed plasma thruster," *Applied Physics Letters,* vol. 93, p. 111502, 2008.

[46] Sabu Thomas, Seiko Jose, Wool Fiber Reinforced Polymer Composites, The Textile Institute Book Series, 2022.

[47] Karthikeyan Subramani,Waqar Ahmed, Nanobiomaterials in Clinical Dentistry, Elsevier, 2019.

[48] Anupam Das Talukdar, Satyajit Dey Sarker and Jayanta Kumar Patra, Advances in Nanotechnology-Based Drug Delivery Systems, Elsevier, 2022.

[49] Jitendra Kumar Katiyar, Vinay Panwar, Neha Ahlawat, Nanomaterials For Advanced Technologies, Springer Singapore, 2022.

[50] Murtala Namakka, Md. Rezaur Rahman,Khairul Anwar Mohamad Bin Said,Mohammad Abdul Mannan,Abdul Majed Patwary, "A review of nanoparticle synthesis methods, classifications, applications, and characterization," *Environmental Nanotechnology, Monitoring & Management,* vol. 20, 2023.

[51] Cheng, H.; Ma, J.; Zhao, Z.; Qi, L., "Hydrothermal Preparation of Uniform Nanosize Rutile and Anatase Particles," *Chem. Mater.,* vol. 7, p. 663–671, 1995.

[52] Paulina Szczyglewska, Agnieszka Feliczak-Guzik, I. Nowak, "Paulina Szczyglewska, Agnieszka Feliczak-Guzik, I. Nowak," *Molecules,* vol. 28, 2023.

[53] V. Harish, M. M. Ansari, Devesh Tewari, A. B. Yadav, N. Sharma, Sweta Bawarig, M. García-Betancourt, A. Karatutlu, M. Bechelany, Ahmed Barhoum, "Cutting-edge advances in tailoring size, shape, and functionality of nanoparticles and nanostructures: A review," *Journal of the Taiwan Institute of Chemical Engineers,* 2023.

[54] He, S.; Zhang, Y.; Guo, Z.; Gu, N., "Biological Synthesis of Gold Nanowires Using Extract of Rhodopseudomonas capsulata," *Biotechnol. Prog.,* vol. 24, p. 476–480., 2008.

[55] Damonte, L.; Zélis, L.M.; Soucase, B.M.; Fenollosa, M.H., "Nanoparticles of ZnO obtained by mechanical milling," *Powder Technol.,* vol. 148, p. 15–19, 2004.

[56] Pimpin, A.; Srituravanich, W., "Review on Micro- and Nanolithography Techniques and their Applications.," *Eng. J.,* vol. 16, p. 37–56, 2012.

[57] Amendola, V.; Meneghetti, M. , "Laser ablation synthesis in solution and size manipulation of noble metal nanoparticles.," *Chem. Phys.,* vol. 11, p. 3805–3821, 2009.

[58] I. Bica, "Nanoparticle production by plasma," *Materials Science and Engineering,* vol. 68, pp. 5-9, 1999.

[59] Hao Yin, Xin Gao, Peng-wan Chen, "One-step synthesis of FeO(OH) nanoparticles by electric explosion of iron wire underwater," *Defence Technology,* vol. 18, no. 1, pp. 133-139, 2022.

[60] F. Hajipour, S. Asad, M.A. Amoozegar, A.A. Javidparvar, J. Tang, H. Zhong, K. Khajeh, "Developing a fluorescent hybrid Nanobiosensor Based on Quantum Dots and Azoreductase Enzyme Formethyl Red Monitoring," *Iran Biomed ,* vol. 25, 2021.

[61] Ahmed Barhoum and Abdel Salam Hamdy Makhlouf, Emerging Applications of Nanoparticles and Architecture Nanostructures, Elsevier, 2018.

[62] Ahmed Barhoum and Abdel Salam Hamdy Makhlouf, Emerging Applications of Nanoparticles and Architecture Nanostructures, Elsevier, 2018.

[63] Francis Verpoort, Ikram Ahmad, Awais Ahmad, Ching Yern Chee, Anish Khan, Nanomedicine Manufacturing and Applications, Elsevier, 2021.

[64] Ch Sateesh Kumar, M. Muralidhar Singh, Ram Krishna, Advanced Materials Characterization, Boca Raton: CRC Press, 2023.

[65] Sneha Mohan Bhagyaraj, Oluwatobi Samuel Oluwafemi, Nandakumar Kalarikkal, Sabu Thomas, Characterization of Nanomaterials, Woodhead Publishing, 2018.

[66] Alcorn, F., Jain, P., & Van Der Veen, R., "Time-resolved transmission electron microscopy for nanoscale chemical dynamics.," *Nature Reviews Chemistry,* vol. 7, pp. 256-272, 2023.

[67] Picollo, M., Aceto, M., & Vitorino, T., "UV-Vis spectroscopy," *Physical Sciences Reviews,* vol. 4, 2018.

[68] S. S. Hamed, "Spectroscopic Determination of Excitation Premixed Laminar Flame," *Egypt J. Solids,* vol. 28, 2005.

[69] M. H. Brodisky, Amorphous Semiconductors, Berlin Heidelberg: Springer-Verlage, 1979.

[70] Sahai, A., Goswami, N., Kaushik, S., & Tripathi, S., "Cu/Cu 2 O/CuO nanoparticles: Novel synthesis by exploding wire technique and extensive characterization," *Applied Surface Science,* vol. 390, pp. 974-983, 2016.

[71] Hoffman, J., Chrzanowska, J., Mościcki, T., Radziejewska, J., Stobiński, L., & Szymański, Z, "Plasma generated during underwater pulsed laser processing," *Applied Surface Science,* vol. 417, pp. 130-135, 2017.

[72] Sapkota, K., Chaudhary, P., & Han, S., "Environmentally sustainable route to SiO2@Au–Ag nanocomposites for biomedical and catalytic applications.," *RSC Advances,* vol. 8, pp. 31311 - 31321, 2018.

[73] Gamaleev, V., Furuta, H., & Hatta, A, "Generation of micro-arc discharge plasma in highly pressurized seawater," *Applied Physics Letters,* 2018.

[74] Bhattacharya, S., Tiwari, N., Mishra, A., Mitra, S., Dey, G., & Ghorui, S. , "Underwater Electrical Discharges: Temperature, Density and Basic Instability Features with Different Anode Materials," *Plasma Chemistry and Plasma Processing,* vol. 39, pp. 1019-1048, 2019.

[75] Bacqueyrisses, Y., Reess, T., De Ferron, A., Tchalla, V., & Novac, B., "Phenomenological Studies for Optimizing Subsonic Underwater Discharges.," *IEEE Transactions on Plasma Science,* vol. 49, pp. 3615-3624, 2021.

[76] Kumar, L., Chakravarthy, S., Verma, R., Jayaganthan, R., Sarathi, R., & Srinivasan, A., "Synthesis of multiphase binary eutectic Al–Mg alloy-nanoparticles by electrical wire explosion technique for high-energy applications, its characterization and size-dependent thermodynamic and kinetic study," *Journal of Alloys and Compounds,* vol. 838, p. 155630, 2020.

[77] Yan, D., Lai, L., Xiao, X., Zhang, L., & Chen, I., "Study on Breakdown Process of High -Voltage Pulse Discharge under Water based on Equivalence Theory and Numerical Simulation," *Journal of Engineering Science and Technology Review,* 2023.

[78] Li, X., Lan, M., Zheng, P., Zheng, W., Song, Y., Zhao, Z., & Li, J, "Repetitive shock waves generated by a single long pulse underwater arc discharge," *Physics of Fluids,* 2024.

[79] Simeni, M., Luo, Y., & Bruggeman, P., "On the origins of the continuum radiation of an underwater nanosecond pulsed discharge: An absolute-intensity optical emission spectroscopy study," *Plasma Sources Science and Technology,* 2025.

[80] Dnyaneshwar Kalyane, Narendra Kumar, Neelima Anup, Kuldeep Rajpoot, Rahul Maheshwari, Pinaki Sengupta, Kiran Kalia, Rakesh Kumar Tekade, "Recent advancements and future submissions of silica core-shell nanoparticles," *International Journal of Pharmaceutics,* vol. 609, 2021.

[81] Michitaka Yamamoto, Takashi Matsumae, Yuichi Kurashima, Hideki Takagi, Tadatomo Suga, Toshihiro Itoh, and EijiHigurashi, "Growth Behavior of Au Films on SiO2 Film and Direct Transfer for Smoothing Au Surfaces," *Int. J. of AutomationTechnology,* vol. 13 , no. 2, pp. 254-260, 2019.

[82] D. R. Lide, CRC Handbook of Chemistry and Physics, New York, 2004.

[83] D. Erenso, Virtual and Real Labs for Introductory Physics II, Virtual and Real Labs for Introductory Physics II, 2021.

[84] P. Hub, "The Beginners Guide to Micro Servos," Arduino cc, 2019.

[85] J. E. Sansonetti and W. C. Martin, "Handbook of Basic Atomic Spectroscopic Data," *Am. Inst. Phys,* vol. 34, no. 4, pp. 1739-2001, 2005.

[86] Varsha, M. Kria, J. E. Hamdaoui, L. Pérez, V. Prasad, M. El-Yadri, D. Laroze, E. Feddi, "Quantum Confined Stark Effect on the Linear and Nonlinear Optical Properties of SiGe/Si Semi Oblate and Prolate Quantum Dots Grown in Si Wetting Layer," *Nanomaterials,* vol. 11, 2021.

[87] M. Capitelli, G. Colonna, G. D. Ammando, and L. D. Pietanza, Laser-Induced Breakdown Spectroscopy, Berlin Heidelberg: Springer Series in Optical Scinces, 2014.

[88] M. Zhukov, Plasma Diagnostics, Mosco: Cambridge International Science Publishing, 2005.

[89] H. Park, S. J. You, and W. Choe, "Correlation between excitation temperature and electron temperature with two groups of electron energy distributions," *Phys. Plasmas,* vol. 17, no. 10, pp. 1-4, 2010.

[90] A. Lesage, "Experimental Stark Widths and Shifts for Spectral Lines of Neutral and Ionized Atoms," *J. Phys. Chem,* vol. 31, no. 3, pp. 819-972, 2002.

[91] Zekun Yin, Jian Wu, Liwen Liang, Chuncai Kong, A. Pervikov, Huantong Shi, Xingwen Li, "Microwave-absorbing performance of FeCoNi magnetic nanopowders synthesized by electrical explosion

of wires," *Journal of Alloys and Compounds,* vol. 966, no. 171594, 2023.

[92] Kramida, A., Ralchenko, Yu., Reader, J., and NIST ASD Team, "IST Atomic Spectra Database (ver. 5.12)," 2025.

[93] D. V. Douanla, Alim, C. G. L. Tiofack, A. Mohamadou, Dust–Acoustic Envelope Solitons and Rogue Waves in a Magnetized Electron-Depleted Plasma, vol. 47, Plasma Physics Reports, 2021, p. 384–395.

[94] W. Davey, "The Lattice Parameter And Density Of Pure," *Physical Review,* vol. 25, pp. 753-761, 1925.

[95] Taha M. Rashid, Uday M. Nayef. Majid S. Jabir and Falah A.-H. Mutlak, "Synthesis and characterization of Au:ZnO (core:shell)," *Optik,* 2021.

[96] Richa Goel, Sibashish Chakraborty, Vimarsh Awasthi, Vijayant Bhardwaj, Satish Kumar Dubey, "Exploring the various aspects of Surface enhanced Raman spectroscopy (SERS) with focus on the recent progress: SERS-active substrate, SERS-instrumentation, SERS-application," *Sensors and Actuators A: Physical,* vol. 376, 2024.

[97] Krishna Daware, Manasi Kasture, Ramchandra Kalubarme, Rakesh Shinde, Kashinath Patil, Norihiro Suzuki, Chiaki Terashima, Suresh Gosavi, Akira Fujishima, "Detection of toxic metal ions Pb2+ in water using SiO2@Au core-shell nanostructures: A simple technique for water quality monitoring," *Chemical Physics Letters,* vol. 732, 2019.

[98] Madalina Tudor, Raluca Borlan, Dana Maniu, Simion Astilean, Marc Lamy de la Chapelle, Monica Focsan, "Plasmon-enhanced photocatalysis: New horizons in carbon dioxide reduction technologies," *Science of The Total Environment,* vol. 923, 2024.

[99] Neeli Chandran, Manikanta Bayal, Rajendra Pilankatta & Swapna S. Nair , Nanomaterials for Luminescent Devices, Sensors, and Bio-imaging Applications, Singapore: Springer, 2021.

[100] Nawfal A. Alnidawi, Saba J. Kadhim, "Synthesis and characterizations of core-shell SiO2/Au/Ag nano-particles by

exploding of wire and pulsed laser plasmas," *AIP Conference Proceedings,* 2021.

[101] R. Soto, Kinetic Theory and Transport Phenomena, Oxford: Oxford Academic, 2016.

[102] B. Balamurugana and Toshiro Maruyama, "Evidence of an enhanced interband absorption in Au nanoparticles: Size-dependent electronic structure and optical properties," *APPLIED PHYSICS LETTERS,* vol. 87, 2005.

[103] K. Willets, R. V. Van Duyne, "Localized surface plasmon resonance spectroscopy and sensing.," *Annual review of physical chemistry,* pp. 267-297, 2007.

[104] Neeli Chandran, Manikanta Bayal, Rajendra Pilankatta & Swapna S. Nair , "Tuning of Surface Plasmon Resonance (SPR) in Metallic Nanoparticles for Their Applications in SERS," in *Nanomaterials for Luminescent Devices, Sensors, and Bio-imaging Applications*, Singapore, Springer, 2021, pp. 39-66.

[105] G M A Gad and Maroof A Hegazy, "Optoelectronic properties of gold nanoparticles synthesized by using wet," *Materials Research Express,* vol. 6, 2019.

[106] Shreyas Ramachandran, Simão M. João, Hanwen Jin, Johannes Lischner, "Hot carriers from intra- and interband transitions in gold-silver alloy nanoparticles," *Commun Chem,* vol. 169, no. 7, 2024.

[107] Ji, C., Liu, W., Bao, Y., Chen, X., Yang, G., Wei, B., Yang, F., & Wang, X., " Recent Applications of Antireflection Coatings in Solar Cells.," *Photonics,* vol. 9, 2022.

[108] Prateek Mishra, Vibhu Srivastava, Mirgendar Kumar & Sunny , "All-Dielectric Metasurface-Enabled Near-Infrared Switching Based on Ge2Sb2Te5 Phase-Change Material," *J. Electron. Mater. ,* vol. 49, p. 3913–3919, 2020.

[109] I. H. Hutchinson, Principles of Plasma Diagnostics, Cambridge: Cambridge University Press, 2002.

[110] Maher I. Boulos , Pierre L. Fauchais , Emil Pfender, Handbook of Thermal Plasmas, Springer Cham, 2020.

[111] D’Amato, R.; Falconieri, M.; Gagliardi, S.; Popovici, E.; Serra, E.; Terranova, G.; Borsella, E. , "Synthesis of ceramic nanoparticles by laser pyrolysis: From research to applications.," *J. Anal. Appl. Pyrolysis,* vol. 104, p. 461–469, 2013.

[112] H.Aspden, "The exploding wire phenomenon," *Physics Letters A,* vol. 107, no. 5, pp. 238-240, 1985.

[113] Toru Sasaki, Yuuri Yano, Mitsuo Nakajima, Tohru Kawamura, and Kazuhiko Horioka, "Warm-dense-matter studies using pulse-powered wire discharges in water," *Laser and Particle Beam,* vol. 24, no. 1-2, pp. 371-380, 2006.

[114] Dawood M. Khudhair, Duaa A. Uamran, Orass A. Hussein and Alyaa A. Ajbar, "Structure and Optical Properties of Olive Oil Thin Films Obtained by Plasma Jet Polymerization," *NLOQO,* vol. 58, pp. 167-176, 2023.

[115] Gamaleev, V., Furuta, H., & Hatta, A, "Generation of micro-arc discharge plasma in highly pressurized seawater," *Applied Physics Letters,* 2018.

[116] Li, C., Han, R., Li, J., Deng, C., Yang, B., & Ouyang, J., "Exploring the Influence of the Evolution of Discharge Plasma Channel on the Characteristics of Electric Explosion Products," *IEEE Transactions on Industry Applications,* vol. 59, pp. 456-464, 2023.

[117] Caposciutti, G., Tellini, B., Saccomandi, P., & Cigada, A, "Experimental analysis on the exploding wire process for nanopowder production: Influence of initial energy and exploding atmosphere," *Acta IMEKO,* 2023.

[118] Yin, Z., Wu, J., Liang, L., Kong, C., Pervikov, A., Shi, H., & Li, X, "Microwave-absorbing performance of FeCoNi magnetic nanopowders synthesized by electrical explosion of wires," *Journal of Alloys and Compounds,* 2023.

[119] Wang, S., Cui, B., Cai, Q., Bu, Y., Wang, X., Cao, M., Xia, Y., & He, H., "Fabrication of highly luminescent SiO2–Au nanostructures and their application in detection of trace Hg2+," *Journal of Materials Science,* vol. 54, pp. 7517-7528, 2019.

[120] Yang, Y., Zhu, J., Zhao, J., Weng, G., Li, J., & Zhao, J., "Growth of Spherical Gold Satellites on the Surface of Au@Ag@SiO2 Core-Shell Nanostructures Used for an Ultrasensitive SERS Immunoassay of Alpha-Fetoprotein.," *ACS applied materials & interfaces,* vol. 11 3, pp. 3617-3626, 2019.

[121] Kaur, G., Kaur, V., Kaur, N., Kaur, C., Shanavas, A., Sen, T., & Sood, K., "Design of Silica@Au Hybrid Nanostars for Enhanced SERS and Photothermal Effect," *Chemphyschem,* 2023.

[122] Chen, M., He, Y., Wang, X., & Hu, Y., "Complementary enhanced solar thermal conversion performance of core-shell nanoparticles," *Applied Energy,* vol. 211, pp. 735-742, 2018.

[123] Wang, K., Wang, Y., Wang, C., Jia, X., Li, J., Xiao, R., & Wang, S., "Facile synthesis of high-performance SiO2@Au core–shell nanoparticles with high SERS activity," *RSC Advances,* vol. 8, pp. 30825 - 30831, 2018.

[124] Hembury, M., Chiappini, C., Bertazzo, S., Kalber, T., Drisko, G., Ogunlade, O., Walker-Samuel, S., Krishna, K., Jumeaux, C., Beard, P., Kumar, C., Porter, A., Lythgoe, M., Boissière, C., Sanchez, C., & Stevens, M., "Gold–silica quantum rattles for multimodal imaging and therapy," *Proceedings of the National Academy of Sciences,* vol. 112, pp. 1959 - 1964, 2015.

[125] S V Priya, G. Indhumathi, S. Vignesh, U Swamyvel Chandar and K. Dinesh, "PLaboratory Safety System using IOT," *PSYCHOLOGY AND EDUCATION,* vol. 9, no. 57, pp. 7078-7084, 2020.

الخلاصة

لقد طورت تقنية السلك الكهربائي الانفجاري تحت الماء (UEEW) وتم استخدامها لتحضير مركبات SiO_2/Au النانوية و بلازما الذهب في عالق SiO_2 الغروي. درست خواص البلازما اثناء التحضير . حقق البحث عن تأثير التيار (١٠٠، ١٢٥، و١٥٠ أمبير) وكتلة SiO_2 (٢٠، ٢٥، و٣٠ ملغ) على معلمات البلازما (درجة حرارة الإلكترون T_e وكثافته n_e) وكذلك تمت دراسة الخصائص التركيبية والشكلية والبصرية لتراكيب SiO_2/Au النانوية.

استخدمت الدراسة مطيافية الانبعاث الضوئي (OES) لتحديد T_e وn_e من خلال مخطط بولتزمان وظاهرة تعريض ستارك. وتمت ملاحظة ارتفاع درجة حرارة الإلكترونات (حتى ١٠,٣٢ إلكترون فولت) وكثافة الإلكترونات (حتى ٠,٤٥×١٠^{18} سم$^{-3}$) بزيادة التيار المطبق.

أظهر تحليل حيود الأشعة السينية (XRD) أن التراكيب النانوية تحتوي على بلورة FCC للذهب بأحجام بلورية تتراوح بين ١٢ إلى ٣٤ نانومتر.

وعرضت صور المجهر الإلكتروني الماسح (FE-SEM) والمجهر الإلكتروني النافذ (TEM) أشكالًا كروية ذات حجوم تتراوح بين ٢١ و٣٩ نانومتر، وأظهرت نتائج طيف (UV-Visible) قمم رنين بلازموني سطحي محلي (LSPR) بين ٥٥٠ و١٠٠٧ نانومتر وفجوة طاقة مباشرة تتراوح بين 2.878-2.792 الكترون فولت.

تقدم هذه الرسالة معلومات أساسية حول تصنيع المواد النانوية بالبلازما من خلال توضيح كيفية تأثير معلمات البلازما على خصائص التراكيب النانوية لتطبيقات البلازمونية والطاقة المتجددة.

جامعة كربلاء

كلية العلوم

قسم الفيزياء

تطوير وتوصيف منظومة بلازما تحت الماء لتحضير مركبات SiO_2/Au النانوية

رسالة مقدمة الى مجلس كلية العلوم / جامعة كربلاء وهي جزء من متطلبات نيل درجة الماجستير في علوم الفيزياء

كتبت بواسطة:

سجى حميد عبد الحمزة

بإشراف:

أ.م.د. دعاء عادل عمران

صفر ١٤٤٧هـ

تموز ٢٠٢٥ م